Alma Mater Studiorum - Università di Bologna

School of Science
Department of Physics and Astronomy
Master Degree Programme in Astrophysics and Cosmology

Polluted white dwarfs and planetary debris with the CUBES spectrograph

Graduation Thesis

Presented by
Alice Vendrame

Supervisor:
Prof. Dr.
Andrea Miglio
Co-Supervisor:
Prof. Dr.
Andreas Quirrenbach

Appello
Academic Year 2022/23

Additional page

Contents

Chapter 1

Introduction

Terrestrial exoplanets

Extra-solar planets are a recent discovery in astrophysics research, as we will see in Chapter 3. The first exoplanet was discovered by Wolszczan (1994), while the observation of a planet around another main sequence star was taken by Mayor & Queloz (1995). So far, more than 5'000 planets are confirmed among the candidates found, and 190 of them are terrestrial (rocky celestial bodies with iron-rich cores; in the Solar System, Mars, Venus, Mercury and Earth are part of this category). Planets are discovered around a variety of stars, with a wide range of possible masses (up to 10^3 Earth masses) and orbital radii (see NASA (2023)).
The exoplanets research in the last decade focused on planets' detection and their atmosphere's characterization through spectroscopy, while we know little about the core composition of worlds outside Earth. Are Earth's geological structure and composition similar to other planets, or is our world unique? Space missions to Mars and Venus (and in the future to Jupiter's rocky moons, Europa and Ganymede) revealed a complex geological history, especially on the Red Planet, with ancient volcanic activity and possible tectonic motion. The insurmountable barrier of exoplanets' distance from the Solar System does not allow us to conduct similar research. Global physiography, impact craters, geological evolutionary residuals (such as large basins, outflow channels and volcanic traces) and any surface features are not available for exoplanetary scientists.

Evolved planetary systems

The Solar System is now around 4 billion years old. The Sun is in the middle of its main life sequence, in which it is burning hydrogen into helium in its core. At around $\cdot 10^{10}$ years hydrogen is going to run out, and the star is going to enter the giant phase: this process will increase the star radius. The Sun's habitable zone will move from 2 AU to nearly 9 AU at the tip of the Red Giant Branch, and this event will lead to the engulfment of Mercury and Venus inside the star, and have catastrophic consequences on Earth and Mars. The planetary system evolution is strongly influenced by its central star, and research on planets-star co-evolution has now a dominant position in exoplanets studies.

The last stage of stellar evolution for stars of mass less than 10 $M_{\odot}$ is a white dwarf, an electron-degenerate core remnant. Nearly 97% of our galaxy stars will end up as white dwarfs which do not continue nuclear reactions after the helium burning phase (exceptions are made by O- Ne white dwarfs, which stop nuclear powering at neon burning phase). But what does it happen to a possible planetary system near an evolving star turning into a white dwarf? In most cases, when a star undergoes the asymptotic giant branch phase, stellar winds are expected to eventually completely disrupt the hosting planetary system. This may lead to formation of a new protoplanetary disk, and huge injection of materials previously encapsulated inside the planets into the ISM. White dwarfs are usually found inside wide nebulae during their formation phase: the external layers and atmosphere are ejected into the interstellar medium, creating an area of gas material and dust. The evolved star is then composed of carbon and oxygen.

Material from the nebulae can fall back on the white dwarf external layer, producing an intriguing effect: a polluted white dwarf, or a stellar remnant with absorption lines of heavy elements, as iron and silicate (see Jura & Young (2014)). The process could bring on the star not only material already ejected, but any debris within the accretion radius , including components from the planetary system before the stellar evolution. This effect is photospheric metal pollution from planetary debris, and it can be clearly visible in heavily polluted white dwarfs: Ca, Ni, Fe, Mg, Ti, Na lines at different abundances have been observed (see Fig. 1.1).
A work of comparison between the Earth and the Solar System planets' geological structure and composition was conducted: a selection of common elements usually present in the Earth's core and crust was used to find a possible match on polluted white dwarfs' surface. Possible rocky planets could have populated the stellar system before the star evolution engulfed them, and some planets can possibly survive the evolved stages of the hosting star itself. If captured within its tidal radius, their interiors' elements abundances are retrievable on the stellar surface.

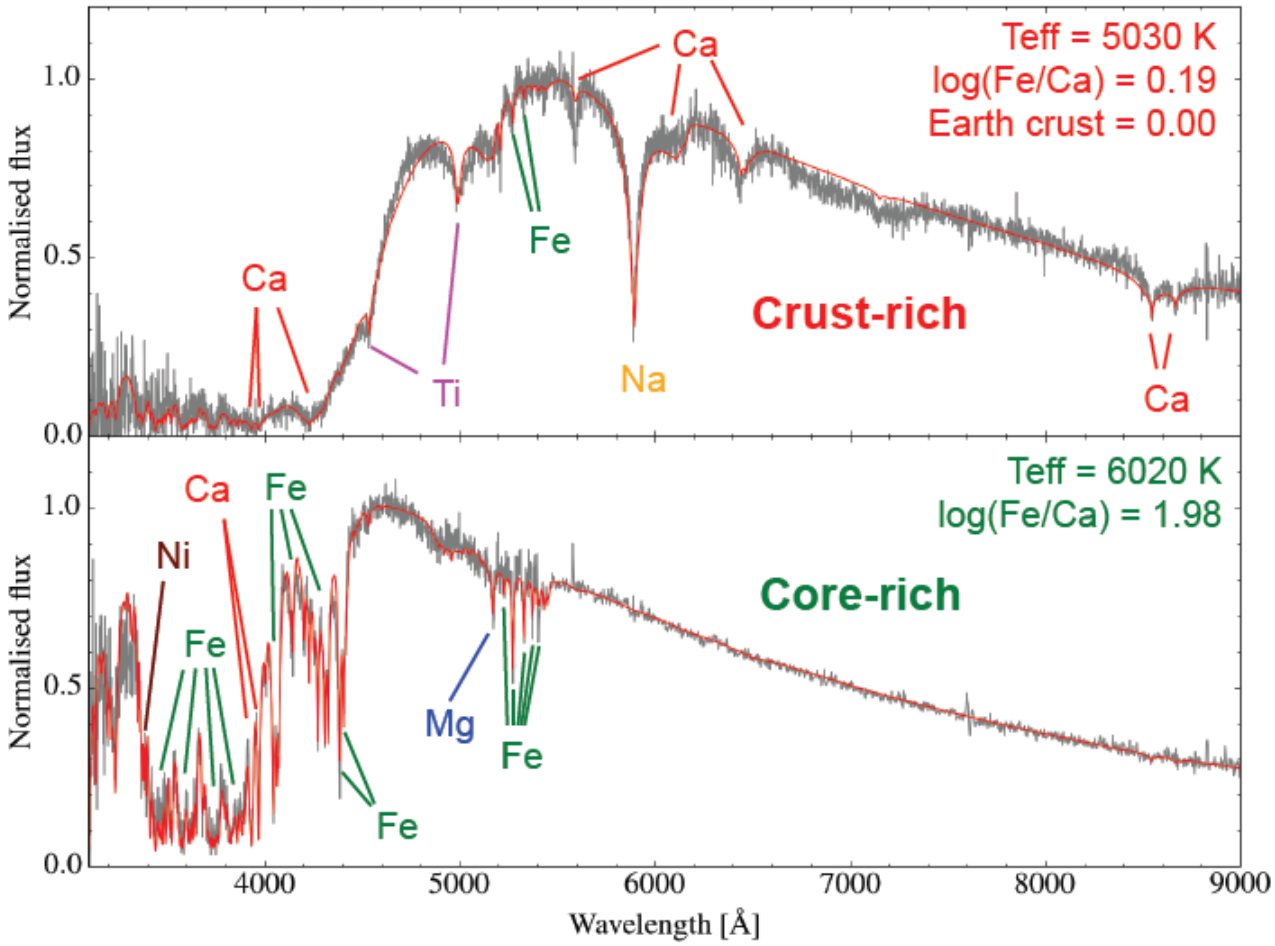

Figure 1.1: *One example of polluted white dwarf from Hollands et al. (2017), with elements comparable with Earth core and crust composition highlighted by Boris Gaensicke.*

CUBES spectrograph and the composition of exoplanets

The scope of this project is investigating the possibility for a new incoming instrument, CUBES (Very Large Telescope Array – INAF (2023)), to observe such absorption lines and the prospective of research. CUBES is a spectrograph with Cassegrain focus covering at high efficiency the UV ground-based region (300 - 400 nm) with intermediate resolution. Its scientific goals encompass both Galactic and extra-Galactic astronomy, in particular detecting iron and heavy elements (see Evans et al. (2023)). The instrument is in design phase, and a detailed simulator is available.

In this work, by simulating spectra at high resolution of polluted white dwarfs and analysing them in the range 300-400 nm, I tested the possibility of using CUBES in the context of future rocky planets research through white dwarfs exogeology. Detecting elements and calculating their abundances, it is possible as explained above to model the process of accretion on the star, and retrieve the planetesimals characteristics (Gänsicke et al. (2012)), such as the geological composition.

Chapter 2

White dwarfs: stellar remnants

The introduction on stellar physics and stellar evolution presented in what follows, is based on the book Carroll & Ostlie (2017); the review from Höfner & Olofsson (2018) was used to describe the mass loss phase.

2.1 Different stellar evolution and the path to evolved stars

A star's faith depends mostly on the star's initial mass. Low mass stars ($M < 0.5M_{\odot}$) are not able to reach the helium ignition temperature of 10^8 K. These stars are red dwarfs, with a temperature around 2,000 K and radius about 0.09 R_0; red dwarfs are so far the most common star type in the Milky Way, making upt to 65% of the total galaxy stars. Because red dwarfs fuse their hydrogen slowly and are fully convective (allowing their entire hydrogen supply to be fused, instead of merely that in the core), they are predicted to have longer lifespans with respect to the actual Universe's age.

Medium mass stars ($0.5 < M < 8M_{\odot}$), like the Sun, have a core sufficiently hot to fuse helium into carbon and oxygen. Near the end of the period in which it undergoes helium fusion in the core, a carbon–oxygen core will form in the star, surrounded by an inner helium-burning shell and an outer hydrogen-burning shell. The medium mass stars are the dominant type of objects that will undergo an extensive process of mass loss in the AGB (Asymptotic Giant Branch) stage, through thermal pulses. At the end of the Red Giant phase (second stage after the Main Sequence of the star), the helium burning process begins with a phenomenon called the He-shell flash: short and intense He-shell nuclear activity of 100-200 ys are interrupted by longer periods in which the outer layers are quiescent. The total duration is around 10^4 ys (it is longer for smaller stars) and it usually finishes when the the He burning process initiates the nucleosynthesis in the inter-shell region.

The AGB thermal pulses may lead to an energy outward flow and slow extinction of the burning phase in the outer shell. In the process, a dredge-up of material from

the inter-shell region to the surface is taking place, and nucleo-enriched elements appear in the star's envelope. The AGB stars tend to transition from M spectral type to C spectral type during the dredge-up, when the C/O ratio increases from 0.5 to >1. However, in very massive stars ($> 4M_{\odot}$) usually the CNO process destroys most of the carbon present in the envelope, avoiding the carbon star formation.

2.2 Mass loss phase and pulsating stars

During the thermal pulses period, there is an important mass loss process in the star's outside layers. The first wind ejection signs from a giant star were first observed by Deutsch (1956) in the binary system Alpha Herculis, where circumstellar absorption lines were seen in the spectrum of the companion star, suggesting that gas from the star was as far away as $10^5 R_{\odot}$ from the original star. It was calculated that the mass loss rate was around $3 \cdot 10^{-8} M_{\odot}$, and Reimers (1975) derived a relation between mass-loss rate and stellar characteristics (see equation 2.1). Dust and different particles were observed, especially in the IR, in various M and C-stars, confirming the presence of a large circumstellar disk (Neugebauer & Leighton (1969),Price & Walker (1976),Gehrz & Woolf (1971)). In addition, the observations showed a wide difference among dust compositions around M and C-type giants: in the Gilman (1969), this characteristics was explained to be caused by the high binding energy of the CO molecule, which prevents the less abundant of the two elements from forming other molecules and solids. Other molecular emissions from these stars were discovered, as OH masers (Wilson & Barrett (1968)) and CO rotational lines (Solomon et al. (1971)).

Stellar outflows

The rate of the mass loss depends on the initial star's mass. Mass loss is still a poorly constrained astrophysical process: so far, in stellar models it is usually parameterized with a free parameter. During evolved phases of the star's life, as AGB/RGB phases (Asymptotic Giant Branch and Red Giant Branch) the stellar radius increases, leading to a substantial decrease in surface gravity. Surface gravity is directly correlated with the star mass:

$$g = \frac{GM}{R^2}. \tag{2.1}$$

In this phenomenon, g can be reduced of more than 10 times the original value due to the radius increase. Even if during the red giant phase mass loss rate is important, at the end of the Asymptotic Giant Branch the process is crucial for white dwarf formation. At this stage of stellar life, the star reaches a mass-loss rate of $10^{-4} M_{\odot}/yr$, the highest peak of mass loss in a single star's life phase. It is also estimated that AGB stars are one of the major sources of dust in the Milky Way, as explained in Tielens et al. (2005). Mass loss rate from star surface is inversely proportional respect to radius in the evolutionary phase of giant star, as follow

$$\dot{M} \propto \frac{LR}{M}. \tag{2.2}$$

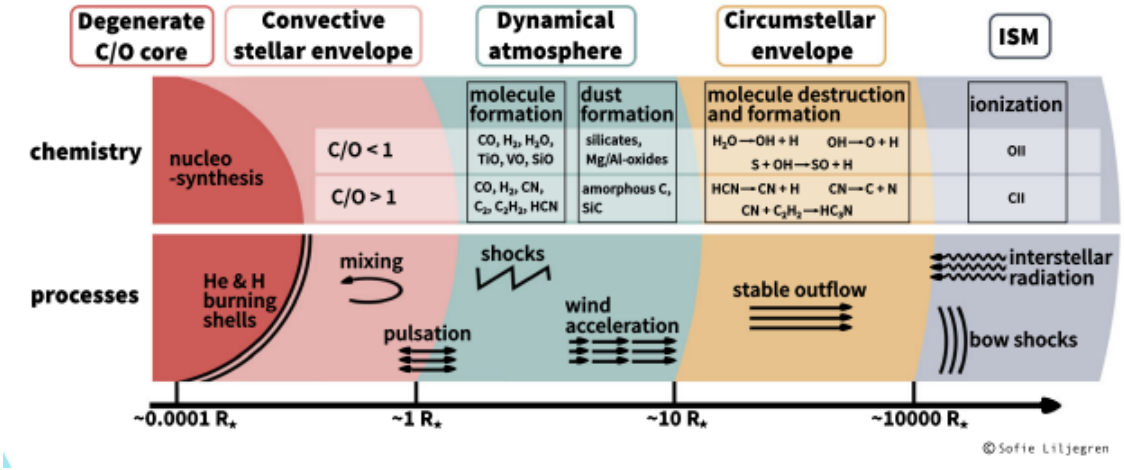

Figure 2.1: *A schematic figure of an AGB star and its circumstellar environment, including the various processes involved. By courtesy of S. Liljegren, from Höfner & Olofsson (2018).*

Increasing the radius allows a slow cooling of the external layers of the stellar surface, supporting the formation of molecules and dust grains, which are ejected through the winds. From meteorites, it was possible to discover that giant stars winds had a dominant role in the Solar System's original elements formation (Nittler & Ciesla (2016)).The origin of the winds is still under research and different theories of radiation-driven winds were proposed.

In general, the winds are produced thanks to the coupling of a variety of dynamical phenomena between the stellar interior (convection, pulsation), the atmosphere (strong radiating shocks) and the wind formation outer region (dust condensation, radiative acceleration). The major processes that contribute to winds formation are showed in Fig. 2.1. The most reliable theory so far is that the radiation pressure acts on microscopic solid-state particles in the dust present in the atmosphere of the stars, levitated during the pulsation, pushing them out of the stellar envelope (Höfner & Olofsson (2018)). Considering that for each photon the momentum is $p_\gamma = \frac{E_\gamma}{c}$, the total momentum emitted by the star per second is $p_{star} = \frac{L_{star}}{c}$. This value is comparable to the typical momentum of the gas/dust mixture leaving the star per second, which can be expressed proportionally respect to the mass-loss rate as $p_{star} = \dot{M} v_t$, where v_t is the wind terminal velocity. Assuming single-scattering limit (where each stellar photon transfers momentum through one interaction), it is possible to write:

$$\dot{M} v_t = \frac{L_{star}}{c}. \tag{2.3}$$

For a star with a luminosity around 5000 $L_\odot$, the wind velocity would be around 10 $km \cdot s^1$ and a wind's mass of $10^5 M_\odot$. In this calculation we are not considering the gravitational potential of the star.

In the atmospheres of cool giant stars most of the gas is composed of both

dust and molecules, which contribute to the mean opacity. In general, for wind with speed around 1000-3000 $km \cdot s^{-1}$, the atomic lines emission drives the outflow, with Doppler shifts in the acceleration zone increasing the effective line width (see Van Marle et al. (2010), Smith (2014)). For lower speed, around 100 kms^{-1}, molecular rotational-vibrational lines are dominant. However, the molecular emission tend to overlap with the IR stellar flux, and the ratio in equation 6.15 does not reach the necessary threshold to conduct the winds emission process. On the other side, the dust grains are very efficient at absorbing and scattering the stellar photons. In particular, amorphous carbon or magnesium-iron silicates are considered good candidates (they are often present around AGB stars). One problem is that, in standard conditions, the gas density drops exponentially with the distance from the star, and no gas would be found at typical dust condensation distances. An alternative explanation made of the combination of pulsation-induced shock waves and radiation pressure on dust is considered the most promising mechanism so far (e.g. Whitelock et al. (1991), McDonald & Zijlstra (2016),Tej et al. (2003), Ohnaka et al. (2017), Karovicova et al. (2013)). Curé & Araya (2023) proposed an innovative solution: the outflows are due to the momentum of photospheric photons transferred to the atmospheric plasma of the star, thanks to the absorption by thousands of spectral lines on the stellar surface.

Pulsations in AGB stars

The mass loss process for AGB stars is strictly connected to a wide phenomenon of radial pulsations in the star envelope: the so called Mira variables (named on the first star successfully observed during this phenomenon, Mira) or Long Period Variables (LPV), which are a class of AGB stars characterized by periodic change in radius through subsequent pulsations. These stars are characterized by the highest mass loss rates, thanks to the superwind process (wind emission supported by radial waves of matter within the star's radius), which usually leads to the complete ejection of the giant's envelope and white dwarf formation. These stars emit red color radiation and the pulsation is longer than 100 days, with amplitudes between 1 and 2.50 for single radial waves.

The radial waves involve a double change in both radius (10% of original radius) and temperature (1000-1500 K) of the outer stellar layers. Temperature and radius sinusoidal peaks are displaced: the temperature is at its maximum when the radius is at its minimum. The change in density and pressure profile leads to a upper layer dissipation (due to the mechanical energy lost to a levitation process involving the atmosphere of the star) and density enhancement in the lower layers. The formation of dust grains and molecules is highly affected by the pulsations: study of abundant molecules, as SiO (Loidl et al. (1999)) can be related to the stellar pulsations properties, as temperature profile or pressure profile. The pulsation process determines the amount of material from nucleosynthesis activity that will reach the star's surface, and then being expelled: a large fraction of the elements we actually find in the Universe was originated from this stellar phase. The LPVs are divided in different

categories (from the General Catalogue of Variable Stars definition):

- MIRA long period (80-1000 days) variability stars with V-magnitude from 2.5 to 11;
- SRa late-giants with regular period (35-1200 days) and V-magnitude around 2.5;
- SRb semiregular stars with wider range of periods (20-2300 days), showing higher irregularity respect to the SRa;
- Lb irregular period giant stars.

In SRa and SRb it is interesting to notice that the period of the variability depends to the star's evolutionary stage (Jura & Kleinmann (1992)). Low mass loss stars ($M < 10^8 M_\odot$) are characterized by $P < 100$ days. The LPVs are located on the right extreme part of the HR diagram, at AGB phase.

Radial waves mechanism

The mass loss is directly correlated to radial pulsation: but what is the mechanism behind the process? The first solution was proposed by Eddington with a driving Carnot cycle: a thermodynamic engine where a layer inside the star is able to convert heat into mechanic energy. Absorbing thermal energy (heat) at high-temperature layers and releasing it at low-temperature layers, it can produce work. The Carnot cycle on a thermodynamic system is composed of different states and at the end of all returns to the initial one. For each stellar layer, a variation of the internal energy $\frac{dQ}{dT}$ is given by the layer state: applying the Carnot cycle on the layer, it will return to this state at the end of one cycle, with null variations in entropy and internal energy. These are the two conditions for a reversal Carnot cycle.

$$\begin{aligned} \oint dU &= 0 \\ \oint dS &= 0. \end{aligned} \tag{2.4}$$

We obtain work performed by the layer selected over the surrounding layers as a function of (1) the rate at which the thermal energy is injected into it; (2) the variation of the layer temperature itself. To keep $\bar{W} > 0$, it is necessary to transfer energy from the layer at higher temperature to the surrounding layers at lower temperature. The cycle is then driving, and in case of gas, these conditions are reached if the layer absorbs heat when it is in compression phase (hot) and releases it in expansion phase (cold).

However, most stellar layers are damping Carnot cycles, transferring energy in the opposite temperature gradient: they are dissipating. This is the reason why a thermal valve is necessary, which is open in case of expansion and closed in case of compression. In giant star, the parameter that functions as a valve is the opacity κ, which is indeed influenced by temperature:

$$\kappa \propto \frac{\rho}{T^{3.5}}. \tag{2.5}$$

But the mechanism results in an opposite thermal valve as expected: in normal conditions the gas layers in star's interior is not suitable as thermal regulator. It was discovered that only partially ionized regions could create the necessary conditions that allows the thermic valve to work and produce a driving Carnot cycle. A partially ionized region absorbs heat during compression, helping the ionization process in which energy is temporarily conserved as ionization energy in the ionized medium. When the layer expands, it cools down and through re-combination processes it releases energy, then it returns to initial conditions.

The mass loss phase in giant stars, characterized by the superwind effect, usually ends at the end of AGB phase, when the stellar envelope reaches around $10^{-3}M_0$: at this point, the outside layers mass fraction is too low for radial pulsations. The huge amount of ejected material, usually composed of molecules and dust, surrounds the star remnant. In this stage, the star is invisible for optical observations due to the high presence of dusty material. Gas is slowly ionized by the star (T around 30'000K): it starts to cool down and expand in a planetary nebula.
The remnant star, usually composed of C and O, has not the temperature to ignite further nuclear burning: it is the beginning of white dwarf formation. In rare cases, the core temperature of the remnant allows ignition of carbon core, starting successfully a new nuclear burning phase of stellar life. At the end of carbon core burning (which has as secondary products oxygen and neon), the neon/oxygen core has not a sufficiently high temperature to ignite neon: this leads to the formation of a neon/oxygen white dwarf.

2.3 White dwarfs

This section is based on the book from Carroll & Ostlie (2017), regarding evolved stars.

Formation and characteristics of white dwarfs

The evolution in the post-AGB phase is at nearly constant luminosity, while the star's effective temperature increases. The transition time is directly connected to the original star mass, from 100 ys only for higher stellar masses to 10^4 ys for lower mass stars. The ejection of the envelope and formation of the nebula happens at very low mass loss rate ($10^{-8}M_\odot$/ys).On average, white dwarfs are around 6 times less luminous in magnitude compared to the Sun: assuming a limit of magnitude in the V band around 27, the furthest white dwarf we can observe is at 14 kpc. So far, white dwarfs are visible only through Galactic survey due to their low luminosity, and they appear on the left and lower side of the HR diagram as we see in Fig. 2.2.

One of the most prominent ad wider surveys comes from GAIA: a space observatory of the European Space Agency (ESA), launched in 2013 (ESA (2023)). The main aim of GAIA is to gather precise astrometric constraints (position, parallax) of a high amount of stars. Thanks to its research, a precise 3D space map of a total of 1 billion astronomical objects as stars, planets, comets, asteroids and quasars was

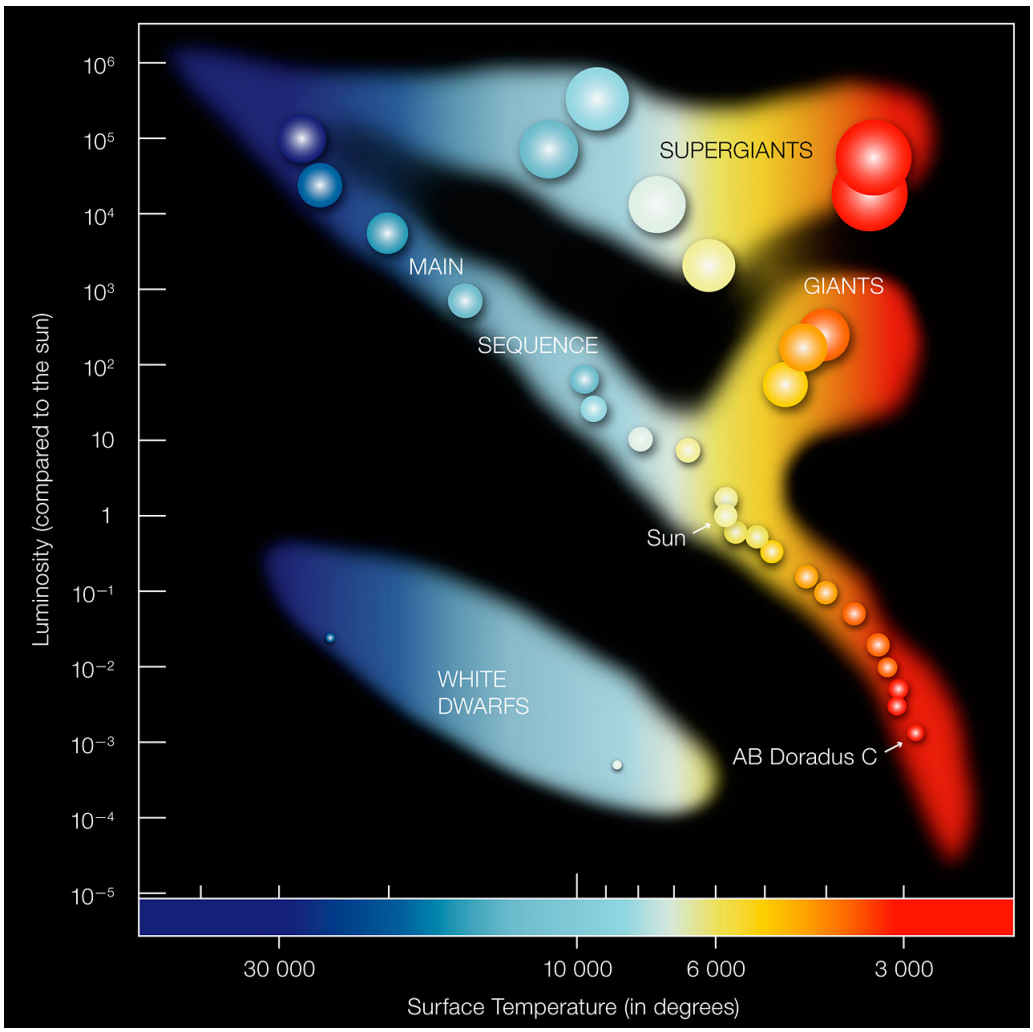

Figure 2.2: *Hertzsprung-Russel diagram: the white dwarfs appear to be on lower left side, where luminosity and temperature are respectively under* 10^2 *and* 10^4 *(ESO (2007)).*

made through the different data releases, collecting also information on luminosity, effective temperature, gravity and elemental composition of the observed targets. To study the precise position and motion of its target objects, the spacecraft monitored each of them about 70 times over the five years of the nominal mission (2014–2019), and continues to do so during its extension (2019-2025). So far, GAIA discovered around 230'000 white dwarfs, thanks to the second and dominant data release in 2018 (Gentile Fusillo et al. (2019)). In the third release, nearly 1.3 million sources were analyzed, and a sample of 359'000 high-confidence white dwarf candidates were selected (Gentile Fusillo et al. (2021)).

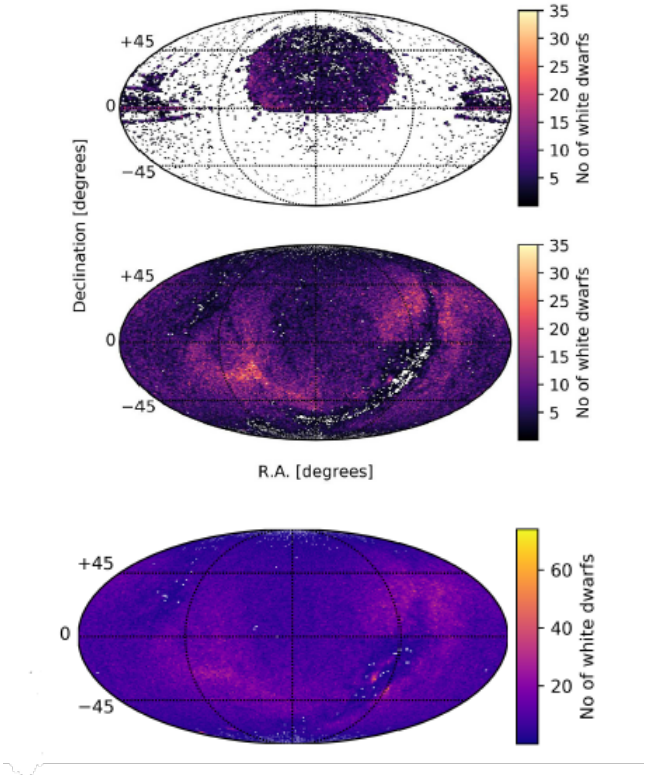

Figure 2.3: ***Top panel:*** *Sky density of the 33'000 known white dwarfs before Gaia DR2 (Gentile Fusillo et al. (2019)).* ***Middle panel:*** *Sky density of Gaia DR2 white dwarf candidates with a* $P_{WD} > 0.75$ *(Gentile Fusillo et al. (2019)).* ***Bottom panel:*** *Sky density of Gaia EDR3 catalogue (Gentile Fusillo et al. (2021)).*

As we saw in the previous section, medium mass stars ($M < 8M_{\odot}$) reaches the end of the AGB phase through a substantial mass loss event, with only a non-active core left as remnant of the original star after the superwind phase. The white dwarf core is an electron-degenerate gas. The momentum of the fermions in the gas generates pressure, termed "degeneracy pressure". Inside the star's core, matter is now composed of positively charged ions (C, He, O) and free electrons, which have been stripped from elements nucle. A low rate of electrons-particles collisions due to the relativistic speed of electrons allows them to travel large distance before colliding: the pressure for a degenerate gas depends only on the speed of the particles and their mass. The pressure tends to decrease the total volume of the star.
Degenerate gas can be compressed to very high densities, typical values being in the

range of 10,000 kilograms per cubic centimeter. The core composition depends on stellar life evolution phases: usually white dwarfs stop the nuclear activity at carbon ignition phase, and main elements of their core are carbon and oxygen, surrounded by a thin atmosphere of hydrogen and helium (as we see in Fig 2.4).

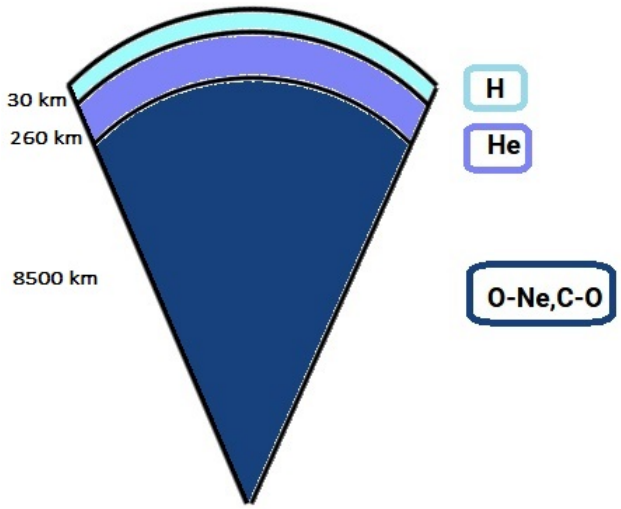

Figure 2.4: *White dwarfs internal structure: an external H-He layer (He resides in the interior part for the atmosphere) represents only 0,03 % of the total radius, while the rest is the core of C/O.*

Carbon and oxygen are produced during the helium burning phase as we see in the following nuclear reactions:

$$\begin{aligned} 3^4He &\rightarrow^{12} C + \gamma \\ {}^{12}C &+^4 He \rightarrow^{16} O + \gamma \end{aligned} \tag{2.6}$$

Usually the atmosphere is divided in two distinct layers of helium ($M_{He} \sim 10^{-2} M_{WD}$) and hydrogen ($M_H \sim 10^{-4} M_{WD}$).

Degenerate gas and the Chandrasekar mass

White dwarfs are characterized by a mass limit above which the core's internal pressure can't support further external gravity due to the star's mass. This limit, called the Chandrasekhar mass, corresponds to approximately 1.44 $M_\odot$ for objects with composition of carbon and oxygen (with two baryons per electron). This mass cutoff is appropriate only for a star supported by ideal electron degeneracy pressure under the assumptions of Newtonian gravity: in general relativity and with realistic Coulomb corrections, the corresponding mass limit is around 1.38 M_0. The limit may also change with the chemical composition of the object, as it affects the ratio of mass to number of electrons present, and with a possible object's rotation speed, which counteracts the gravitational force. The Chandrasekhar limit sets the border

between formation of a white dwarf and more massive and dense objects, such as neutron stars and black holes.

The luminosity of these faint stars is not sustained by thermonuclear processes or gravity, as it happens in active stars. The internal energy is progressively radiated away through ions cooling: since white dwarf core material is a completely ionized plasma (nuclei and electrons), the cooling process is only due to the heat transfer from the inside layers to the outside layers. It is important to remember that the degenerate matter is optically thick (optical depth over 1.0). White dwarfs radiation is caused by the thermal conductivity: the star slowly cools down from 10^8 K to 10^4 K, emitting as a blackbody from the outer shell (10^5K) atmosphere. However, some cases of hot white dwarfs (T surface <30,000 K) have been observed in the soft X-rays band. Usually white dwarfs are cataloged from O/B color emission up to early M stars.

It is possible to derive fundamental relations between the elemental quantities (radius, temperature, luminosity and mass) of white dwarfs. Introducing the degeneracy condition between temperature T and density ρ

$$\frac{T}{\rho^{2/3}} < D = 1.3 \cdot 10^5 K \cdot m^2 kg^{-2/3}. \tag{2.7}$$

we can calculate the star's core pressure due to the electrons from the statistical particle velocity distribution as

$$\begin{aligned} P &= \tfrac{1}{3} m \int_0^\infty N(v) v^2 dv \\ P &\sim \tfrac{1}{3} n_e p v \end{aligned} \tag{2.8}$$

where:

- n_e is the electron' number $n_e = \left[(\frac{Z}{A}) \frac{\rho}{m_H} \right]$, depending on hydrogen mass m_H, gas density ρ, protons' number Z and nucleons' number A;
- the momentum $p = h \left[(\frac{Z}{A}) \frac{\rho}{m_H} \right]^{1/3}$;
- the particles' speed $v = \frac{h}{m_e} \left[(\frac{Z}{A}) \frac{\rho}{m_H} \right]^{1/3}$.

The momentum can be simplified using the Heisenberg principle $\Delta x \cdot \Delta p = h$ as:

$$\Delta p \sim \frac{h}{\Delta x} \sim h n_e^{-1/3} \tag{2.9}$$

where $\Delta x \sim x \sim n_e^{-1/3}$ (since are distinguishable objects) and their position's uncertainty is their separation (on average), so it is directly dependent on density

in volume units. The number of electrons depends directly from the ratio protons over nucleons: we can rewrite it as

$$\begin{aligned} n_e &\sim (\tfrac{Z}{A})\tfrac{\rho}{m_H} \\ p &\sim h\left[(\tfrac{Z}{A})\tfrac{\rho}{m_H}\right]^{1/3} \end{aligned} \tag{2.10}$$

Considering now the speed term, in our regime (non-relativistic) $v = \frac{p}{m_e}$, so:

$$v = \frac{h}{m_e}\left[(\frac{Z}{A})\frac{\rho}{m_H}\right]^{1/3} \tag{2.11}$$

Rewriting the pressure with all terms:

$$P = \frac{1}{3}\left[(\frac{Z}{A})\frac{\rho}{m_H}\right] h\left[(\frac{Z}{A})\frac{\rho}{m_H}\right]^{1/3} \frac{h}{m_e}\left[(\frac{Z}{A})\frac{\rho}{m_H}\right]^{1/3} \tag{2.12}$$

It is possible to obtain a relation dependent on a constant D for white dwarfs relating temperature and pressure (Carroll & Ostlie (2017)):

$$M^{1/3}R \sim 3 \cdot 10^{19} kg^{1/3} \cdot m. \tag{2.13}$$

This is the mass-radius relation for white dwarfs: the higher the mass, the smaller is the radius; massive white dwarfs become denser. Considering a relativistic regime, we easily notice that the mass has a limit value of 1.44 $M_\odot$, which is exactly the Chandrasekhar mass. The mass of an isolated, non-rotating white dwarf cannot exceed this limit, but if in a binary system the star can accrete material from a companion, increasing both mass and density. As its mass approaches the Chandrasekhar limit, this could theoretically lead to either the explosive ignition of fusion in the white dwarf or its collapse into a neutron star.

Cooling function for white dwarfs

Since white dwarfs' surface is small (the radius is usually between 0.8–2% $R_\odot$), they tend to remain hot for a long time and shift to the red part of the spectrum as their temperature decreases. Remembering luminosity $L = 4\pi\sigma R^2 T_{eff}4$ (where $\sigma = 5.67 \cdot 10^{-8} W m^{-2} K^4$ is the Stefan-Boltzmann constant) and the radius-mass relation 2.13, it can be easily derived a logarithmic relation between the three parameters:

$$log\frac{L}{L_\odot} \propto 4log\frac{T}{T_\odot} - \frac{2}{3}log\frac{M}{M_\odot} + c \tag{2.14}$$

For different masses, we see cooling sequences of L-$T_{eff}$where the star are assuming progressively lower luminosity and temperature with time (Fig. 2.5). Unless there is accretion from nearby younger star, the stored energy of the white dwarf is released as radiation and progressively reduced. For a carbon white dwarf of $0.59 M_\odot$, after approximately 1.5 billion years the surface temperature reaches about 7'140

K. The cooling process takes approximately 0.3 billion years to reduce the temperature by 500 K, but below 6'590 K takes up to 1.6 billion years.

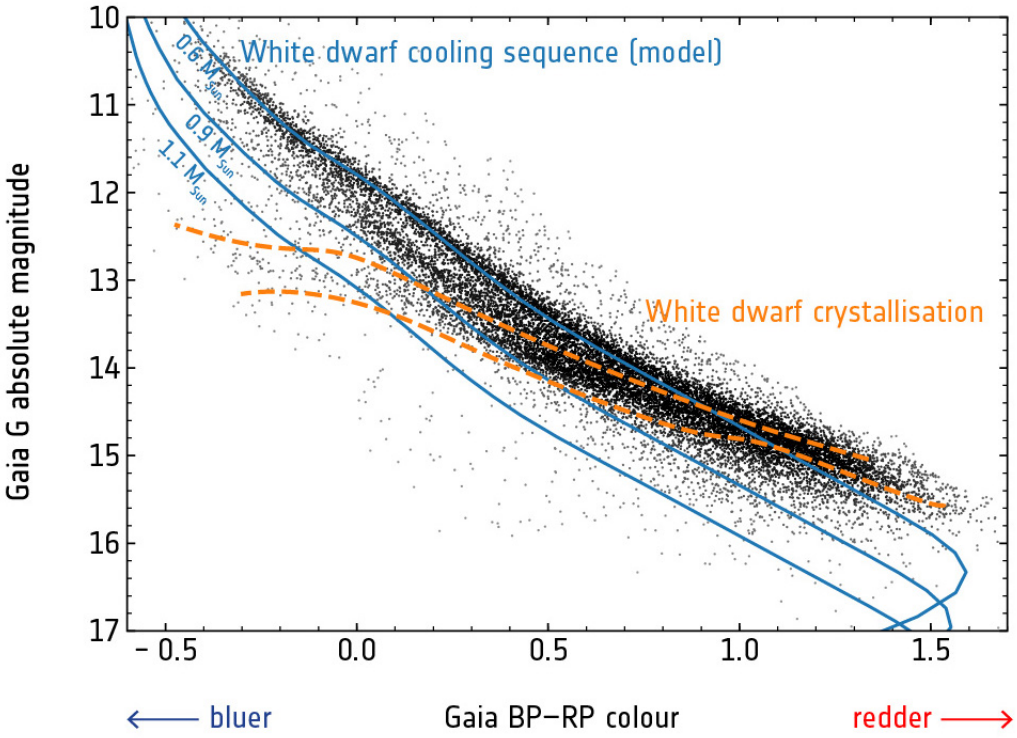

Figure 2.5: *In the plot, as black dots we can see real data from the second release of ESA's GAIA satellite regarding white dwarfs on the HZ diagram (Tremblay et al. (2019)). The blue lines show the simulated cooling sequence of white dwarfs with different masses – 0.6, 0.9, and 1.1 times the mass of the Sun, respectively. In orange lines it is highlighted the white dwarfs population affected by cooling and crystallisation inside the star's core: as expected, they slightly depart from the simulated cooling function for their masses.*

White dwarfs' external layers are in hydrostatic equilibrium, where $\frac{dP}{dR} = -\frac{GM\rho}{R^2}$. The gradient of the core's temperature respect to the radius is as follows:

$$\frac{dT}{dR} = -\frac{3\kappa\rho}{4ac}\frac{1}{T^3}\frac{L_R}{4\pi R^2} \tag{2.15}$$

where κ is the opacity parameter, $a = 7.6 \cdot 10^{16} Nm^2K^4$ is the radiation costant and L_R is the luminosity depending on the radius R. At the border layers of the star the temperature is equal to the core's temperature (the structure is assumed

isothermal), so we can derive a useful luminosity-temperature relation:

$$L = CT_{core}^{7/2}$$
$$C = \frac{4D^3}{17}\frac{16\pi ac}{3}\frac{GH}{k\kappa_0}\mu M_{WD} \propto \frac{M_{WD}}{M_0}. \tag{2.16}$$

This luminosity is completely due to internal stored energy, in form of ions' thermal energy. Then assuming $L_\odot$ the luminosity of the star at initial time τ_0 and remembering the correlation between luminosity and temperature from the Stefan-Boltzmann law:

$$L_{WDsurface} = L_0\left[1 + \frac{5}{2}\frac{t}{\tau_0}\right]^{-7/5}. \tag{2.17}$$

We obtained the Mestel Law, which describes the variation of the white dwarf's luminosity with time (as it is possible to see in the HZ diagram in Fig.2.2).

The luminosity has a very rapid decline then a decreasing plateau, and it is a good approximation model compared to the real data (as it is evident from Fig. 2.5). An apparent deviation from the pattern is visible in the plot: it is the crystallization process in white dwarfs. It was theoretically predicted in the 1960s that, at a late stage of cooling, white dwarfs tend to crystallize into a solid state, starting at their center. The formation of a structure reduces the ions' degree of freedom: latent heat is released from ions' internal energy and the cooling process is delayed. It is called the "dimming" process, which shows the small bump in the cooling function of most white dwarfs. In 2004, thanks to precise asteroseismology observations on an evolved white dwarf (BPM 37093) by Kanaan et al. (2005), it was proved that up to 90% of its structure had crystallized, and through GAIA's data releases a pile up in the cooling sequence of more than 15,000 white dwarfs was observed.

After the beginning of the crystallization phase, a plateau continues until the core is completely solid ($< 90\%$): at this point the star is made of carbon crystals, which composition is similar to diamonds. A standard equation for the cooling time of such stars is:

$$t_{cooling} = 8.8 \cdot 10^6 (\frac{M}{M_\odot})^{5/7} (\frac{L}{L_\odot})^{-5/7} \tag{2.18}$$

As we can see, the smaller the star the shorter the amount of time required for cooling. Most massive white dwarfs (1 $M_\odot$) need around 12 Gys to cool down and reach the plateau.

White dwarfs classification

White dwarfs are cataloged through spectral absorption lines: due to their thin stellar atmosphere and thanks to the important process of mass ejection prior to their formation, usually white dwarfs are characterized mostly by H and He lines. In some cases the star surface is thin enough that it is not possible to detect any other element. The classification is:

Type	Characteristics
A	H lines present
B	He I lines
C	Continuous spectrum; no lines
O	He II lines, accompanied by He I or H lines
Z	Metal lines
Q	Carbon lines present
X	Unclear or unclassifiable spectrum
P	Magnetic white dwarf with detectable polarization
H	Magnetic white dwarf without detectable polarization
E	Emission lines present
V	Variable

Table 2.1: *Classification of white dwarfs types based on their emission lines or secondary features (etc. magnetic field or polarization).*

- 80% DA-type (DA-WD) Broad H Spectral lines
- 8% DB-type (DB-WD) Broad He spectral lines
- 14% DC-type (DC-WD) No spectral lines.

In white dwarfs' atmosphere usually one element is dominant, either hydrogen or helium, up to 1000 times more abundant than any other element. The reason is that, due to the high surface gravity, heavier elements tend to sink while light elements remain on the outside layer, having observable emission lines.

The first classification comes from Kuiper (1941) and various classification schemes have been proposed and used since then. The classification proposed above was introduced by Sion et al. (1983). It classifies a spectrum by a symbol which consists of an initial D, a letter describing the primary feature of the spectrum followed by an optional sequence of letters describing secondary features of the spectrum (as shown in Table 2.1), and a temperature index number, computed by dividing 50,400 K by the effective temperature. In case of uncertain classification, it is usually proposed the symbol "?". DA (hydrogen-dominated white dwarfs) are 80% of the white dwarfs total catalog, DB 16% and only 4% what is not classified in the first two categories, as DB, DC, DO, DZ, and cool DQ.

Chapter 3

Exoplanets: classification and detection

By definition, extrasolar planets are considered planets outside the Solar System: the first confirmed exoplanet was discovered Wolszczan (1994) around a millisecond pulsar. Mayor & Queloz (1995), with the collaboration of Queloz, only PhD student at time, discovered the first planetary system with a main sequence star after the Sun. By September 2023, 5502 exoplanets are confirmed in 4047 planetary systems: of these, 875 systems have more than one planet (NASA (2023)). The criteria defined by the IAU Commission F2 for the exoplanets definition were the following:

- Objects with true masses below the limiting mass for thermonuclear fusion of deuterium (currently calculated to be 13 Jupiter masses for objects of solar metallicity) that orbit stars, brown dwarfs or stellar remnants and that have a mass ratio with the central object below the L4/L5 instability ($M/M_{central} < \frac{2}{(25+\sqrt{621})}$) are "planets" (no matter how they formed).
- The minimum mass/size required for an extrasolar object to be considered a planet should be the same as that used in our Solar System.

So far, the smallest planet outside our planetary system is Draugr (also known as PSR B1257+12 A or PSR B1257+12 b), which is about twice the mass of the Moon. The most massive exoplanet instead is HR 2562 b, about 30 times the mass of Jupiter. Planets with high mass are at the limit of the nuclear fusion ignition of the deuterium, and in most cases might be a brown dwarf as well. Known orbital periods for exoplanets vary from less than an hour (for those closest to their star) to thousands of years. Exoplanets observation are nearly all conducted within the radius of the Milky Way (26.8 kpc), due to the challenge of detection at far distances.

Last fifteen years of research showed a huge diversity in planets shape, mass and composition, through simulated different formation paths from the planetary disks to the planets itself. Most of the numerical simulation are strongly based on the evolution path of the Solar System, but original tracks were necessary to describe peculiar typologies of planets not present within our system radius.

3.1 Detection methods and discoveries so far

In the last twenty years, a variety of exoplanets have been found, most of them not adhering to any of the Solar System planets. The hosting stars are different in characteristics and location in the Milky Way: they include very low mass stars, low metallicity stars, giant stars, and other advanced evolutionary stages such as white dwarfs and pulsars. Planets with resonant motion respect to the star (the same face of planet always directed to the star light) and multi-planetary systems (up to 7 or 8 planets) have been also detected. Most of the information in this chapter is taken from Perryman (2018).

Radial velocity measurements

The radial velocity, or line-of-sight velocity, of a target with respect to an observer (Earth) is the rate of change of the distance or range between the two points: it is equivalent to the vector projection of the target-observer relative velocity onto the relative direction connecting the two points. The motion of a single planet in orbit around a star causes the star to have a reflex motion respect to the system barycentre, resulting in a periodic perturbation due to the planet's motion. Through the observation of star's radial velocity it is possible to estimate the presence of an exoplanet orbiting around it.

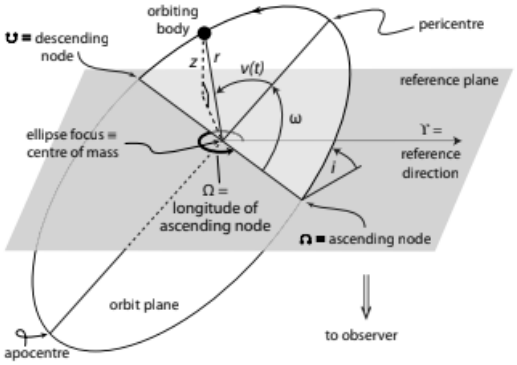

Figure 3.1: *An elliptical orbit in three dimensions, where the reference plane is tangent to the celestial sphere (Perryman (2018))*

If we consider the star orbiting around the system's barycentre as in Fig. 3.1, the star's z-coordinate along the line-of- sight and relative speed are

$$\begin{aligned} z &= r(t)sin(i)sin(\omega + \nu) \\ v_r &= K[cos(\omega + \nu) + e \cdot cos\omega] \end{aligned} \tag{3.1}$$

where z is the star's coordinate along the line of sight, ω is the argument of pericentre (the angular coordinate of the planet's pericentre relative to its ascending node, measured in the orbital plane and in the direction of motion), i is the orbit inclination with respect to the reference plane (in the range $0 \leq i < 180$), ν is the true anomaly (the angle between the direction of pericentre and the current position of the body measured from the barycentric focus of the ellipse), e is the eccentricity and K is the radial velocity semi-amplitude

$$K = \frac{2\pi}{P} \frac{asen(i)}{(1-e^2)^{1/2}} \tag{3.2}$$

The speed is limited between $K(-1 + ecos(\omega)) < v(t) < K(1 + ecos(\omega))$. The relation is usually written depending on the planet's mass as:

$$K = \frac{G}{(1-e^2)} \frac{1}{asin(i)} \frac{M^3_{planet} sin(i)^3}{(M_{star} + M_{planet})^2} \tag{3.3}$$

It is possible to use this technique for single and multiple planets fitting. In case of one planet, the observables are $e, P, t_{pericentre}, \omega, K$; usually also the systemic velocity γ (constant component of the radial velocity of the system's centre of mass relative to the solar system barycentre) and a linear trend parameter d (which may consider also instrumental drifts and unidentified contributions from possible massive, long-period companions) are taken into account. From equation 3.1, the radial velocity signal of a star with an orbiting planet can then be expressed as:

$$v(t) = K[cos(\omega + \nu) + e \cdot cos\omega] + \gamma + d(t - t_0) \tag{3.4}$$

The radial velocity technique is one of the standard detection methods for exoplanets, with the advantage of detecting low mass planets around bright stars. The negative side is that only the $M \cdot sin$ parameter is determined, while orbital inclination remains unknown. For an Earth-mass planet at 0.1 AU the induced radial velocity component would be around 0.9 $m \cdot s^{-1}$

One of the most important radial velocity survey was Keck/HIRES (Doppmann (2008)): an extensive long-term search for extrasolar planets around nearby F, G, K, and M dwarf stars using the Keck Observatory HIRES spectrometer (Mauna Kea). HIRES (High Resolution Echelle Spectrometer) is a grating cross-dispersed, echelle spectrograph operating between 0.3-1.0 microns, with a resolution of 25'000-85'000. Around 60'949 precision radial velocities from 1624 stars obtained over the past 20 years. Some noticeable results were reviewed by Butler et al. (2017) (see Fig. 3.2 for the catalogued stars) : the co-discovery of HD 209458b (the first transiting extrasolar planet by Henry et al. (1999)), the first discovery of a Neptune-mass planet outside the solar system (Butler et al. (2004)), the first direct mass measurement (without isin ambiguity) of Gliese 876 d, the first super-Earth (Rivera et al. (2009)), and many others. The first decade of the survey's productivity was memorialized in 2008, with a then-complete compendium of the orbital characteristics of nearby exoplanets by Cumming et al. (2008).

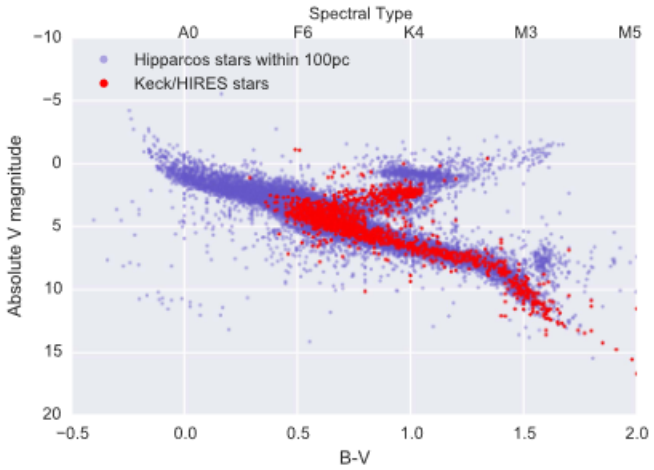

Figure 3.2: *HR diagram for Keck HIRES survey for radial velocities, compared with HIPPARCOS stars selection. From Butler et al. (2017).*

GAIA, mentioned already in Chapter 2, has either a dominant role in astrometry, but also it gave an important contribution in radial velocity measurements. In the DR2 release, the radial velocity data set contains the median radial velocities, averaged over the 22 months of the observations, for 7 224 631 sources. In DR3,around 1 million mean spectra were retrieved from the high-resolution Radial Velocity Spectrometer (Katz et al. (2004)).

Astrometry

The aim of this approach is to determine the transverse component of the displacement of the host star due the gravitational perturbation of an orbiting planet. If the radial velocity technique measures motion of the system' s component , astrometry calculates the coordinates in the sky. Considering a star orbiting around a planetary system barycenter (as in Fig. 3.3), the angular semi-major axis α projected on the plane of the sky is:

$$\alpha = \frac{M_{planet}}{(M_{planet} + M_{star})} \tag{3.5}$$

This astrometric signature α is the observable for astrometric planet detection: it is sensible to long orbital periods ($P > 1yr$).

For a planet $Mp = 1MJ$ orbiting nearby a solar-mass star the median value is 10^3 AU in linear displacement. The main disadvantages are related to the small dimension of the astrometric signature. Also, signature sensitivity drops linearly with the distance. In general, this technique is favorable with larger orbit planets.

The first experiment in space for precise astrometric measurements was Hipparcos (ESA (1993)): it was a scientific satellite from the European Space Agency (ESA), launched in 1989 and operated until 1993. The retrieved Hipparcos Catalogue (Perryman et al. (1997)) was a high-precision collection of more than 118'200 stars with parallax measure, published in 1997. Then also a lower-precision Tycho

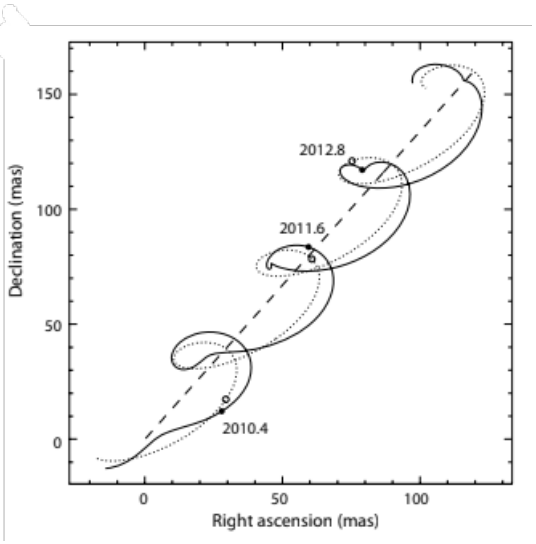

Figure 3.3: *Path on the sky of a star at d =50 pc, orbited by a planet of Mp = 15MJ, e = 0.2, and a = 0.6 AU. The straight dashed line shows the system's barycentric motion viewed from the solar system barycentre. From Perryman (2018).*

Catalogue (in two versions: Høg et al. (1997), Wright et al. (2003)) contained additional 2 539 913 stars. Noticeable results were the a posteriori photometry for HD 209458 b (Robichon & Arenou (2000)) and HD 189733 b (Hebrard (2006)).

The main survey for astrometric signature in the last ten years was conducted by GAIA (ESA (2023)), already mentioned in Chapter 2. GAIA's measurement principles were: 1) observations above the atmosphere; 2) widely-separated viewing directions; 3) a uniform 'revolving scanning' of the celestial sphere. Properties of GAIA respect to other missions are listed in Fig. 3.4. GAIA measures the absolute trigonometric parallaxes and not the relative parallaxes, which is due to the fact is possible to take measures from space (not narrow-field). In Fig. 3.5, the G magnitude (the apparent magnitude of the star seen through the broadest of the Gaia photometric bandpasses) distribution for DR2 release.

Timing

An orbiting planet causes a periodic oscillation of the position of the host star respect to the system barycentre, recognisable through changes in the radial velocity and astrometric position of the star. In some cases, the star itself has a periodic time signature: then it is possible to observe a change in measured star's period. This change is calculated as follow:

$$t = \frac{1}{c}\frac{asin(i)M_{planet}}{M_{star}} \tag{3.6}$$

Stars as radio pulsars, pulsating stars, and eclipsing binaries have this characteristic. In Fig. 3.6 it is possible to observe different paths to the formation of a system pulsating star-planet.

Mission	Launch	No. of	Mag	Accuracy	
		stars	limit	(mas)	(mag)
Hipparcos	1989	120000	12	1	10
DIVA	2004	40 million	15	0.2	9
				5	15
FAME	2004	40 million	15	0.050	9
				0.300	15
SIM	2009	10000	20	0.003	20
GAIA	2012	1 billion	20	0.003	12
				0.010	15
				0.200	20

Figure 3.4: *Summary of the capabilities of Hipparcos and GAIA, along with those of the DIVA (Graue et al. (2003)) and SIM (Catanzarite et al. (2006)) and FAME (Johnston et al. (2000)) astrometric space missions. Numbers of stars are indicative; in the case of SIM they are distributed amongst grid stars and more general scientific targets. From Perryman et al. (2001).*

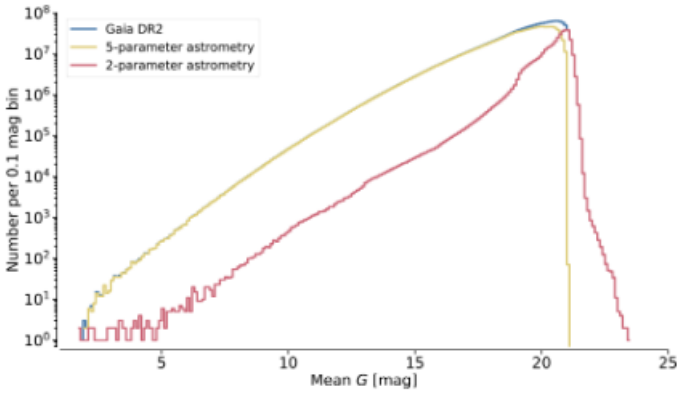

Figure 3.5: *Distribution of the mean values of G for the sources with a full astrometric solution in Gaia DR2 ("5-parameter") and for the sources for which only the celestial position is listed ("2-parameter") compared to the overall magnitude distribution for Gaia DR2. From Gaia et al. (2018).*

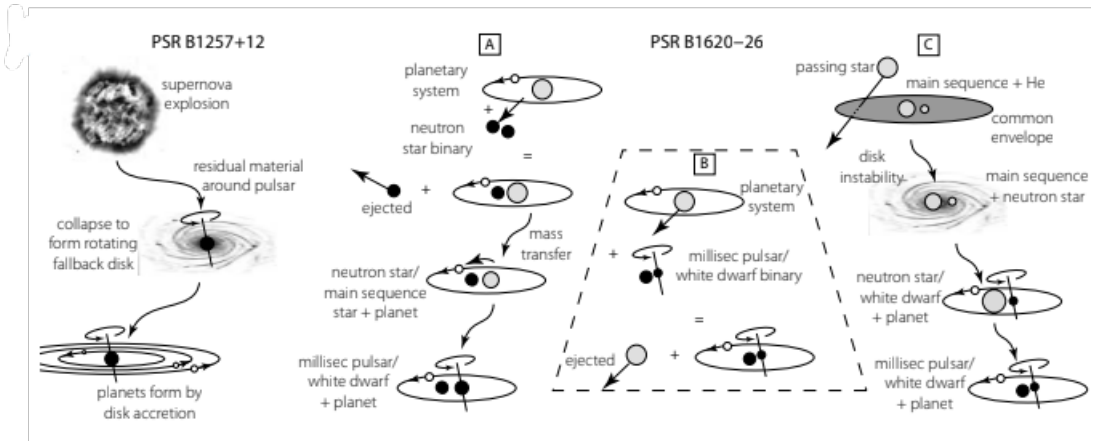

Figure 3.6: *Possible formation ways for pulsar planets.* ***PSR B1257+12:*** *the planet is surmised to have formed from a 'fallback disk' created after the supernova explosion.* ***PSR B1620–26:*** *three options are described. A and B involve different capture-and-exchange scenarios of a pre-existing main sequence star–planet system, while C involves planet formation via disk instability after a passing star disrupts the common envelope of a main sequence/giant binary. From Perryman (2018).*

Some relevant cases of planets orbiting stars with periodic oscillations were confirmed: PSR B1257+12 pulsar with three planets (Rasio et al. (1992), Konacki & Wolszczan (2003)), PSR B1620–26 pulsar with one planet and a binary companion star (Sigurdsson et al. (2008)), G117–B15A white dwarf with one planet (Kepler et al. (2005)), G29–38 with probable planet candidates (Debes et al. (2005)), GD66 with one planet (Mullally et al. (2009)), V391 Peg hot sdB-type star with one giant planet (Silvotti et al. (2007)), HW Vir eclipsing binary including a sdB and a main sequence M star with two planets (Lee et al. (2009)), DP Leo strongly magnetised cataclysmic bina- ry with a giant planet (Qian et al. (2009)) and NN Ser eclipsing binary composed by a white dwarf primary and red dwarf secondary with two planets (Hessman et al. (2011)).

Microlensing

In general relativity, the gravitation lensing is the effect of light distortion due to spacetime variations involving huge masses (etc. stars, black holes). The light rays come from a distant background object (the source) and they are bent by the gravitational potential of a foreground object (the lens) to create images of the source which are distorted. Two different regimes are recognised: strong lensing (the effects are discernible at an individual object level) and weak lensing (effects are discernible only statistically). Strong lensing is further divided into:

- **Macrolensing:** multiple images are resolved (in "arcs").
- **Microlensing:** discrete multiple images are unresolved.

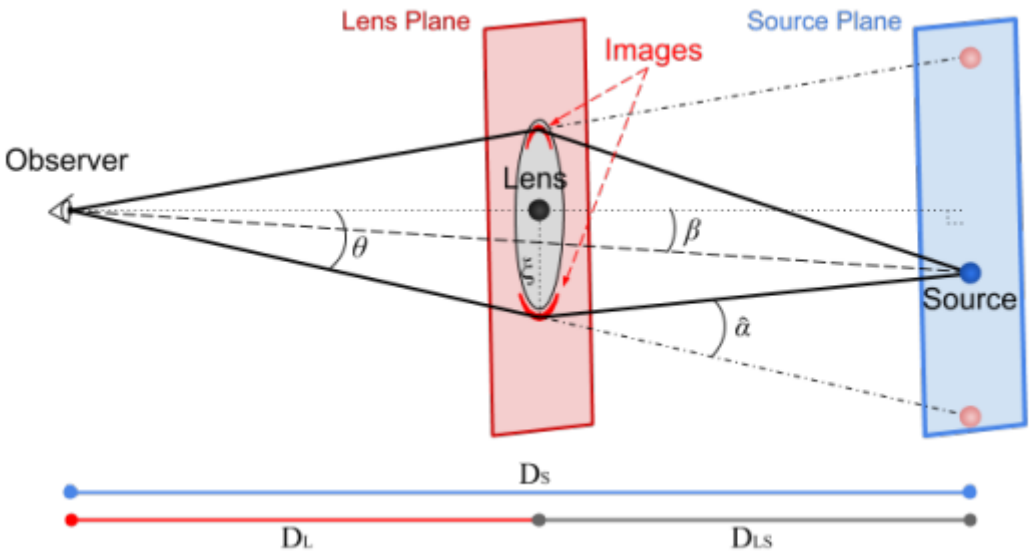

Figure 3.7: *The geometry of a single lens microlensing event. The distances from the observer to the lens and the source are D_L and D_S, respectively. The distance between lens and source is DLS. β is the angular position of the unlensed source, α denotes the deflection angle and θ is the angular position of one of the images. The red and blue rectangles represent the parallel lens and source planes, perpendicular to the observer-lens axis (dotted). From Tsapras (2018).*

The most important equation for lensing is the lens equation:

$$\beta = \theta - \alpha \frac{D_{LS}}{D_S} \tag{3.7}$$

where β is the source position, α angular position of an un-lensed source, θ is the angle between the observer-lens optical axis and the image considered and D_{LS} and D_L are respectively distance from source to lens and from lens to observer. See Fig.3.7 for a scheme of the system.

For exoplanets research, the star-planet system acts as a multiple lens, and a more distant star within the Galaxy acts as the source. Usually, observations are on longer period of time (weeks), allowing a changing in the images magnification due to the variation of the alignment between the observer and the system itself. One issue of this technique is blending: regular blending is the overlapping of two or more stars on the same image to such an extent that the software that performs the photometry cannot identify them individually. The single blurred object dilutes the signal. Also parallax effect is a problem (parallax is a vector with two components in the East and North directions), which becomes non-negligible when the time scale of an event is an important fraction of the Earth's orbital period (months). At last, binary sources can also result in a challenging detection.

Some relevant survey conducted regarding microlensing for exoplanets research were:

- **OGLE**: (Optical Gravitational Lensing Experiment) a Polish astronomical project (Udalski (1997)) based at the University of Warsaw, that runs a long-term variability sky survey (1992–present). The main goals are the detection and classification of variable stars (pulsating and eclipsing), discovery of microlensing events, dwarf novae, and studies of the structure of the Galaxy and the Magellanic Clouds. It has discovered a multitude of extrasolar planets, as the first planet discovered using the transit method, OGLE-TR-56b (Sasselov (2003)). The OGLE survey lasted until 1995, with a total of 19 microlensing events.

- **MOA**:(Microlensing Observations in Astrophysics) a Japan/NZ collaboration that makes observations on dark matter, extra-solar planets and stellar atmospheres using the gravitational microlensing technique at the University of Canterbury (Paczynski (2008)). It is monitoring at present day hundreds of millions of stars every 10–30 min in the direction of the Galactic bulge.

- **KMTNet**: (Korea Microlensing Telescope Networwide) a field photometric system from Korean Space Institute (Kim et al. (2016)), which aims to discover extrasolar planets based on the analyses of gravitational microlensing events. It is focusing on the detection of earth-mass planets in the habitable zone.

Transit detection

The transit technique is based on the fact that light from the host star is attenuated by the transit of a planet across its disk, as it visible in Fig. 3.8. The process is repeated along the orbital period of the planet. As in a Earth eclipse, the shadow of the planet is visible on the hosting star: if the planet is in front of the star respect to the observer, is a primary eclipse; if the planet is behind the star, is a secondary eclipse.
Since 1999 and the first transiting exoplanet (Henry et al. (1999)), planetary systems studied with radial velocity technique were also confirmed in most cases by transit observations. Survey have been carried on until today, looking for periodic attenuation on stars.

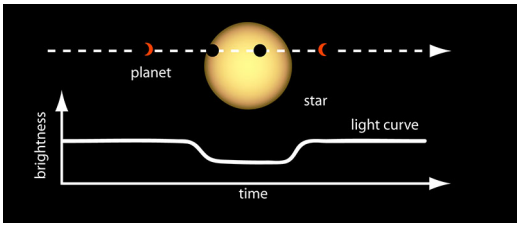

Figure 3.8: *Light curve of a planet transiting the hosting star, from NASA (2022).*

The transit $P_{transit} = \frac{R_{star}}{a}$ (where a is the semimajor axis of the planet, R_{star} the star's radius and $P_{transit}$ the transit's period) depends strictly on the chance that the planet-star system is aligned with the observer. For planets in a short orbit, probability is higher. However, due to the low amount of data on short period planets, this led to a limitation for this technique. From a transit, it is possible to derive directly the planet's radius versur star's radius ratio: this may lead to an estimation of the planet density.

The first theoretical transit technique was already proposed by Struve (1952), and developed by Rosenblatt (1971) (limb darkening). Since it is the oldest detection method for exoplanets, the number of conducted experiment and going-on projects is wide.
Some relevant experiments from the ground:

- **HATNet:** The Hungarian-made Automated Telescope Network Exoplanet Survey (PrincetonUniversity (2003)) is a geographically distributed network of 7 small telescopes optimized for detecting transiting exoplanets. Since first light in 2003, we have discovered 70 exoplanets to date.
- **OGLE:** see Microlensing.
- **MOA:** see Microlensing.
- **WASP/superWASP:** The WASP consortium operates two wide-field camera arrays in the northern (La Palma) and southern (Sutherland) hemispheres (Cameron et al. (2008). Each installation comprises a robotic mount bearing 8 cameras, forming a mosaic with a field of view of 30 degrees in declination by 1 hour in right ascension. Catalogue avalaible at Hellier (2023).

- **XO:**The XO project (McCullough et al. (2005)) aims at detecting transiting exoplanets around bright stars from the ground using small telescopes. The project's first objective is to find hot Jupiters transiting bright stars. It has been operating since 2003 September on the 10,000 foot Haleakala summit on Maui. Up to the first year, it detected 100'000 stars with photometric data.

Some relevant experiments from space:

- **CoRoT:** (Convection, Rotation et Transits planétaires) a space telescope mission which operated from 2006 to 2013, with the goal of observing extrasolar planets with short orbital periods. The mission was led by the French Space Agency (CNES) in conjunction with the European Space Agency (ESA). By 2010, CoRoT discovered a number of confirmed planets, some particularly important as CoRoT–1 b,CoRoT–17 b and CoRoT-7b (first rocky exoplanets). Data from Perryman (2018)).

- **Kepler:** a space observatory launched in 2009 by NASA (NASA/ESA (2009)) to monitor 170'000 stars over a period of four years. The goal was researching for terrestrial planets in the habitable zone through transit technique. It reached 2,600 planet from outside our solar system, of which particularly important are: Kepler-16b orbiting two stars (Doyle (2019)), Kepler-22b first in the habitable zone of a star (Borucki et al. (2012)),the orbital period of the outermost planet in the TRAPPIST-1 system (Grimm et al. (2018)), Kepler-90 largest planetary system discovered (Petrescu et al. (2018)).

- **HST:**(Hubble Space Telescope) a 2.4-m aperture telescope from NASA and ESA(NASA (1990)), was used also to observe known transit events in high resolution. Observations have been made with the Space Telescope Imaging Spectrograph and with the Advanced Camera for Surveys. It detected the first spectroscopic survey of Earth-sized planets in the TRAPPIST-1 system's habitable zone (De Wit et al. (2018)).

- **Spitzer:** from NASA, the Spitzer Space Telescope was launched on 2003 August 25 and working unitl 2009. It has a 0.85-m primary mirror and three instruments: IRAC (Infrared Array Camera), IRS (Infrared Spectrograph) and MIPS (Multiband Imaging Photometer for Spitzer). It concluded the mission in 2020, after 16 years of operations. It reported essential data regarding either exoplanets mass and orbit and asteroid/comets composition.

- **Hipparcos:** see Astrometry.

- **MOST:** the Microvariability and Oscillations of Stars/ was from Canada and it was the smallest space telescope in orbit. MOST was the first spacecraft dedicated to the study of asteroseismology. In addition, it also detected transit of exoplanets.

- **EPOXI–EPOCh:** an experiment carried out using the instruments on board the NASA Deep Impact spacecraft during the cruise phase of its primary mission to rendezvous with Comet P/Tempel 1 (NASA (2005)). This project was to monitor several stars already known to host at least one exoplanet and

to monitor the Earth as a remote source: these were secondary goals respect to the main focus of the mission.

- **TESS:** the Transiting Exoplanet Survey Satellite (TESS) is an MIT-led NASA mission to spend two years discovering transiting exoplanets by an all-sky survey. It is equipped with four highly optimized, red-sensitive, wide-field cameras that together can monitor a 24 degree by 90 degree strip of the sky. It was launched in 2018 and it is still operating. A catalogue of possible life bearing systems was created, the Transiting Exoplanet Survey Satellite (TESS) Habitable Zone Stars Catalog (Kaltenegger et al. (2019)): a list of 1822 nearby stars with a TESS magnitude brighter than 12 and reliable distances from Gaia DR2 (at which the planets would receive Earth-like irradiation).

- **JWST:** the James Webb Telescope (NASA/ESA (2022)) was launched on 25 December 2021 on an Ariane 5 rocket from Kourou, French Guiana. The particular primary mirror consists of 18 hexagonal mirror segments made of gold-plated beryllium, which together create a 6.5-meter-diameter mirror, nearly three times the Hubble Telescope size. atmosphere characterization of transiting planets is one of the goals of the mission. The diameter is about 5.6 times that of HST, and thus JWST will produce considerably higher resolution spectra, especially in the 1-10 microns range (CO, CO2, H2O, and NH3). One of the first investigations into K2-18 b, an exoplanet 8.6 times as massive as Earth, has revealed the presence of carbon-bearing molecules including methane and carbon dioxide: the planet has the potential to possess a hydrogen-rich atmosphere and a water ocean-covered surface (specutils (2023a)).

PLAnetary Transits and Oscillations of stars (PLATO) will be a space telescope from the European Space Agency (ESA (2026)), planned to be launched in 2026.The mission is focused on search for planetary transits across up to one million stars, and to discover and characterize rocky extrasolar planets around Sun-like stars, subgiant stars and red dwarf stars. The emphasis of the mission is on Earth-like planets in the habitable zone around Sun-like stars where water can exist in a liquid state.

3.1.1 Imaging

Direct imaging (detection of the planet's image with a telescope) is technically challenging and so far it has been possible only for rare cases of massive planets. The first and most important step to overcome is to distinguish the planet from the hosting star.
Planets' light is either the reflected light from the parent star (in the visible) or planets' own thermal emission (in the infrared). Calculating the ratio planet/star brightness for reflected light of a specific wavelength λ depends on: stellar spectral type /luminosity class (the more luminous the star and lower the ratio and the more challenging is to detect the planet), the planet's distance from the star, the planet's mass, the planet's composition and radius, possible atmosphere of the planet. It is generically small, around 10^{-10} for Earth–Sun system. In Fig. 3.9, an example of planet-star flux ratio respect to the wavelength for different planets' type.

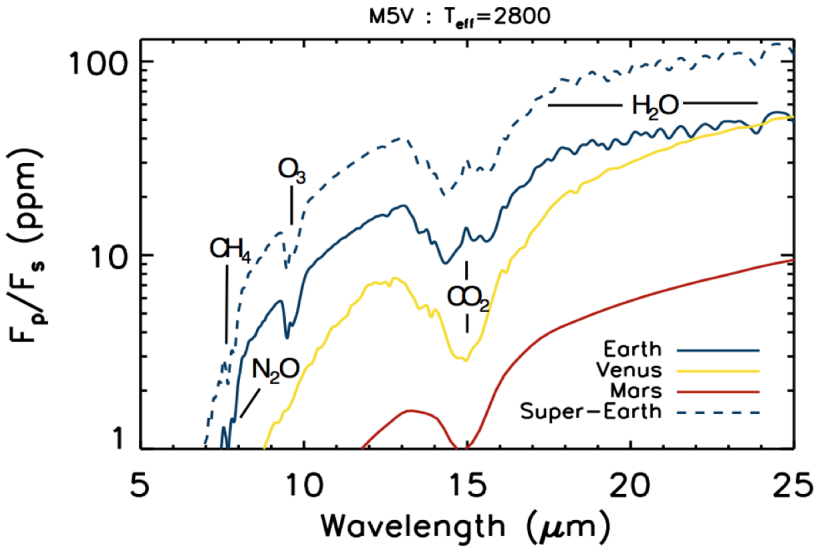

Figure 3.9: *Modeled secondary eclipse spectra in the thermal infrared, shown as the planet-to-star flux ratio in parts per million, for Earth (blue solid), Venus (yellow), Mars (red), and a super-Earth (blue dashed) with an identical atmospheric composition and structure to Earth but with a planetary radius of 1.5 Earth radii. Key molecular features are indicated.From Robinson (2017).*

Regarding the hosting star, a series of targets are considered a good option for imaging:

- Young stars (10–100 Myr, $d < 100$ pc) with young, warm planets and hence self-luminous.
- Stars with known planets.
- Nearby stars, $d < 5$ pc.

Due to the observational challenge of such research, it is fundamental to have a high S/N. One main goal is to attenuate the light from the hosting star. Various solutions have been proposed: large aperture telescopes, adaptive optics (minimisation of atmospheric turbulence), space telescopes, coronagraphic masks (light suppression),post-processing to treat residual aberrations and interferometers (angular resolution improvement).

The main surveys were conducted as ground-based interferometry (VLT, Keck) or space telescope interferometry (HST, Spitzer, but they have not the angular required resolution). ESA and NASA proposed two main missions, Darwin (ESA) and Terrestrial Planets Finder (NASA), both cancelled due to the challenging technical requirements and costs.

3.2 Classification

From the NASA catalogue for extra-solar planets, of 5502 confirmed exoplanets, 1891 are Neptune-like, 1735 are gas giants, 1671 are Super Earths, 198 are terrestrial

and 7 still unknown in features (see Fig.3.11). Of these, 74.8% were discovered with the transit technique, 19.2% with the radial velocity measurements, 3.6% with microlensing and only 1.3% with direct imaging (see Fig. 3.10).

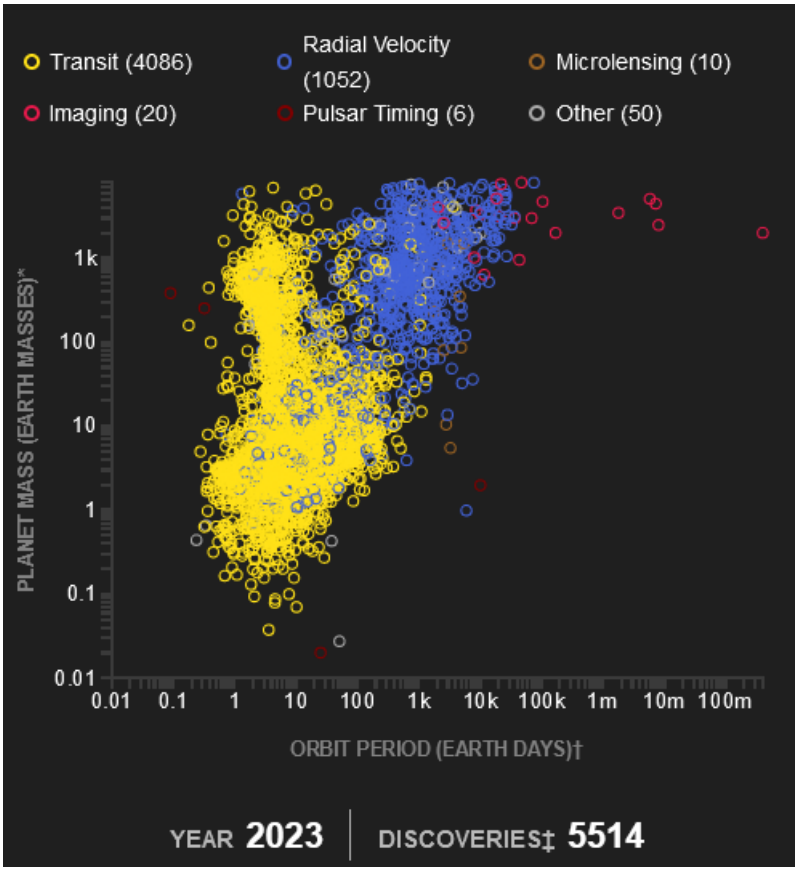

Figure 3.10: *NASA catalog selection (NASA (2023)) through different detection methods, showing visually planet's mass and orbit radius.*

Neptunian planets are Neptun-like objects: they have similar size to Uranus and Neptun (respectively radius 51'118 km and 49'528 km, and mass $14.54 M_{Earth}$ and $17.1 M_{Earth}$) , and they have a mixture of interior compositions. Usually, a hydrogen and helium-dominated outer atmosphere with a rocky core is the standard.
Gas giants are massive planets with an important atmosphere of hydrogen and helium. They are called "failed stars" since they contain the same elements of young stars but they did not reach the necessary core's temperature to ignite nuclear fusion reactions.
Super-Earths are planets 14.5-17 times larger than Earth, but below ice giants dimensions. Terrestrial or rocky planets, as the name says, refer to planets composed of silicates and heavier elements (metals): in our system, Mercury, Venus; Earth and Mars are terrestrial planets.

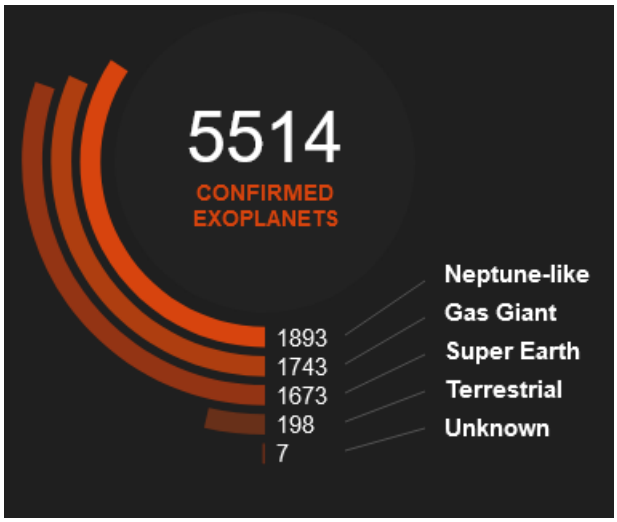

Figure 3.11: *NASA exoplanets' catalog at time of September 2023 (NASA (2023)).*

Chapter 4

Exogeology from polluted white dwarfs

Exoplanets research is drastically limited by the distance of the nearest planetary systems compared to Earth. If the atmosphere could be accessed through high resolution transit spectroscopy, the interior structure is obscure. To discover the geological structure of solid (rocky) planets below the surface, an innovative study from Jura & Young (2014) and Gänsicke et al. (2012) analysed the possibility of tidal destruction and consequent accretion of planetesimals onto evolved stars, such as white dwarfs. The phenomenon is referred as white dwarfs pollution.

4.1 Planets' formation and evolution

Modelling of the thin planet's atmosphere brought the research to confirm two possible exoplanets cases: 1) low-mass, high-density planets (solid) rich in metals and silicates within the core and the mantle; 2) high-mass, low-density planets with thick hydrogen and helium envelopes (gas giants). We are interested in solid planets, as their structure may resemble Earth's geology. Independently from the type, planets are one product of the gas and dust collapse into a protostar in very dense molecular clouds. This process is part of the stellar evolution, typically for medium-mass stars. The section is based on Perryman (2018).

Protostars evolution starts with the gravitational collapse of a cold, high-density molecular cloud. Even if under research, the mechanism is confirmed to be triggered by supersonic turbulent flows within the higher density region. The local density increases until the cloud mass becomes gravitationally unstable. The Jeans criterion for gravitational instability determines, for objects of size λ:

$$\lambda = \lambda_{Jeans} = (\frac{\pi c_s^2}{G\rho})^{1/2} \tag{4.1}$$

where ρ is local density and c_s is the isothermal sound velocity.

At collapse point, thermal pressure cannot resist self-gravity: free fall contraction on an isothermal curve begins, continuing until the core of the molecular cloud is completely opaque. Temperature rises in the region, which is the beginning of the

heating process that will allow nuclear burning and star formation. The accretion rates are 10^9 $10^7 My^{-1}$ for T Tauri stars. The accretion process depends significantly on the angular momentum losses: still not completely constrained, the main parameter considered is the viscosity.

The accretion disk appears around 1 Myr. Protostars with accreting disks are called young stellar objects, characterised by an infrared excess (hot dust) and ultraviolet excess (accretion onto the star). They also show evidence of stellar winds and outflows. Four classes of YSOs are present:

- **Class 0**: sources with a very faint protostar and with a spectral peak in the far infrared or sub-mm region.
- **Class 1**: sources with a spectral energy distribution flat.
- **Class 2**: sources with a spectral energy distribution declining into the mid-infrared.
- **Class 3**: sources with little or no infrared excess.

The protoplanetary or non-accreting disk appears at Class 3 YSOs: the vertical structure of the disk increases in volume, intercepting the stellar photons in the outside layers, where average temperature reaches higher values. A nebula will form from the residuals of the massive accretion disk and planetesimals will grow into asteroids and planets. The composition is mainly hydrogen and helium (similar to the Sun composition). The protoplanetary disks half lifetime is on average 3–5 Myr, and during this range of time planet formation takes place. The disk slowly disappears progressing radially outwards material, removing material from the system through powerful ultraviolet radiation from the central star. The gas in the disk is heated up to 10^4 K and the disk life is around 10^5 years.

The subsequent step is the formation of a debris disk, which was first identified through the infrared excess of α Lyr (Aumann et al. (1984)). Dust and gas from protostar formation and accretion disk conglomerate in a debris remnant disk, which will receive additional material from collisions of planetesimals and asteroids at later stages. The size of these objects is massive: they can reach 500-1000 AU in diameter. Their spectral peak is in the infrared (2 μm-1mm), with a broad black body emission spectrum (which is originated by thermal emission from 1000 K close to the star to 10–30 K near the outer edges of the disk).

4.2 Terrestrial planets

4.2.1 Formation

As we mentioned in Chapter 3.2, terrestrial planets are characterised by a solid structure of heavy elements, as silicates. Planet formation theory predicts that these kind of celestial objects form through agglomeration of disk residuals during

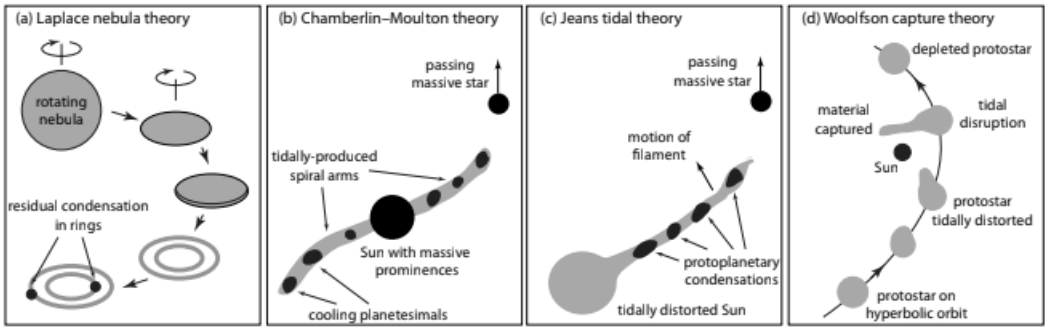

Figure 4.1: *Schematic of alternative mechanisms that have been proposed for the formation of the solar system: (a) Laplace nebula theory, in which the rotating nebula collapses, leaving rings of material in which condensations form; (b) Chamberlin– Moulton planetesimal theory, where high-density regions come from solar prominences drawn out by tidal disruption; (c) Jeans tidal theory, where condensations form in ejected filaments from the tidally-distorted Sun; (d) Woolfson capture theory, showing successive configurations of a disrupted protostar leading to captured material. From Perryman (2018).*

the protoplanetary phase of the circumstellar disk (after the end of the accretion process). It is a bottom-up evolution where bodies increase in size and collide one into another producing more massive planetesimals. The process extends for over 14 orders of size magnitude. The primary and currently used theory was presented by Safronov & Zvjagina (1969) and refined later by Goldreich & Ward (1973), Cameron (1973), Wetherill (1990), Lissauer (1993), Wetherill (1996) and Klahr & Bodenheimer (2006). A series of stages describe the planetesimals evolution in the final rocky planets, as we can see in the next paragraphs. Time scales and processes remain partially uncertain (e.g. dust coagulation, angular momentum transport, the role of magnetorotational turbulence, presence of dead zones, possible gravitational fragmentation). Most of the information in this chapter are based on Perryman (2018).

1) Dust settling Dust is one of the molecular clouds components. During the collapse, the dust grains conglomerate in a dense layer in the central region of the disk due to the presence of electrostatic forces: here multiple collisions allow them to grow significantly in size (Kusaka et al. (1970)). Formation of dust structures was modelled by Weidenschilling et al. (1989) as $m \propto d^2$, with a settling time scale of $10^5 - 10^6$ ys. Detailed collisional and coagulation models in these earliest phases were partially founded on laboratory studies (works from Supulver et al. (1997), Blum et al. (2000), Dominik et al. (2006), Zsom et al. (2010), Brucato & Nuth III (2010)), including the Space Shuttle experiment CODAG (Blum et al. (2002)).
The evolution of dust grains leads to macroscopic objects (rocks) of 0.01–10 m. The main forces involved work radially, so dust grains and smaller bodies, coupled to the circulating gas, orbit the protostar. This leads to Stoke or Epstein drag by the gas on the dust grains:

$$F_{drag} = \frac{1}{2} C_d \pi a^2 \rho v^2 \tag{4.2}$$

Here a is the particle radius, ρ is the gas density, v is the velocity and C_d is the drag coefficient (depending on the particle size). Grains lose angular momentum and they gain an inward motion (drift) with a time scale of 100 years. It is a rapid process: particles and dust grow in size up to 10 m diameter, with the support of increasing temperature and pressure in particular zones which favor the growth process.

2) Planetesimals

Collisions are the dominant evolution for rocks below 10 m in size, leading to a final dimension of 1 up to 3 km. These are planetesimals, and the average duration of this process is around $10^4 - 10^5$ ys. During this step, gravitational interaction is still negligible as the size of the objects involved is small.
The planetesimal size of 1 km represents the point of decoupling from the gas and the starting of gravitational interaction between the different bodies (usually modeled with N-body simulations). Safronov (1972) showed that if the random relative velocity between planetesimals is less than the escape speed from the largest of the them, then that body will grow accreting the other bodies that will collide with it. Planetesimals move in elliptical orbits through gravitational interaction, as objects in a elastic collisions system. As relative velocity increases, the eccentricity of their orbit is higher and leads to inelastic collisions, which have a damping effect on the involved bodies. Balance in the system is reached when the random motion is equivalent to the escape velocity from the largest planetesimal in the group. The protoplanet growing rate is defined as:

$$\frac{1}{M_{planetesimal}} \frac{dM_{planetesimal}}{dt} \propto M_{planetesimal}^{-1/3} \tag{4.3}$$

Considering disk mass of 0.1 M_{Earth} with density varying R^{-1}, timescale for 1 M_{Earth} planet is $4 \cdot 10^6$ys. For Jupiter (10 M_{Earth}) would be 10^{10}ys. As the protoplanet grows, the rate decreases (orderly growth process): most of these objects grow at the same rate, with very long scales of $10^8 - 10^9$ ys.

3) Runaway growth

It is still uncertain which process is involved in the range of size from 1 km to 10 km: usually this phase is around $10^3 - 10^6$ys long. As the protoplanets grow, gravitational interaction becomes dominant in collisions. With higher mass, also dynamical friction between bodies has a significant role in planets evolution: it transfers kinetic energy from the massive protoplanets to the small ones, reducing the velocity dispersion. The growing rate is then:

$$\frac{1}{M_{planetesimal}} \frac{dM_{planetesimal}}{dt} \propto M_{planetesimal}^{1/3} \tag{4.4}$$

It is proportional to the embryo mass: as the protoplanet increases its size, the rate is higher, leading to a runaway growth for the most massive planets. Smaller bodies are accreted or fragmented with the formation of >100 km diameter objects (t= 10^4ys).

4) Oligarchic growth

The planet's Hill radius is the distance within which the gravity of the planet dominates that of other bodies in the system. Large growing mass have an important Hill radius, which can interfere with nearby orbits of smaller planetesimals. The accretion is frequently strongly reduced by the lack of circular orbits around these bodies, which are then not able to accrete more material.
A phase of oligarchic growth starts: massive planets have a constant growth rate, while smaller bodies do not increase in size anymore. The limit mass for oligarchic growth is called the isolation mass:

$$M_{iso} \propto M_{star}^{-1/2} \Sigma_p^{3/2} r^3 \tag{4.5}$$

Here Σ is the local surface density of planetesimals. For a density of 100 kg m^2, the estimated isolation masses are of order 0.07 M_{Earth} for terrestrial planets and 9 M_{Earth} for gas giants.

5) Planets formation

Gravitational interaction is now dominant after reaching dimensions around 1000 km, and catastrophic chaotic impacts are the main reason for major mergers in this phase. Collisions are mainly caused by orbits crossing and eccentricity and inclination increasing. The total rate of growth drops significantly and the process is now inefficient: the final structure of the planetary system is established, while single bodies experience evolution through internal melting process and differentiation of the layers below their surface. Impact types are classified as:

- **Head-on collisions**: frontal impact with a merger of little mass loss, causing extensive heating and the formation of magma oceans (Tonks & Melosh (1992)).
- **Oblique collisions**: impact not on the perpendicular between the two bodies; it may allow separation or even escaping, usually involving exchange of material (Agnor & Asphaug (2004)).

To reach a final quasi-stable configuration we need around 10-100 Mys. The characteristics, including planets position and orbit, depend on various factors: the initial conditions, the viscosity of the protoplanetary disk, the surface density of planetesimals and the existence and migration of giant planets.

The final mass threshold for an object to develop a solid-state convective interior and a geological evolution over time is at diameter of 3500 km (Moon) to 6500 km (Mars) and mass between $7.3 \cdot 10^{22}$kg to $6.4 \cdot 10^{23}$kg. Convection is important at size of 3500 km with mass around Moon's mass: with an average gravitational energy per atom of more than 1eV (limit for chemical reactions), the planet's mass is enough to change chemical composition of the material inside the object. Physical properties changes, due to pressure and temperature, appear at a diameter of 6000 km (rocky planets) or 1000 km (ice planets), when the central pressure due to gravity exceeds the bulk modulus of the material:

$$K = -V \frac{\partial P}{\partial V} \tag{4.6}$$

Usually, the standard mass for pressure to become dominant is around Mars' mass.

6) Interior differentiation

After reaching the mass limit for geological differentiation, elements are divided based on density: iron-like components tend to sink inward due to the very high density, while light elements remain on the surface. The chemical bonds formation between elements allows further differentiation. The interiors structure of the planet's rocks is based on the geochemical classification presented by Goldschmidt & Holmsen (1927) (Fig. 4.2):

- **Litophiles:** those that remain on or close to the surface because they combine readily with oxygen, forming compounds that do not sink into the Earth's core; mostly highly reactive metals.
- **Siderophiles:** elements are the transition metals which tend to sink into the core because they dissolve readily in iron either as solid solutions or in the molten state.
- **Atmophiles:** those that remain on or close to the surface because they combine readily with sulfur and some other chalcogen other than oxygen, forming compounds which do not sink into the Earth's core; usually oxygen low-affinity.

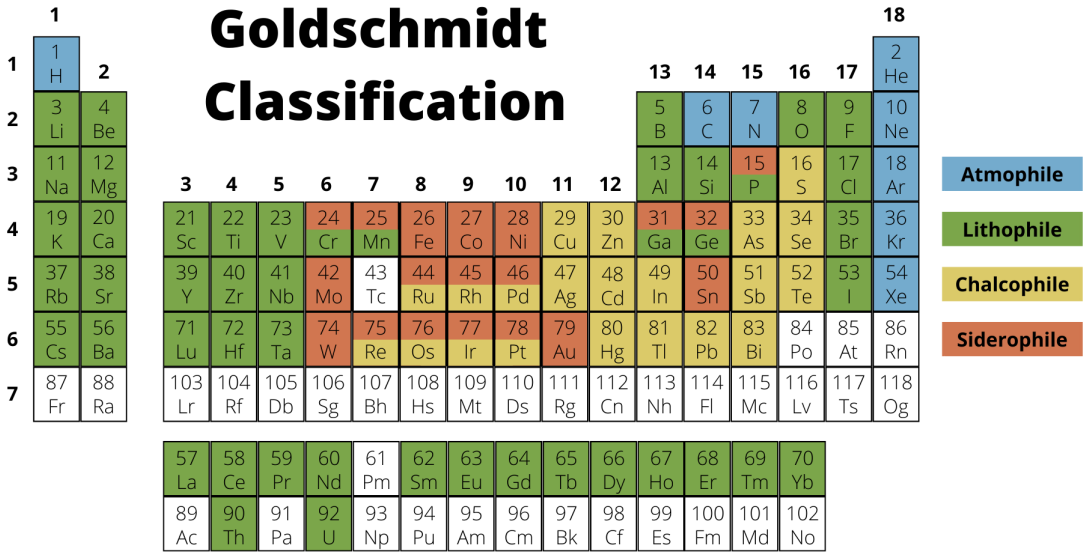

Figure 4.2: *Goldsmith classification for elements in the periodic table: it groups the elements according to their preferred geochemical host phases. From White (2013).*

4.2.2 Planets migration

Planetary systems are not fixed structures in time: migration processes after the formation phase are frequent, and they explain large eccentricities and the large

number of semi-major axes, as a < 0.2 AU (where the formation processes, due to high temperature and low density, would actually be not possible). One and dominant explanation for these values is the planets migration due to gravitational instabilities. The hot Jupiters are an important example: massive gas giants can form at high distance from the star and have a subsequent non-destructive migration inward, leading the planet to a very short orbit respect to the star (Dawson & Johnson (2018)).

The perturbed disk seems to have a dominant role in the orbital migration of the planets and their changes in eccentricity. Calculating the torque on a planet embedded in a 2D debris disk, Goldreich & Tremaine (1982) noticed that the Lindblad resonances (orbital resonance in which an object's epicyclic frequency is a simple multiple of a forcing frequency) produced negative torques which pushes the planet to migrate (Goldreich & Tremaine (1979)). The migrations can be around an order of $1 - 10 \cdot 10^5$ yr migration time for Earth-size planets.

There are two main regimes for planets migration:

- **Type 1 Migration:** the density profile is unperturbed by the migration and the process can be treated as linear ($\mathrm{M} < 10 M_{Earth}$)
- **Type 2 Migration:** the density profile is azimuthally-averaged, modified by planet's mass if massive, leading to domination of the planet's angular momentum over disk's viscous forces; gas is pushed far from the planet and the final orbital evolution is a migration inward. In this case, to have a gas opening the condition

$$\frac{M_{planet}}{M_{star}} \geq (\frac{c_s}{r_{planet}\Omega_{planet}})^2 \alpha^{1/2} \tag{4.7}$$

  (where α is viscosity parameter) must be satisfied, where the possiblity of a gap requires that tidal torques must remove the gas faster than viscosity will allow it to be replenished. This usually happens for disk with $\alpha = 0.01$ and $\mathrm{h/r} = 0.1$, giving $t = 10^3 - 10^4$ yr at for radii at 1 - 5 AU.

A third type of migration exists, consisting in a mixture of the first two types, which is faster and also called "runaway migration". Various researches are investigating the intriguing possibility that a fraction fo terrestrial planets can survive migration during the system's evolution. In particular Mandell & Sigurdsson (2003) suggest that the inward motion of a massive gas planet is not always a threat for the existing terrestrial planets, but this is highly dependent on the initial conditions of eccentricity, orbit and overall system structure , including the disk gas density profile. After the migration, the planets can re-settle in quasi-stable orbits if they were not destroyed or partially damaged by collisions and migration. In addition, it is also possible that the habitable zone will then move inwards or outwards but not completely disappear.

4.3 Elements involved in planets formation

The accretion disk defines the main elements that will form the interiors of the planets within the stellar system. Usually the three most common compounds are (in order of abundance): gas, rock (non-volatile condensate) and ice (volatile condensate). Only in the subsequent evolution the phase of differentation (chemical and gravitational) will then take place.

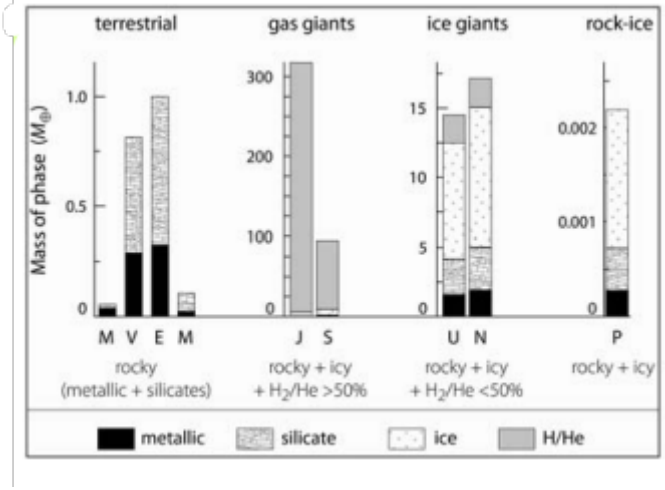

Figure 4.3: *Classification of solar system bodies into four com- positional types, represented by the terrestrial planets (respectively Mercury M, Venus V, Earth E and Mars M), the gas-rich giant planets (respectively Jupiter J and Saturn S), the ice giants (respectively Uranus U and Neptune N) and the dwarf planets (Pluto P). From Lodders (2010).*

GAS Mostly H and He, it makes up to 98% of the original solar nebula. It is the main compound of gas giants, and it can also include some of the noble gases or photochemical pollutants.

ROCK High-temperature evaporation compounds, mostly refractive, are usually the last material to evaporate and separate from gas. They form around only 0.5% of the original solar nebula. Olivine (magnesium iron silicate $(Mg, Fe)_2SiO_4$) is the most common in Earth crust and mantle. In general, the main rocks we find in the Solar System are : olivine, pyroxene (rock-forming inosilicate minerals with the general formula $XY(Si, Al)_2O_6$, where X represents calcium, sodium, iron or magnesium), feldspar (rock-forming aluminium tectosilicate minerals), metal alloys, sulphides, oxides and hydrous silicates.

ICE In planetary science, any volatile with a melting point around 100-200 K is considered ice, including water as expected ($T >> 273$ K). The most common elements forming ices are C, N, O, molecules $CH_4, CO, CO_2, N_2, NH_3$, apart from water.

The Solar System main composition is described in 4.3. We see that the different

objects are divided in three main categories: rocky-materials, gas-rich and ice-rich; only few cases include rock-ice composition (mostly dwarfs planets and moons). The main studies to understand planets interiors' composition within and outside the Solar System without the need of landing on the surface are focusing on:

- Solar nebula composition (starting point of planets formation).
- Dust composition in the interstellar medium and in planetary formation areas.
- Accretion process on planets.
- Gas giants envelopes.
- Super-Earths and rocky planets atmospheres.
- Hosting stars atmospheres.

A study from Lodders (2003) highlighted the possibility of inferring the planetesimals constituents abudances at the end of planets formation through thermodynamical simulation that can calculate the conditions at time of thermochimical equilibrium only through initial solar nebula abundances. In two steps, we can sum up the process:

1. Abudances calculation for each element as follow

$$X_{\Sigma i} = \frac{n(i)}{n_{tot}} \tag{4.8}$$

   where Σ is surface density and i is the i-element we are considering; n_{tot} is the sum of all other gas abundances.

2. Condensate stabilities conditions are calculated applying the chemical reaction for the single molecule. This leads to a condensation temperature for the constituent (some examples in Fig. 4.4).

4.4 Pollution in white dwarfs

White dwarfs are characterized by a thin atmosphere of helium and hydrogen, as mentioned in Chapter 2.3. This is usually due to the process of sinking for heavier elements accreted on their surface. However, if the surface temperature reaches below 20'000 K during cooling, support of elements on the surface due to an upward flow of radiation becomes important (Chayer et al. (1995)). In this case, the sinking time is longer than the white dwarf's cooling age and it leads to the possibility of observe these elements before they reach the undetectable interior. At the beginning, this discovery led to theories of interstellar medium accretion , or comets. Thanks to Jura & Young (2014) (Harrison et al. (2018), Xu & Bonsor (2021)), it is now widely accepted that the pollution is due to rocky planetesimals accretion through three main phases, explained below.

TABLE 7

MAJOR ELEMENT CONDENSATION TEMPERATURES

Ideal Formula	Mineral Name	Solar System Composition (K)	Photospheric Composition (K)
Al_2O_3	Corundum	1677	1665
$CaAl_{12}O_{19}$	Hibonite	1659	1647
$CaAl_4O_7$	Grossite	1542	1531
$Ca_2Al_2SiO_7$	Gehlenite	1529	1519
$CaTiO_3$	Perovskite	1593	1584
$Ca_4Ti_3O_{10}$	Ca titanate	1578	1567
$Ca_3Ti_2O_7$	Ca titanate	1539	1529
$Ca_4Ti_3O_{10}$	Ca titanate	1512	1502
$CaTiO_3$	Perovskite	1441	1429
$MgAl_2O_4$	Spinel	1397	1387
$CaAl_2Si_2O_8$	Anorthite	1387	1378
Mg_2SiO_4	Forsterite	1354	1346
$MgSiO_3$	Enstatite	1316	1308
$CaMgSi_2O_6$	Diopside	1347	1339
Fe	Fe alloy	1357	1351
Fe_3P	Schreibersite	1248	1245
FeS	Troilite	704	693
Fe_3O_4	Magnetite	371	365
H_2O	Water ice	182	181

NOTE.—At 10^{-4} bar total pressure.

Figure 4.4: *Resulting condensation temperatures for a solar nebula, from Lodders (2003), Table 7).*

1) Planetesimal's orbit perturbation after star's evolution Considering a planetesimal/asteroid orbiting an evolving star, during the mass loss phase the planetesimal's period is much shorter respect to the time the star spends in this stage. The angular momentum of the planetesimal is conserved and its orbit perturbed: it migrates outwards without leaving the star gravitational bound. Due to the distance acquired, the planetesimal is safe from the heat and the dragging from the stellar winds.

2)Disk formation The white dwarf forms, and its density is approximately 10^5 times the Sun's density: the gravitational force is strong and can easily disrupt completely an asteroid of mean density 3 g/cm^3 within $1R_\odot$ from the center.
In case a planetesimal is captured in the tidal radius of the star, it is divided in fragments which will be further destroyed by mutual collisions into dust and rocks. The process is similar to the formation of an accretion disk, which is sustained by the maintenance of angular momentum. A UV/optical dust and debris disk will appear around the white dwarf, with a probable double-peaked emission spectrum. Usually only very hot white dwarfs (T $>$ 10′000K) have the chance of form a disk thanks to the higher thermal energy available for disruption. Even if there is an observable correlation between highly polluted white dwarfs and dust disks, the data shows only 1/10 of these stars have a disk.
The disk life is dependent on the angular momentum, which is mainly dissipated though the Poynting-Robertson effect (light from the star is absorbed and then re-emitted by the orbiting material, which then loses angular moment thanks to the

emitted radiation); also viscosity has an important role. As a standard, disk's average life is around 0.4 Myr but with a factor of 10 uncertainty. It was estimated through statistically significant studies by Girven et al. (2012) that, for disk to be formed by planetesimals disruption, the total lifetime of the disk should be around $3 \cdot 10^4$ to $5 \cdot 10^6$ yr. The research was conducted on 53 metal-polluted, helium and hydrogen atmosphere white dwarfs surveyed with IRAC.

3) Photospheric pollution of the star's atmosphere through accretion The debris disk is the main source of accreting material in the star: what is present in the disk is visible on the stellar surface after accretion. Accretion is either continuous (elements' signature always present in the surface) or stochastic (with a non-fixed frequency). It is possible to determine the photospheric abundances from the spectroscopical analysis and the theoretical stellar models. Understanding the original abundance inside the accreted parent body for white dwarfs is easier compared to younger stars, due to the lack of convection zones (which would then mix the interior material with the polluted surface).

To calculate the rate of the mass of the Z_{th} element in the outer mixing zone depending on time we can use as follow:

$$\frac{dM_{star}(Z)}{dt} = -\frac{M_{star}(Z)}{t_Z} + \dot{M}_{PB}(Z) \tag{4.9}$$

where $M_{star}(Z)$ is the mass of the Z-element in the outer mixing zone of the star, $\dot{M}_{PB}$ is the rate of mass loss of the star and t_Z is the settling/sinking time of the element. Solving respect to the time:

$$M_{star}(Z) = e^{-t/t_Z} \int_0^t e^{-t'/t_Z} \dot{M}_{PB} dt'$$

$$M_{star}(Z) = M_{t0}(Z) \cdot e^{-\frac{t-t0}{t_z}} + t_z(\frac{\dot{M_{PB}}}{M_{conv}})[1 - e^{(-\frac{t-t0}{t_z})}]$$

(4.10)

In case of a convective zone (so M_{conv} is not zero), the time t_z would be the time necessary for the element Z to diffuse in the lower layers: for white dwarfs, is the so called "sinking time" that would allow the element to reach under the thin atmosphere and be then not observable anymore. From Koester (2009), it is possible to understand the two main extreme behaviour solutions for the equation 4.4:

1. **Accretion rate is constant and** $t << t_z$: then it is possible to calculate the solution as:

   $$M_{star}(Z) = \dot{M}_{PB} t \tag{4.11}$$

   Considering two elements, we can easily set a ratio that directly reflects the abundance in the parent body:

   $$\frac{\dot{M}_{PB}(Z_j)}{\dot{M}_{PM}(Z_k)} = \frac{M_{star}(Z_j)}{M_{star}(Z_k)} \tag{4.12}$$

2. M_{PB} **constant and** $t > t_z$**:** now the relative settling times are necessary to solve the equation for the abundances as

$$M_{star}(Z) = \dot{M}_{PB} t_z \tag{4.13}$$

The ratio depends strictly on the settling time of different elements, and can vary of a factor of 2 or even 4, since now is depending on an addition ratio of the two settling times $\frac{t_{Zj}}{t_{Zk}}$.

3. **No accretion:** heavy elements still present in the outer mixing zone are depleted at different speed depending on their molecular weight (see 4.5). Settling times were computed by Xu et al. (2013), and it was also clear that the type of white dwarf is a dominant parameter in the final result. These times are referred to hydrogen-dominated atmospheres (DA stars) with T > 12'000 K : in case of cooler DB and DZ stars, the settling times can be longer than 10^6 years. This is the reason why DB and DZ white dwarfs are the preferred targets for pollution.

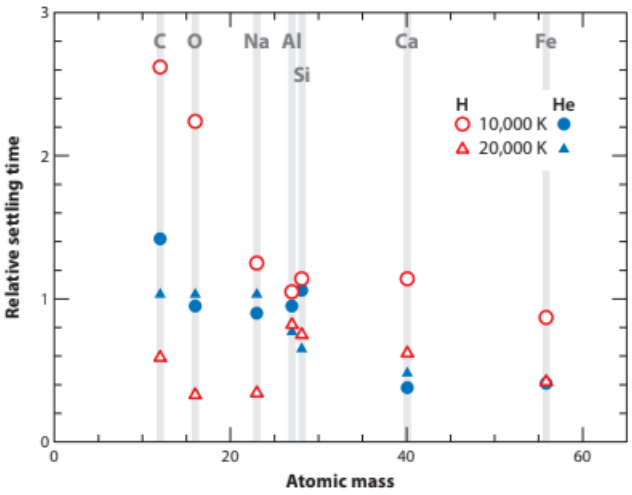

Figure 4.5: *Settling times on a linear scale relative to magnesium's. The red open and blue filled points are for white dwarfs with H-dominated and He-dominated atmospheres, and circles and triangles are for atmospheres of 10'000 K and 20'000 K (from Jura & Young (2014)).*

Is there a limit in the accreted body mass to be visible on the star's surface? In case of DB white dwarfs, Dufour et al. (2012) put a minimum threshold of $4 \cdot 10^{22}$ g (the equivalent of an asteroid of approximately 300 km in diameter , as studied in Klein et al. (2010)). Regarding the accretion rate, usually heavily polluted stars have rates near $10^9 g \cdot s^1$: this would not completely explain why we can see these abundances on the surface.

A significant number of publications reported cases of confirmed white dwarf pollution due to planetesimals disruption/planets disruption. A good number of

cases were observed with the Hubble Space Telescope: it would be interesting also to see how James Webb could also take its place. Among the publications we mention Zuckerman et al. (2007), Gänsicke et al. (2008), Zuckerman et al. (2011), Klein et al. (2011), Gänsicke et al. (2012),Jura et al. (2012), Xu et al. (2013),Xu et al. (2014), Vanderburg et al. (2015) and Klein et al. (2021) (which detected the presence of beryllium in a white dwarf's atmosphere). In detail the elements detected in Chapter 6.1.

Chapter 5

CUBES: the future of VLT in the U-band

In this Chapter, we will present CUBES, the main instrument tested in this project. For further information about the design and development, the consortium's website is from INAF (2023).

5.1 The CUBES project

CUBES (Cassegrain U-Band Efficient Spectrograph) is the study of a ground-based U-band efficient Spectrograph to be installed at the Cassegrain focus of one of the four units (UT2) of the Very Large Telescope (VLT). The main goal is reaching up to 40% efficiency from the slit to the detector (included) and resolving power of 20,000. The first project came from the Brazilian-ESO consortium in 2012, in collaboration with IAG/USP and LNA/MCTI. The project has been revised in 2020 and a new Consortium led by INAF was selected to carry out the study.

The Phase A study has been successfully concluded and the project is now in the Preliminary Design Phase (Zanutta et al. (2022)). The Phase A study, which includes system design, science performance evaluation and embryonic development of the DRS, was conducted to choose entrance aperture, wavelength coverage, resolving power, SNR, manufacturing and system constraints and investigation of when the instrument is background limited compared to the expected detector noise.

5.2 The U-Band

The U-Band in Astronomy includes the range between 320 nm and 400 nm. In the UBV photometric system, the U filter has the effective midpoint wavelength at 365 nm, in the Ultraviolet band. The Ultraviolet band is characterised by three different wavelength ranges:

- UVA (400-320 nm) is a long-wave radiation not absorbed by the ozone layer, usually named the soft UV.

- UVB (315-280 nm), which is mostly absorbed by the ozone layer.
- UVC (280-100 nm) is the shortest UV band, a ionizing radiation completely absorbed by the ozone layer.

The ground-based UV astronomy, which works mostly between 300-400 nm due to atmosphere absorption, is rich in elements and molecules emission lines. Both light and heavy elements (Fe, Be, etc..) can be found in this range, and this led the U-band to an important role in stellar physics. Abundances can be calculated for different star types, but the difficulty increases for faint stars, due to a lower line intensity in the spectrum.

The Multi-Object Spectrograph for Astrophysics, Intergalactic Medium and Cosmology proposed that a new instrument would cover, in optimised mode, the 300-400 nm frequency range (Cristiani et al. (2022)). Several VLT spectrographs already cover (partially or entirely) the U-band, but with limited performances in terms of spectral coverage, sensitivity and/or spectral resolution. Hence, the need of an efficient medium-resolution spectrograph optimized for observations from 400nm down to about 300 nm (the atmospheric cut-off) has been considered a priority within the third-generation instrumentation at the VLT. It is also worth mentioning that the ESO Extremely Large Telescope (ELT) will have limited efficiency in the U-Band due to the chosen mirror coating (protected silver Ag+Al), which maximizes performances in the red and infrared.

5.2.1 Science cases

CUBES is designed to both study galactic and extra-galactic astrophysical cases, briefly summarized below.

- **Cometary science(Opitom et al. (2023))**: the gas coma of a comet contains a large number of emission features in the near-UV range covered by CUBES (305-400 nm). It would be possible to study the ices in its nucleus and the chemistry in the coma. Elements as Fe and Ni, molecules as OH, NH, CN and ions as CO+2, CO+ and N+2 are observable at these wavelengths, in particular metals and the N2/CO ratio.
- **Beryllium abundances (Giribaldi & Smiljanic (2023))**: globular clusters are essential to study early chemical evolution of galaxies. They usually host multiple stellar populations that show a variation of light element abundances, due to various episodes of star formation. Any variation in the abundance of beryllium (313nm line) in young population of stars allows to study the chemical evolution of the population itself.
- **Stellar nucleosinthesis (Ernandes et al. (2023))**: the near-UV domain (300-400 nm) is rich with diagnostic lines from both light- and heavy-elements, allowing precise spectroscopy on a wide range of different stars. CUBES will focus on the study of neutron-capture elements (the s-r processes) to investigate stellar nucleosynthesis processes.

- **Young stars accretion and outflows (Alcalá et al. (2023))**: the circumstellar disks evolves and forms protoplanets with an important influence by the processes of mass accretion onto the central star, ejection of outflows and photo-evaporation in winds of the disk material. So far, in the U-band, due to low sensitivity and limited spectral resolution, Young Stellar Objects (YSOs), in the radius of 500 pc respect to the star, observations have been limited, but CUBES can address this topic in the future.

- **Stellar populations and UV upturn(Ali & De Propris (2023))**: early-type galaxies (ETGs) are evolved galaxies with stellar population mostly comprised of old main sequence (MS) and red giant branch (RGB) stars. They usually manifest a gradual rise in the UV spectra around 3000 Å and down to the Lyman limit: so far, the origin of this phenomena is still uncertain. CUBES can accomplish deep observations of ETGs in the local Universe, due to many UV lines accessible from the ground (NH at 3370 Å and CN at 3383 Å).

- **Cosmological missing baryonic mass (D'Odorico (2023))**: the ratio between standard and dark matter, in our Universe is $fb = (\Omega_b/\Omega_m) = 0.16$. This ratio is not conserved in cosmological evolution of the Universe, since at $z \sim 0$ a baryonic fraction of 30 - 40 % is missing on cosmological scales. With cosmological hydrodynamical simulations, the missing fraction is predicted to be mostly contained in the Universe gaseous components. CUBES, due to higher sensitivity, can be used to observe Hi Lyman-α lines at $z = 1.5 - 2.3$ redshift range, immediately after the era of peak star-formation in the Universe, with simultaneous observation of the metal absorption lines, as C IV and Si IV, to understand the mass in the hot/warm components.

- **Molecular hydrogen in absorption at high redshift (Balashev & Noterdaeme (2023))**: molecular hydrogen (H2) is one of the most abundant molecule in the Universe. CUBES, due to higher sensitivity in the 300-400 nm range, would allow: 1) increase of the gas sample by an order of magnitude; 2) reach of extreme and elusive environments (e.g., more dusty and molecular rich).

The main focus of our project are polluted white dwarfs, which became a possible science case for CUBES only in 2023 from Evans et al. (2023). Characterising exo-planets and understanding their formation and evolution are now major research areas. Nevertheless main-sequence stars, which have a high luminosity compared to the rest of the planetary system, are the main drawbacks for observing the planets' characteristics.
White dwarfs are faint and require high-throughput high-resolution spectroscopy (R > 20'000). The current state-of-art for studies of the bulk compositions of exo-planets are VLT-UVES (ESO (2023a)) and Keck-HIRES(Doppmann (2008)), with strong limitations on magnitude (V < 16 to 16.5 mag), and X-Shooter (ESO (2023b)), which has an important drop in the spectral resolution below 350 nm.
CUBES will cover the range 305-400 nm, with the aim of acquire as much data as possible on exo-planetesimal compositions to reach the values of meteorite samples, which are the only other path to study the core of planets outside the Solar System.

5.2.2 Technical requirements

The top level requirements (TLRs) for CUBES are as follows.

- **Spectral range:** CUBES shall provide a spectrum of the target over wavelength range of 305–400 nm in a single exposure, with the goal of reaching 300–420 nm.
- **Efficiency:** The efficiency shall be more than 0.4 for 305–360 nm (with a goal of more than 0.45 and more than 0.5 at 313 nm), and more than 0.37-0.4 in the range 360-400 nm.
- **Resolving power (R):** CUBES must reach an R above 19 000, with an average value above 20 000 in any part of the spectrum. R is calculated as the full width at half maximum (FWHM) of unresolved spectral lines of a hollow cathode lamp in the spectral slice.
- **Signal-to-noise (S/N) ratio:** In a 1-hour exposure the spectrograph shall be able to obtain for an A0-type star of U = 17.5-18 mag at S/N = 20 at 313 nm for a 0.007 nm wavelength bin.

Goal developments in the Phase A study were also an additional observing mode at a lower spectral resolution of 7,000, to enable background-limited observations of faint sources where spectral resolution is less critical, and an extra-fiber feeding the UVES spectrograph to allow simultaneous observations at longer wavelengths (like for example in case of observations of transients).

5.3 The instrument

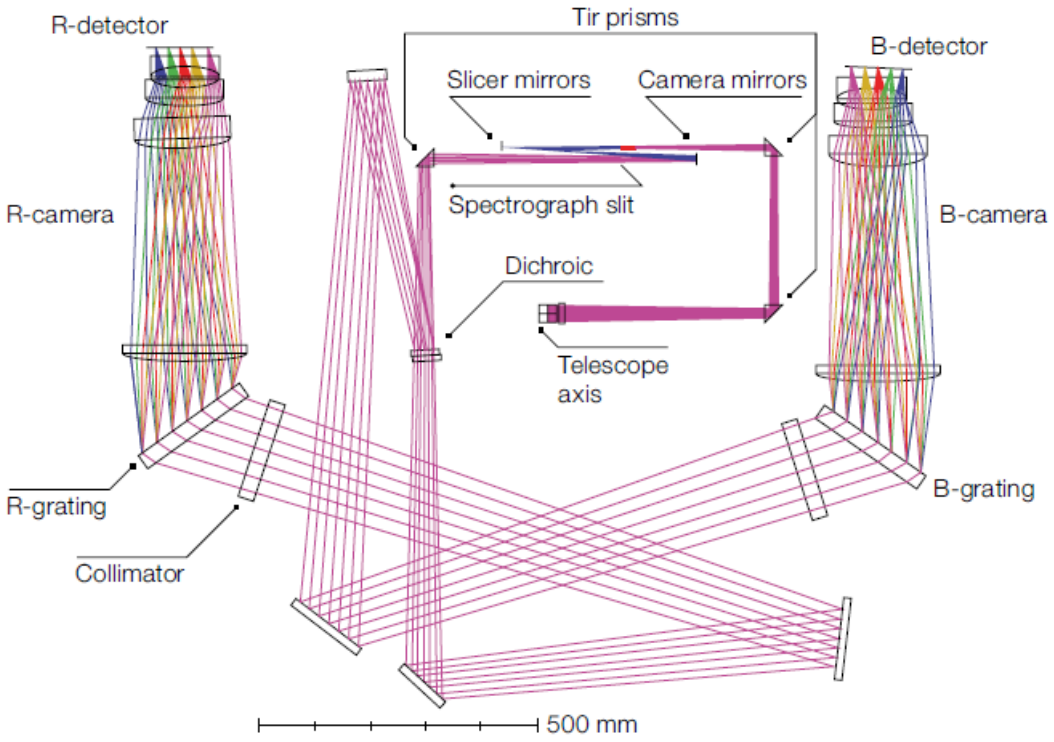

Figure 5.1: *CUBES schematic design: DC - dichroic, P - pinhole, Ps - series of pinholes, AG - Acquisition and Guiding, AFC - Active Flexure Compensation system, FL - fiber link, ADC - Atmospheric Dispersion Corrector. Optional modules (TBD in Phase-B) are marked with a trefoil sign. From Zanutta et al. (2022)*

CUBES has two main instrument's subsystems: the fore-optics and the spectrograph. In addition, a calibration unit and a fiber link to UVES are part of the instrument assembly. A schematic design of the instrument in Fig. 5.1.

The CUBES' baseline is divided into five main elements, which compose the light path:

- **FORE-OPTICS** The optics system provides a collimated beam for the Atmospheric Dispersion Corrector (ADC) and the optics, in order to feed the image slicer.
- **ACQUISITION AND GUIDING(A& G)** Another CCD camera is located near the telescope focus: its goal is providing a more accurate positioning of the target, to account for offsets between the reference frame of the telescope from the Field of View (FoV) of the instrument.
- **IMAGE SLICERS** Two interchangeable slicers enable different spectral resolutions: a high-resolution (HR) slicer to reformat the rectangular 1.5 × 10 arc-

sec FoV to generate the spectrograph entrance slit, and a second low-resolution (LR) slicer with a FoV of 6 × 10 arcsec.

- **SPECTROGRAPH** The spectrograph includes a dichroic beamsplitter to spectrally separate the full bandwidth into two arms, with for each arm: two fold mirrors, a collimating lens, a transmission grating for the necessary spectral dispersion, a camera to focus the spectrum on the detectors.
- **DETECTORS** Two CCDs (one for each arm) mounted in separate cryostats have the function of main detectors.

5.3.1 The fore-optics subsystem

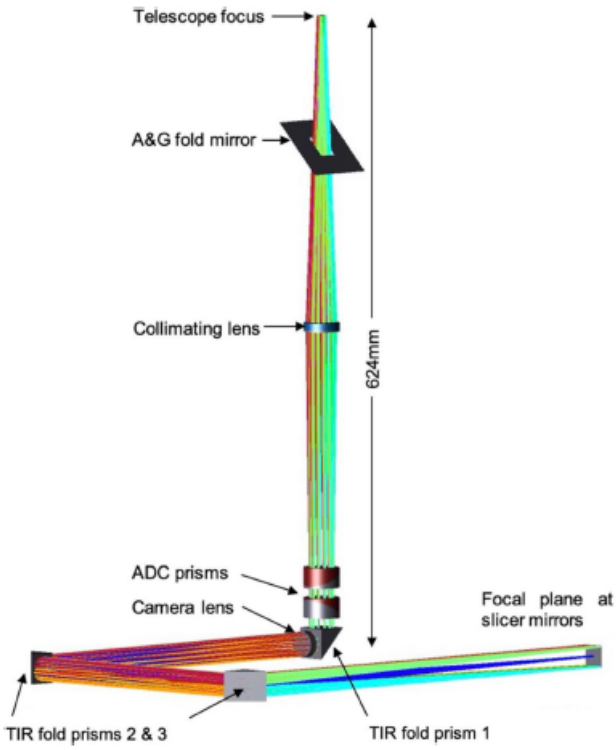

Figure 5.2: *CUBES design: here the optical light path through the fore-optics system. From Zanutta et al. (2022)*

The light path begins at the fore-optics (a schematic view of the light path through the optics is shown in Fig.5.2): after the telescope focus and the instrument shutter, the moving calibration mirror injects the light from the calibration unit. Next, a pin-hole mask is included for alignment purposes and to check the focus during operations. Here there is also an insertable dichroic relays longer-wavelength light to the Fiber Link, allowing the instrument to work in a double mode with UVES (simultaneously), if required. Then a collimator doublet provides the parallel beam for the atmospheric dispersion prisms (ADC), two counter-rotating prisms of 30 mm in diameter, located next respect to the mirror (the material is fused silica/CaF2). Both input and output faces of the prism pairs are tilted at an angle of 0.90° with

respect to the rotation axis, while the angle of the common surface is at 25.22° to the rotation axis. The camera lens has the focus at the input of the image slicer. All foldings of the science beam are obtained by total internal reflection prisms (TIR), to maximize the throughput.

5.3.2 The Image Slicer

The Image Slicer unit is located after the atmosphere correction prisms. It reformats the FoV to generate narrower entrance slits, so it can transmit the light to the spectrograph, achieving the proposed resolution (R=24'000) without the need for adaptive optics and reducing the size of the optical components of the instrument. With a low-resolution mode (R= 7000), CUBES increases the amount of light from the source entering the effective slit, having then higher sensitivity: with a second interchangeable large slices unit, the low-resolution is enabled, and can also cover a wider sky area. The Image Slicer field of view is shown as an example in Fig.5.3 below.

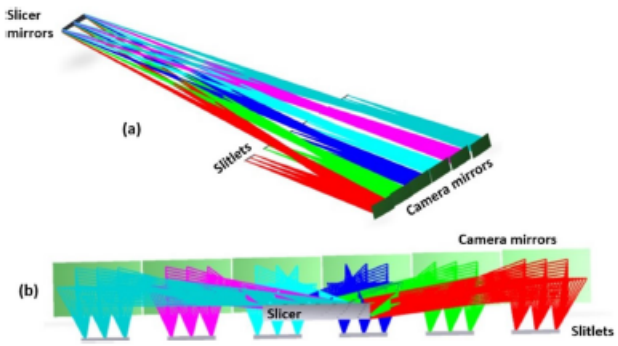

Figure 5.3: *The images of the six slices of the field of view generated by the image slicer, slitlets, compose the spectrograph entrance slit.From Zanutta et al. (2022)*

The baseline of the CUBES design includes two image slicers, due to the requirement of a low and high resolution mode. The image slicers generate the entrance slit for the spectrograph, whose length was calculated to be 10arcsec. This is sufficient to obtain, in standard seeing conditions, sky spectra up to a distance of at least five times the seeing disk away from the center of a point-source on both sides of the target. To maximize the throughput, each image slicer has only two arrays of mirrors: the slicer mirror array and the camera mirror array. The slicer mirror array is placed at the telescope focus, that is re-imaged and magnified by the fore-optics. This allows wider mirrors, reducing manufacturing complexity and costs. This array has six spherical mirrors, each one of them with different tilt angles to reflect a slice of the field towards a camera mirror. So far in the design of CUBES, all slicer mirrors and all camera mirrors have different radius of curvature. Between the two arrays, an intermediate pupil image is generated due to the power of the slicer mirrors. The camera mirrors, also spherical, then focus the beams at their focal length. Each camera mirror produces a portion of the spectrograph entrance slit (slitlet) and places the exit pupil at the diffraction grating position. Despite having sliced

the field of view, the pupil is recomposed on the grating by the overlapping of all the pupils generated for each slice. The width of the slit is different for each resolution mode and so is the field observed.

5.3.3 The spectrograph

Another dichroic mirror after the Image Slicer allows light to be fed to the two arms of the spectrograph that collimate the beams, provide the dispersing function using transmission gratings, and use cameras to focus the spectra on the detectors. An Active Flexure Compensation system (AFC) is considered in the design, to avoid loss of resolution due to a varying gravity vector observation. The spectrograph sub-system is composed of two arms with common optics before a dichroic, which splits the light in two bands: by reflection in the Blue-Arm (300 – 352.3 nm) and by transmission in the Red-Arm (346.3 – 405 nm). The input slit consists of six slitlets, one for each slice in the image slicer (0.25 × 10 arcsec on the sky in HR mode, and 1 × 10 arcsec in the LR mode) and three fiber sources (two for simultaneous wavelength calibration and one for the AFC). The slices have a dielectric coating which is expected to reach 90% efficiency. The two arms have different individual components (all in fused silica) and single separations to achieve the required dispersion, magnification and image quality for the two passbands. CUBES uses first-order gratings produced by microlithographic techniques with an average efficiency of 85% over the whole wavelength range. The spectrograph camera is composed of four lenses, the last of which leads directly to the detector cryostat. The optics are four of spherical shape and four instead have modest conic constants (between -1 and 0.560); the correction for thermal changes in the focus of the spectrographs is done using the first three lenses as single moving unit. The science CCDs are tilted by 3.80° and 2.45° for the blue and red arms, respectively. If needed, the AFC will be implemented by moving the collimator lenses.

5.3.4 The mechanics

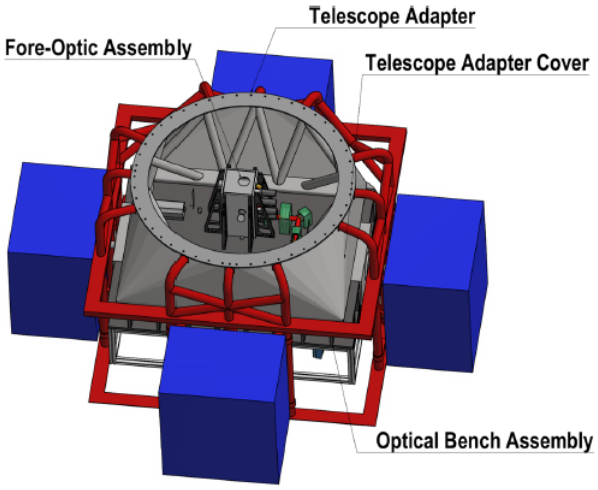

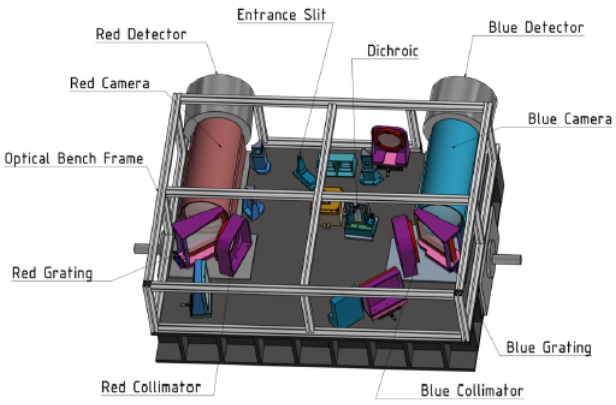

Figure 5.4: *The mechanical design for CUBES. On the top, the general layout. On the bottom, a map of the components of CUBES on the main bench: the Fore-Optics Assembly is located near the center of the bench, while the spectrograph opto-mechanics are 'hanging' on the bottom side. From Zanutta et al. (2022).*

The instrument CUBES, with a designed beam diameter of 160 mm, is fairly large compared to other Cassegrain instruments (e.g. X-Shooter with a 100 mm beam diameter). Therefore, scaling classical instrument designs to the required size of CUBES would then exceed the mass limit of 2500 kg for Cassegrain instruments of the VLT Unit Telescopes. To fix the issue, it was necessary to use light-weight construction principles and select modern composite materials. In the optical layout all the optical elements of the spectrograph, from slit to detectors, lie in a single plane: in this way all the spectrograph optics can be mounted on a single optical bench (1.3 × 1.7 m), which is arguably the most stable configuration and focus also on avoiding gravitational bending, since the dispersion direction of CUBES is parallel to the stiff surface plane of the optical bench. In the current design, the CUBES mechanical structure is divided into three main components, visible in Fig.5.4:

- **Telescope adapter**: it provides a connection between the Cassegrain telescope flange and the optical bench.
- **Optical bench assembly**: a stable platform for the spectrograph optics/fore-optics.
- **Support frame assembly**: a support for auxiliary equipment (the electronic racks, the calibration unit and vacuum equipment); it is detached from the optical bench to mitigate additional flexure contribution.

5.3.5 The Fiber-Link Unit

A fiber link to UVES, the two-arm high-resolution echelle spectrograph located at the Nasmyth B focus of VLTUT2, was designed. To enable simultaneous observations with UVES, the CUBES fore-optics will be equipped with a front-end (FE) module that feeds up to seven optical fibers with: 1)stellar source 2) sky-background 3) a calibration light. The optical fibers have a 120 μm core, which subtends a 1-arcsec aperture on the sky. The light is picked-off using a dichroic mirror that can

be moved into the telescope beam: this will divert light at a wavelength larger than 420 nm and move it to the FE module. The FE module will contain subsystems for: 1)field stabilization (tip/tilt) 2) ADC 3) fiber guiding. The relay optics of the module convert the native F/13.41 telescope beam into an F/3 beam to minimize the loss due to focal ratio degradation (degrade the incident f-ratio to faster output f-numbers, characteristic of optical fibers). A 40 m long fiber cable installed at the UT2 telescope will transmit light from the Cassegrain flange to UVES, where the pre-slit optics relay the UT2 Nasmyth beam into its blue (300–500 nm) and red (420–1100 nm) arms. The injected light from the CUBES fibers will be directed into the red arm through a fold mirror, located on the back of the dichroic mirror (which splits the light into the two wavelength bands). This procedure was already used in a similar way in FLAMES fiber-feed to UVES, for the red arm.

5.3.6 The calibration unit

The calibration subsystem have different kind of light sources to register frames for flat fielding, wavelength calibration, the simultaneous wavelength calibration, alignment and the possible AFC option. The unit will be located on one of the side cabinets and will feed light into the spectrograph with two different paths:

- on the fore-optics by using a folding mirror (for daytime calibrations);
- at the slit level (for the sides of the science spectra, especially when taking simultaneous, night time calibrations).

Two ThAr lamps (one dimmed for simultaneous calibration), one Hg lamp and one Laser Driven Light Source (LDLS) for a near UV flat and four QTH lamps for the UVES flat (TBC) were selected.

5.3.7 Detectors

The main detectors are two Teledyne-e2v CCD290-99, one for each of the blue and red arms. They are standard silicon, backside illuminated devices of dimension 9k $\times$ 9k pixels, that will use an antireflection coating (still to be developed) which is expected to maximize the wavelength range of the spectrograph at 300 - 405 nm. The detector control electronics will be the New Generation Controller II (NGCII) from ESO laboratories; also this is still in development. The science data on the CUBES arrays will only occupy a small percentage of the available rows (14 $\times$ 92 mm is the size of the footprint of the spectra on the detector): this is the full width of the device, but only 1400 rows vertically, located on the lower half of the detector itself. In the upper half, an amount of space is left for the AFC system, with a windowed part of the array read out at a faster frame rate than the science data. Due to the design of the subsystem, an independent control unit of the upper and lower halves of the CCDs is required, with a focus on the dark current of the detectors to maintain the performance requirement. So far, the level specified by Teledyne-e2v for the CCD290-99 arrays is 3 e-/pix/hr at 173K. The target value for CUBES is < 0.5 e-/pix/hr (to enable background-limited performance to i ≥ 20

mag, for example for high-redshift galaxies): this requires the arrays to be cooled to a lower temperature of $\leq$ 165 K. To do so, a baseline for the cryostat design was developed using a liquid nitrogen bath that is similar to others actually used at ESO. Individual baths will be fitted to each detector cryostat, with a similar layout to that used for the X-Shooter cryostats. The evacuated volume of each cryostat is nearly 3 liters, so the 1 - 10 liters standard ESO vacuum system will be used. The cryostat control electronics will control: pumping and venting, the detector thermal control, the cold finger thermal control (used for warm-up and coarse temperature control), the warm-up control, the liquid-nitrogen level monitoring,the monitoring of the cryostat states, the data logging and the alarms and safety-critical interlocks.

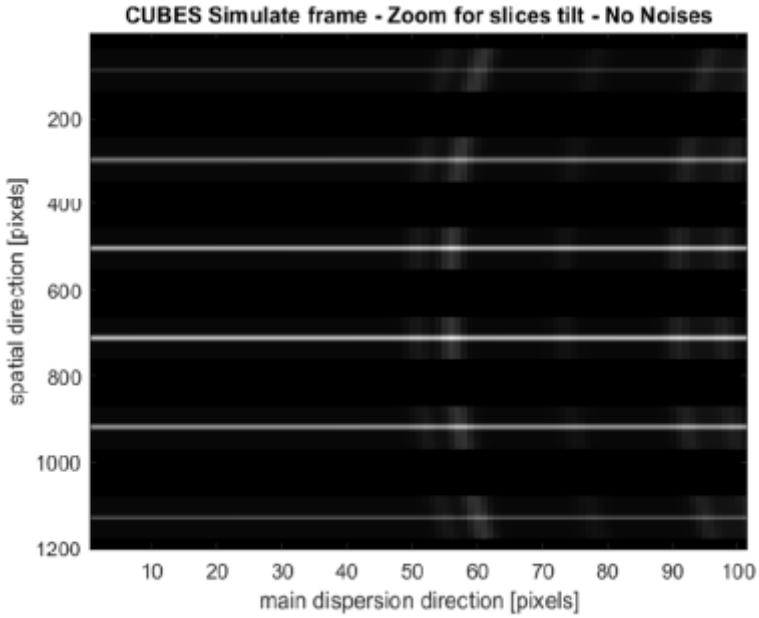

Figure 5.5: *Mock-up of the slice layout from the simulator E2E. Several sky lines are visible (with the most prominent located at 60 pixels in the main dispersion direction) over the continuum trace of the science target across the six slices. From Genoni et al. (2023).*

5.4 CUBES software

The instrument software architecture has a main workstation for the instrument and additional connected devices or components: the Controller Devices (PLC1), the archiving system, the Observation Handling Workstation (OH WS), the VLT Telescope Control System (TCS) and the fromt-end components (DWS). The Observation Blocks (fundamental scheduling units of VLT science operations) are transferred from the Observing Tool (vOT), hosted on the OH WS, to the Sequencer, which reads the information of the Observations Blocks and executes one by one the templates specified in there. Each one consists in a sequence of commands to be sent to the instrument subsystems, as OCS, FCS, DCSs and TCS (through the VLT-ELT Gateway), so they can configure the corresponding hardware according to the selected settings. The Observation Coordination Manager (OCM) coordinates

the data acquisition from the scientific detectors, triggers the creation of metadata from the other instrument subsystems and controls the data products creation. At the end of the real observation, the DCS generates the detector data and saves it in a FITS file. Then the Data Product Manager (OCM controlled) collects the CUBES data from all the subsystems and creates the final FITS file, which is then transferred to the Archiving System. The Supervisor monitors and manages the processes and states of the different subsystems. The two scientific detectors are controlled by one dedicated controller, the New General detector Controller II (NGCII) and the technical cameras of the CUBES Acquisition Guiding System and Fiber Link Guiding System are controlled by the ESO standard Camera Control Framework (CCF).

The CUBES instrument control software is based on the ELT Instrument Control Software Framework developed by ESO (to help the instrument developers implementing the control software for the ELT instruments). The IFW follows the ELT standard, and includes:

- **Function Control System (FCS):** controls and monitors the instrument hardware functions and sensors, except the detectors.
- **Detector Control System (DCS):** carries out all the tasks to control the detector subsystems.
- **Observation Coordination System (OCS):** the highest layer of the control software. It consists of a Supervisor (responsible for the overall monitoring and supervision of the subsystems), an Observation Coordination Manager (responsible for coordinating the scientific exposure) and a Data Product Manager (responsible for collecting and archiving the results of the scientific exposure in the final FITS file and for sending it to the Online Archive System).
- **Maintenance Software (MS):** used for instrument configuration and maintenance procedures.

The ELT IFW-based control system must interface with the VLT physical environment. A dedicated intermediary will be the VLT-ELT Software Gateway component, developed by ESO, which will translate protocols and interfaces between the ELT and VLT environments allowing the instrument communication with the VLT TCS. For simultaneous observations CUBES-UVES, it will also provide the synchronization between the CUBES and UVES on-line databases (OLDBs).

The Data Reduction Software (DRS) will extract complete spectra from the raw science and calibration frames produced by the instrument, removing the instrument signature. The software language will be in ANSI C, using the ESO Common Pipeline Library (CPL) and High-level Data Reduction Library (HDRL). It will be operated through the standard ESO interfaces (EsoRex, Gasgano, and ESO Reflex). An additional Python interface will be developed internally for a possible integration with the Python ecosystem standard used by the astronomical community.

5.4.1 Simulation tools

The CUBES preliminary design phase brought two main simulation softwares (Genoni et al. (2023)): an End-to-End (E2E) instrument simulator and an Exposure Time

Calculator (ETC). They have been developed to help define the current baseline design as well as in the scientific evaluation of the various observing modes. The ETC predicts the global performances of the CUBES spectrograph for a given source, considering the input instrumental parameters and the environmental conditions. It will derive the S/N per pixel for a given exposure time, and vice versa. The E2E simulator aims to simulate the instrument behavior and the astronomical observations given the flux distribution of the scientific sources/targets (or calibration sources) to the output raw-frame data produced by the CCD(s).

The End-To-End Simulator tool follows past ESO instruments simulators: it is composed of different modules (each with specific tasks), units and interfaces. The aim is to follow the same workflow as the instrument, testing the functions and limits. Three versions of the CUBES E2E have been developed for different user applications, featuring different capabilities required by the design phase:

Basic Version: aimed at science users, to assess the performance of the instrument with respect to the science objective.

Parametric Version provides fast parametric simulations of the different possible design solutions and configurations, as an aid for design development.

Full Version It produces high-level simulated frames based on a detailed physical model of the instrument (including optical effects as the contribution of blurring of the point spread function (PSF), distortions and detector diffusion effects), to be used for the development and testing of the data reduction software.

The Exposure Time Calculator(ETC) can predict the SNR for a given exposure time (and vice versa). It is a web-based application that provides the achievable SNR per pixel for a given wavelength, exposure time , sky conditions, and Vega magnitude (U, V) of a point-source target.

Different simulations with a variety of instrument working conditions were tested in 2021-2022, especially by Genoni et al., aiming for the best configuration standards. Two main configurations were selected as best options for CUBES:

- Configuration 6K: this design used 6K-15 um detectors, which were considered to minimize the spatial sampling and maximize SNR. The 1:500 aperture is sampled with six slices, resulting in a 0:2mm input slit width to the spectrograph. In this way the collimated beam size is 150mm. The minimum R is 18500, thus just below the requirement, while the average is 20500. The wavelength range provided is 305-400 nm.

- Configurations 9K: adopting a 9K-10 um detectors and reducing the aperture projected on sky allows to extend the wavelength range to 300-405 nm.

The current chosen baseline is the so-called H2, that maximizes the entrance aperture (1.5 arcsec) with R over 20000 and brings the instrument mass below the requested limit of 2500 kg.

Also low resolution mode was investigated, and two possible modes were tested:

- An input aperture of 6 arcsec and six slices, which allow an average geometrical R of 6000.

- An input aperture of 3 arcsec and four slices, which allow an average geometrical R of 8000.

Chapter 6

The project: synthetic polluted white dwarfs spectra

6.1 Previous works on the topic and the method

White dwarfs can be a laboratory for the study of terrestrial planets interiors, so far unreachable with our observations. The possibility of an element detection on the stellar surface depends on either the abundance of the element and the properties of the star: as we saw before, cold white dwarfs have a longer sinking time for heavier elements (see Chapter 4.4). Regarding the type of observations, optical and UV high-resolution spectroscopy are the first choices for this research, since elements as Ca, Si, Mg, Fe, O, C, N and S. UV spectroscopy is challenging: from the ground, up to 70% of the light is absorbed by the atmosphere when we reach below 350 nm (see Chapter 6.2.5). CUBES, as it was mentioned in Chapter 5, is expected to reach the highest efficiency below 350 nm for the U-band, considering ground telescopes, and become potentially an asset for this research field.

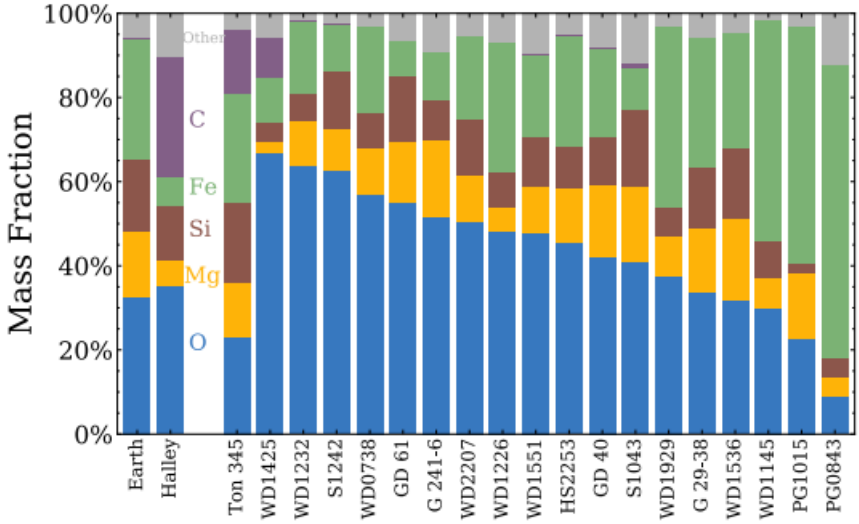

Figure 6.1: *Mass fractions of different elements (O, Mg, Si, Fe, C) from different polluted white dwarfs studies. On the left, the compositions of bulk Earth and comet Halley for comparison. From Xu & Bonsor (2021).*

Previous studies show a majority of rock-forming elements, as Mg, Ca and Fe, and volatiles as C, N and O, comparable with Earth/terrestrial bodies composition. Also, the debris is partially composed by icy particles (see Fig. 6.1): to detect ice features, due to the high temperature on stellar surface, we can trace oxygen. Formation of metal oxides as MgO, SiO_2, FeO, Fe_2O_3, and CaO requires high abundance of oxygen. Consequently, deriving the abundances of these compounds, the rest of the oxygen will be incorporated as water content.In the next paragraphs, I reported selected studies on stellar atmosphere exogeology on white dwarfs.

Zuckerman et al. (2007)

One of the first and most important observational detection of white dwarfs pollution from a planetesimal came from Zuckerman et al. (2007), with the HIRES spectrometer at Mauna Kea Observatory. Studying a heavily polluted white dwarf (GD 362, temperature 9850 K $\pm$ 100K and gravity logarithm of 9.09 $\pm$ 0.10 $cm \cdot s^{-2}$) in the wavelength range 10-20 μm, they were able to infer the abundance of 17 elements, similar to Lodders (2003) mentioned in Chapter 4.4. Most of them are heavy, metal-like elements which are not typical of interstellar space. The discovery of excess infrared emission around the star demonstrated that it is orbited by circumstellar dust particles, which confirms the accretion onto the stellar surface. The surface is helium-dominated, but rich in hydrogen and heavier elements: hydrogen is probably of interstellar source, while metals and silicates were confirmed of asteroid-like object accretion.

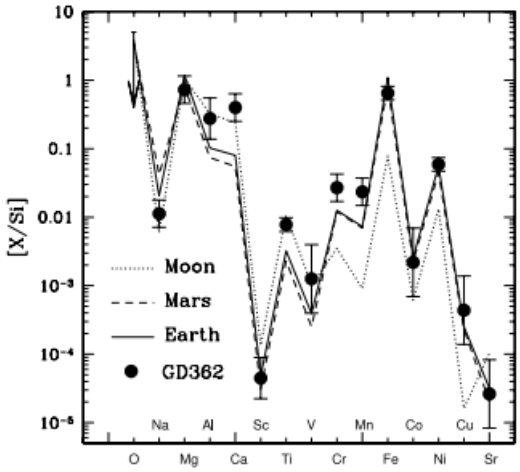

Figure 6.2: *Elemental abundances by number relative to silicon for the white dwarf GD 362 in Zuckerman et al. (2007). It is possible to see a Earth match with Mg, Sc, Co and Mn, and similar composition also respect to the Moon.*

The analysis of the abundances of sodium and calcium match with a possible Earth-Moon system, as shown in Fig. 6.2, which is strongly correlated to a planetesimal parent body and not an asteroid from the asteroid belt. Regarding the X/Si ratio, for most of the elements present in the observations it is clear that there is a strong difference with interstellar medium composition: there could be no accretion from the interstellar space. Also the possibility of comet material pollution is to be

excluded (a comet hits on average every 10'000 ys, and sinking time would be of 100'000 ys: in the study, the amount of cometary material would represent 10 comet hits; in addition, accreted icy material would have resulted in 3 times the amount of oxygen present in the star).

Gaensicke et al. (2008)

In Gänsicke et al. (2008), the first DBZ (metal-polluted) white dwarf with confirmed debris disk was discovered, SDSS J084539.17+225728. It is characterised by a T= 18'600 K ± 500K and a gas disk up to $1R_{\odot}$. The study used the Sloan Digital Sky Survey (Sloan (2000)) and retrieved 484 candidates with Ca II triplet (8498, 8542,8662 $\AA$) presence: of these, only 3 of them have the three components, and only had confirmation of a debris disk thanks to spectroscopy and photometry observations.

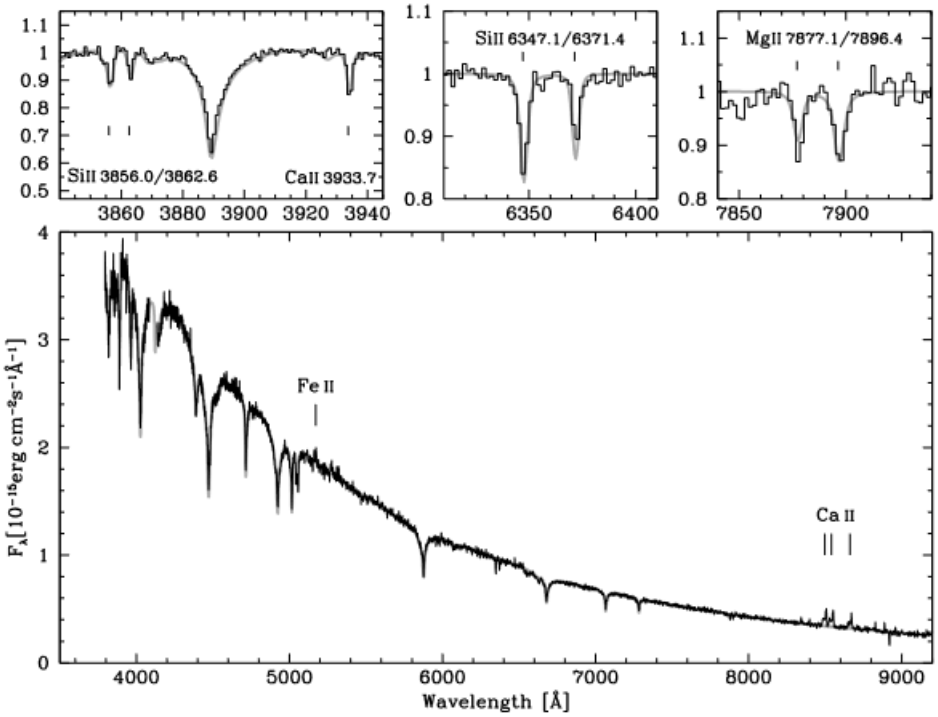

Figure 6.3: *Spectrum of SDSS J084539.17+225728 with the confirmed lines of Mg, Ca and Si highlighted. From Gänsicke et al. (2008).*

Ca, Mg and Si features were observed, as shown in the spectrum in Fig. 6.3. H alpha was not detected, and this was a sign of non-Solar abundances: probably the accretion was of a rocky asteroid. Calculating the equivalent width of the lines it was confirmed also that accretion was not of a single massive body but due to frequent episodes of small objects accretion.

Zuckerman et al (2011)

In another relevant study from Zuckerman et al. (2011), two heavily polluted white dwarfs were analysed : G149-28 and NLTT 43806, both aluminium-rich. Using the

HIRES spectrometer, the two stars were observed in the range 3130-5940 $\dot{A}$. G149-28 has an average effective temperature of 8600 K with gravity logarithm of 8.10 $cm \cdot s^{-}2$, NLTT 43806 of 5900 K (one of the coldest polluted white dwarfs) and 8 $cm \cdot s^{-2}$. Both stars have a very high accretion rate , around $10^{8} g \cdot s^{-1}$, and they are confirmed to be in a declining phase of accretion (otherwise it would be impossible to observe within the sinking time any element on the surface).

Table 6. Element Abundances by Number in NLTT 43806, G149-28, and the Solar System

Z/Al	NLTT 43806 photosphere	NLTT 43806 steady state accretion	G149-28 photosphere	Solar	Bulk Earth	Earth's continental crust	30% crust 70% upper mantle (by weight)	lunar mare basalt	CI	Euc	How
Ca/Al	0.5	0.61	1.35	0.76	0.72	0.425	0.57	1	0.73	0.76	0.70
Mg/Al	3.16	2.82	8.5	12.3	11.8	0.428	3.11	0.77	12.6	0.74	1.54
Fe/Al	0.63	1.07	5.75	10.2	9.1	0.405	0.61	1.31	10.5	1.10	1.26
Si/Al	2.5	2.68	<9.3	12.0	11.0	3.07	4.48	3.65	12.0	3.3	4.1
Na/Al	0.32	0.27	<4.7	0.69	0.19	0.32	0.26	0.043	0.69	0.038	0.052
Ti/Al	0.011	0.0166	0.05	0.029	0.0265	0.036	0.0343	0.236	0.029	0.037	0.031
Cr/Al	0.011	0.0178	<1	0.155	0.148	0.001	0.0147		0.158	0.019	
Ni/Al	0.032	0.0575	0.69	0.57	0.49	0.00057	0.0105		0.575		

Figure 6.4: *Element to aluminium ratios for both WDs from this work compared to Solar, Earth's bulk, Earth's continental crust, Earth's core/crust mix, Moon composition and chondrites/eucrites. From Zuckerman et al. (2011).*

Both stars are characterised by an high amount of aluminium. G149-28 has a composition similar to Earth's bulk and meteorites (chondrites); it may have originated from a parent body similar to Earth. On the opposite, NLTT 43806 is unusual: very iron poor but aluminium rich, typical of high temperature rocky material. At the same time, even if Al is common in Earth's crust, there is no match with other elements (see ratios in Fig. 6.4). A good match was achieved with a simulation of 30% Earth crust and 70% mantle material, maybe due to accretion of debris from an impact of a differentiated planet with a huge rocky object (as an asteroid), which would have freed part of the mantle material.

Xu et al. (2014)

On HIRES data, Xu et al. (2014) studied two pulsating white dwarfs, G29-38 and GD 133, in the optical, infrared and ultraviolet bands. G29-38 has an effective temperature of 11'820 K $\pm$ 100K and gravity logarithm of 8.40 $cm \cdot s^{-2} \pm$ 0.10 $cm \cdot s^{-2}$ and GD 133 12600 K $\pm$ 200 K and 8.10 $cm \cdot s^{-2} \pm$ 0.10 $cm \cdot s^{-2}$. Main lines observed for both stars were from C, Mg, O, Si, Ca, Ti, Cr and Fe. Less intense lines from N, S and Ni were also detected. The sinking times for the elements are short compared to disk life: both stars appear to be in steady accretion phase.

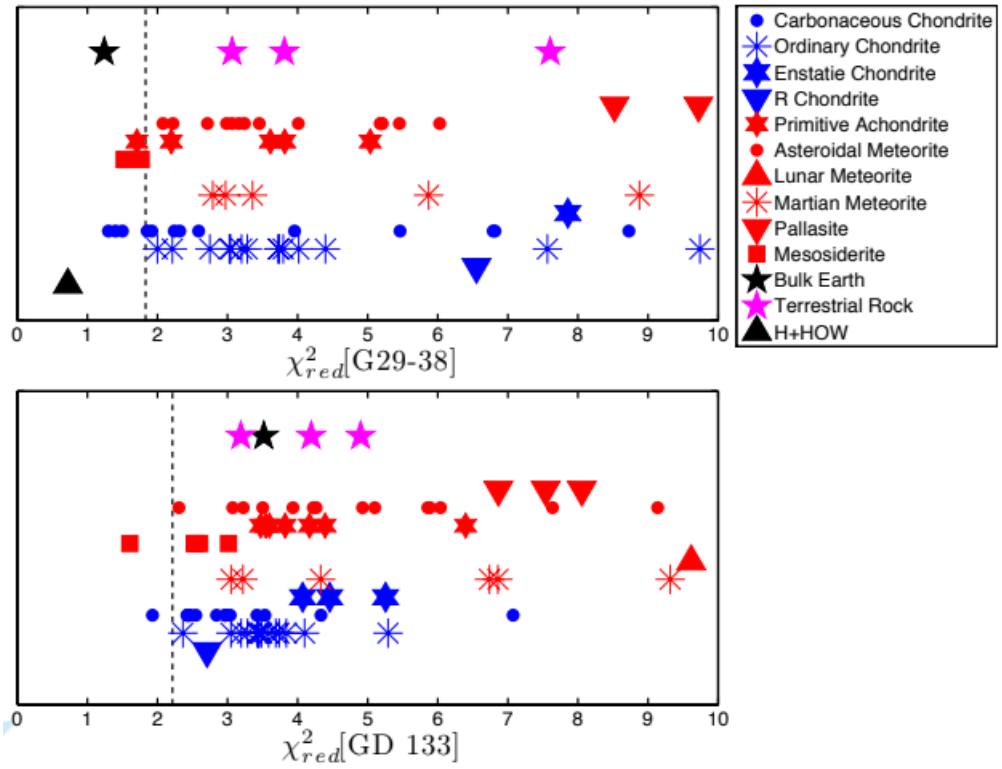

Figure 6.5: *Computed reduced chi-squared values between the observed composition and meteorites, with upper panel for G29-38 and lower panel for GD 133. For G29-38, it is compared the mass fraction of 10 elements (C, O, Mg, Si, S, Ca, Ti, Cr, Fe and Ni) relative to the summed mass of O, Mg, Si and Fe; for GD 133, 5 elements (C, O, Mg, Si and Ca) are considered relative to the summed mass of O, Mg and Si. The dashed lines represent 95% confidence level. The black triangle represents one of the blends that can best match the abundances observed in G29-38 (60% H chondrite and 40% of howardite, an chondritic stony meteorite). From Xu et al. (2014).*

For both of them, the main reason behind the presence of such heavy elements is accretion of a rocky planetesimal. In the case of G29-38, the dominant minerals found were amorphous carbon and amorphous/crystalline silicates (silicates ($MgFeSiO_4$, Fe_2SiO_4, $Fe_2Si_2O_6$, $CaMgSi_2O_6$, $Mg_2Si_2O_6$), water ice (H_2O) and metal sulfides. A comparison with the Earth bulk components and different types of meteorites components, as achondrites (stony meteorite that does not contain chondrules, or round grains; it consists of material similar to terrestrial basalts and has been differentiated and reprocessed to a new degree due to melting and recrystallization), mesosiderites (stony–iron meteorites consisting of about equal parts of metallic nickel-iron and silicate) and chondrites is shown in Fig. 6.5 . The star appears to be abundant in calcium and titanium, which can be referred to a refractory elements-rich parent body, probably at beginning of geological differentiation. For GD 133, a similar comparison was made and the results were a high abundance in mesosiderites and low in carbon, but the overall accretion rate was low and not comparable with the information it was possible to retrieve from G29-38.

Gaensicke et al. (2012)

With the Hubble Space Telescope, Gänsicke et al. (2012) researched four different white dwarfs: PG 0843+516, PG 1015+161, SDSS 1228+1040, and GALEX 1931+0117; their parameter are visible in Fig. 6.6. The survey was conducted in far ultraviolet band (1000-1500 $\dot{A}$), with additional observations in the optical band to detect calcium and magnesium strong lines (the Ca II H/K doublet and the Mg II 4482 $\dot{A}$ line). Main elements detected were C,O,Mg,Al,Si,P,Ca,Cr,Mn,Fe and Ni, where C, O and Fe were always found in all the four cases in different observations.

Object	$T_{\rm eff}$ (K)	log g (cgs units)
PG 0843+516 = WD 0843+516		
Optical (Liebert et al. 2005)	23 870 ± 392	7.90 ± 0.05
HST (this paper)	23 095 ± 230	8.17 ± 0.06
PG 1015+161 = WD 1015+161		
Pptical (Liebert et al. 2005)	19 540 ± 305	8.04 ± 0.05
Optical (Koester et al. 2009)	19 948 ± 33	7.925 ± 0.006
HST (this paper)	19 200 ± 180	8.22 ± 0.06
SDSS J122859.93+104032.9 = WD1226+110		
Optical (Eisenstein et al. 2006)	22 125 ± 136	8.22 ± 0.02
Optical (Gänsicke et al. 2007)	22 292 ± 296	8.29 ± 0.05
Optical, our fit to SDSS spectrum	22 410 ± 175	8.12 ± 0.02
HST (this paper)	20 565 ± 82	8.19 ± 0.03
Adopted (this paper, Section 3.1)	20900 ± 900	8.15 ± 0.04
GALEX J193156.8+011745 = WD 1929+012		
Optical (Vennes et al. 2010)	20 890 ± 120	7.90 ± 0.03
Optical (Melis et al. 2011)	23 470 ± 300	7.99 ± 0.05
HST (this paper)	21 200 ± 50	7.91 ± 0.02

Figure 6.6: *White dwarfs stellar parameters in Gänsicke et al. (2012).*

Through a comparison with Earth's bulk, core and silicate rocky planets composition, it was possible to understand that most of the parent body material was of rocky nature. There is significant difference among the white dwarfs selected for the study: 1) SDSS 1228+1040 has composition similar to bulk Earth; 2) PG 1015+161 is silicate depleted respect to Earth's bulk; 3) PG 0843+516 is abundant in Fe, Ni and S, typical of Earth's core, with Cr (usually present due to a partitioning process into the Earth's core), all signs of geological differentiation. In general, there is the prevalence of minerals composed of iron and magnesium jointed with silicon. No carbon-oxygen based minerals were found, but the Al/Ca ratio follows a similar trend as observed among Solar system (see Fig. 6.7), which suggests that processing of proto and post-planetary material follows similar underlying principles.

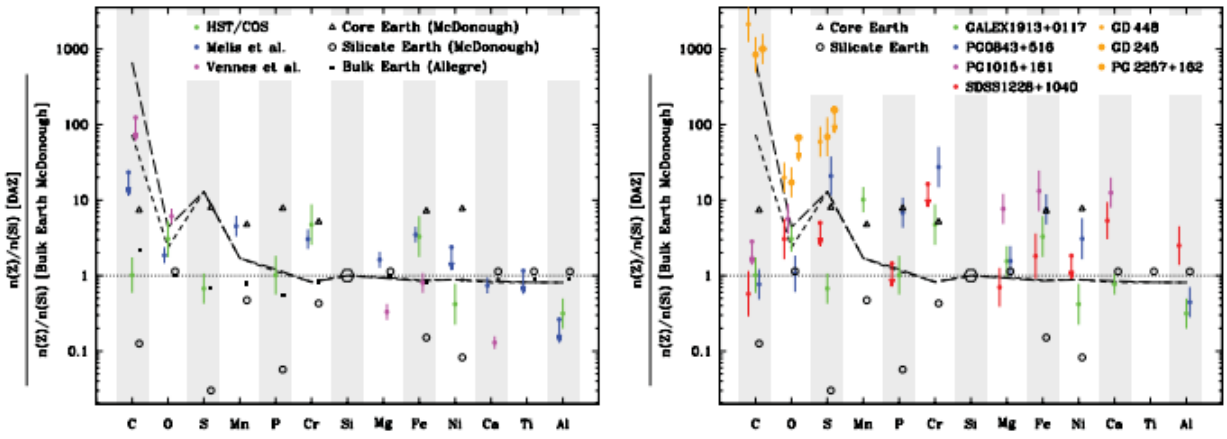

Figure 6.7: *The chemical abundances of original planetary debris of the studied polluted white dwarfs: the four panels illustrate a range of metal-to-Si number abundance ratios compared to those of bulk Earth and bulk silicate Earth (BE and BSE; McDonough (2001)), solar abundances and CI chondrites (S and CI; Lodders (2003)), and several meteorite classes (grey =carbonaceous chondrites, green = mesoderites, blue = pallasites, red = diogenites, orange = howardites, magenta = eucrites; from Nittler et al. (2004)). In light blue, are the abundance ratios for the polluted DB white dwarfs GD 362 (Zuckerman et al. (2007)), GD 40 (Jura et al. (2012)) and HS 2253+8023 (Klein et al. (2011)). Plot from Gänsicke et al. (2012).*

Venderburg et al 2015

An interesting study from Vanderburg et al. (2015) analyzed a He-dominated white dwarf (WD 1145+017) with temperature of 15'900K ±500 K . It was identified a transit period of 4.5 hours up to 5 hours, and, at the same time, spectroscopy on the star revealed the presence of magnesium, silicon, calcium, iron and nickel on the surface (accreted in the last 10^5 yr). Simulations revealed the possible presence of six bodies partially or completely disintegrated by the star, which have formed dusty clouds around the star itself (this explains also the asymmetric transit shadow). The planetesimals are supposed to be rocky ($\rho > 2g \cdot cm^{-3}$), with a very short period compared to the star (within the tidal radius).

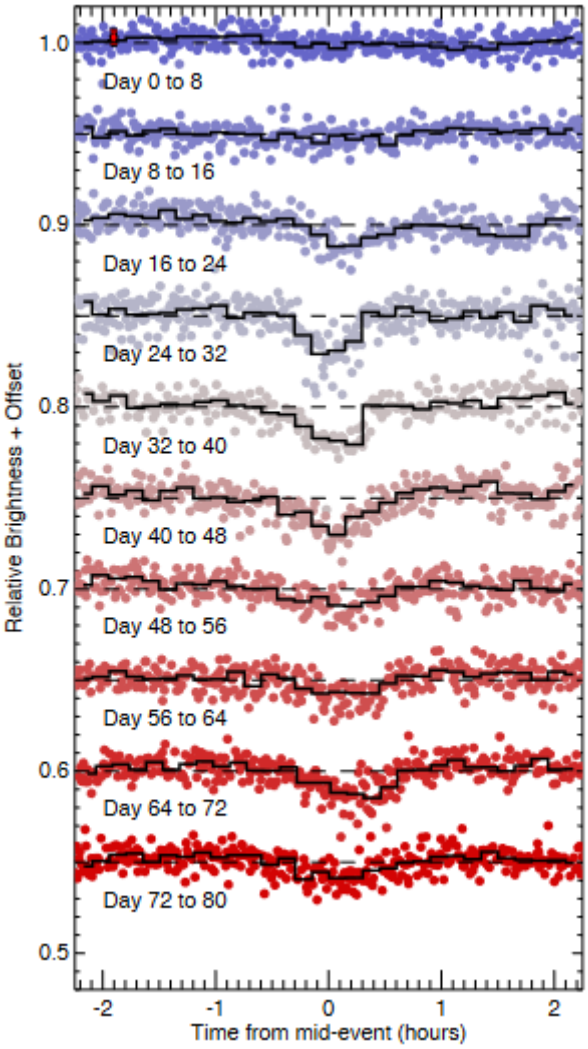

Figure 6.8: *The WD's light curve broken into segments 8 days in length and folded on the most significant, 4.5 hour period. The individual data points (sampled with a 30 minute integration time) are shown as dots, with the colour representing the segment in time. The averaged light curve for each bin is shown as a solid black line. The typical measurement uncertainty (standard deviation) is shown with a red error bar on one data point in the upper left. From Vanderburg et al. (2015).*

Even if not certain, this case is a striking example of the asteroid/planetesimal accretion in polluted white dwarfs. The light curves and the transit are shown in Fig. 6.8.

6.1.1 Selection of elements from known polluted white dwarfs

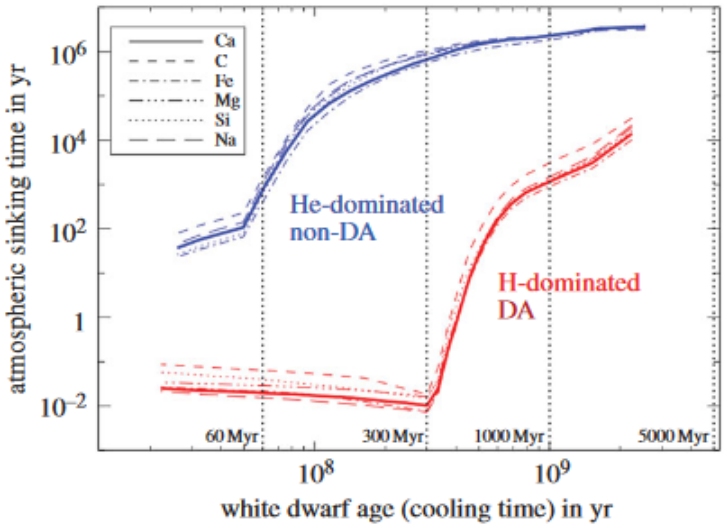

Figure 6.9: *Sinking times of different elements (Ca, C, Fe, Mg, Si, Na) respect to cooling age for DA H and He white dwarfs. It is clear that He WDs have longer sinking times for shorter cooling ages. From Veras (2016).*

So far, less than fifty white dwarfs with low temperature and long sinking times which show a heavy polluted atmosphere were detailed spectroscopically analysed (Gänsicke et al. (2012)). On their surface, a variety of absorption atomic lines were detected (most common elements were O, Na, Mg, Al, Si, P, S, Ca, Sc, Ti, V, Cr, Mn, Co, Ni, Cu, Sr, with atomic numbers up to 38; so far a total of 18 heavy elements was found). Analysing previous publications and the related lines detected on white dwarfs, a new selection of possible elements to survey was prepared.

Comparing the results from white dwarfs observations and bulk Earth/asteroids composition, we notice that most of the rocky planetary material is similar in composition to bulk Earth (Bonsor & Xu (2017). The bulk Earth composition was determined in models through meteorites studies and it is dominated by four elements, O, Mg, Si and Fe, as it is visible in Fig. 6.10. The low oxygen abundance suggests the accreting material has little H_2O, which means low to none water content (this excludes icy cometary material). In addition, the carbon C, present in the Halley Comet, is nearly non-existent in the studied white dwarfs, as in the Earth's bulk. If oxygen was higher, it would have been connected to observed elements that form typical rocky minerals(MgO, SiO_2, FeO, etc..). It is also possible to study differentiation in exoplanets geological structure: for example, the Ba-to-Ca ratio is a determinant factor for plate tectonics activity. Traces of elements typical of rocky material undergoing important pressure and temperature conditions were found in multiple polluted white dwarf, and the Fe-to-Al ratios measured in this kind of stars

is much larger than the ratios measured in CI chondrites and planet-hosting stars.

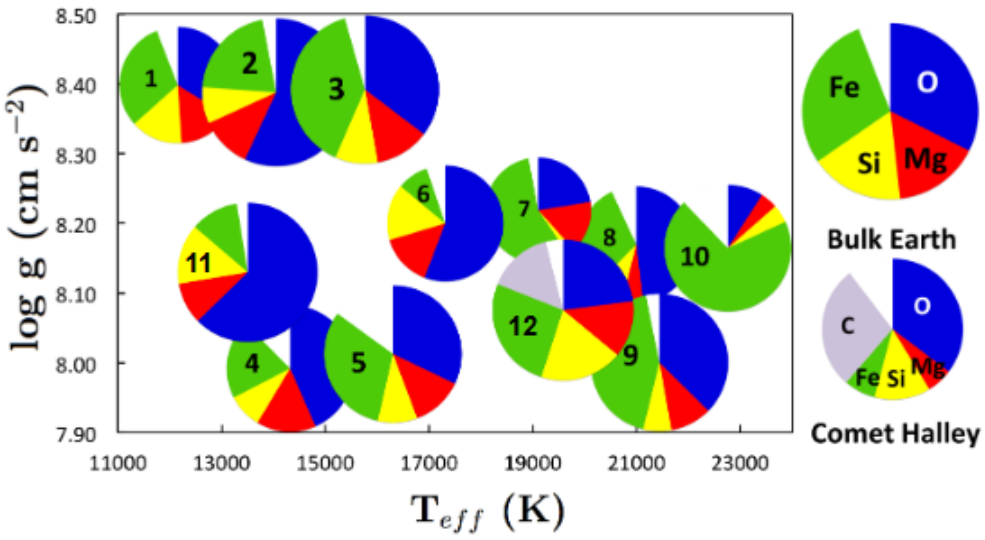

Figure 6.10: *Set of 12 white dwarfs with lines of O, Mg, Si and Fe, and a comparison with Earth bulk and Hally Comet. The abscissa represents the effective temperature of the white dwarf (cooling age) and the ordinate is surface gravity (main sequence mass). Most white dwarfs have accreted extrasolar planetesimals with compositions similar to bulk Eart. From Bonsor & Xu (2017).*

Polluted white dwarfs are DZ white dwarfs, or white dwarfs with metals lines on their surface (with little or no convection found). The total amount of the known DZ stars are above 80'000: to further select the targets, we researched only white dwarfs confirmed as polluted by planetesimals accretion in previous studies. The main parameters for pollution confirmation through planetesimals were (Veras (2016)):

1. presence of debris disk confirmed;
2. signs of planetesimal accretion;
3. Earth/planet-like elements' signatures on surface of the star;
4. Solar system similar abundances on stellar surface;
5. important difference with interstellar medium abundances;
6.

The fraction of polluted WD systems is 25– 50% and hence roughly commensurate with estimates of Milky Way MS planet-hosting systems (since the sinking times are orders of magnitude shorter than the WD cooling age, we should always expect to detect heavy metal pollution at a level under 0.1%; see Fig. 6.9). Our main goal is testing CUBES on the same astrophysical event: it is good to have a comparison and see either the limitations and improvements it is possible to obtain. Collecting the white dwarfs that appear through 10-12 previous researches, it was possible to make a list of the stars with the different stellar parameters:

OBJECT	V magnitude	Spectral class	Radius($R0$)	Mass (M_0)	Surface gravity (log g)	Age(ys)	Temperature(K)	Publication
GD 40	11.3	DB	0.1	0.59	7.90	$2 \cdot 10^8$	15'300	Jura et al. (2012)
GD 61	13.8	DBAZ		0.7		$6 \cdot 10^8$	17'800	Jura et al. (2012)
PG 0843+516	11.4	DA			7.90		23'100	Gänsicke et al. (2012)
PG 1015+161	15.6	DA			8.04		18'540	Gänsicke et al. (2012)
PG 1225-079	14.8	DB		0.58	8.00		10'800	Xu et al. (2013)
GD 362	16.23	DB		0.72	8.24		10'540	Xu et al. (2013)
NLTT 43806	15.4	DA			8.00		5'900	Zuckerman et al. (2011)
WD 1929+012	14.2	DA			7.90		21'200	Gänsicke et al. (2012)
HS 2253+8023	16.11	DB		0.84	8.4		14'400	Klein et al. (2011)
G29-38	13	DA		0.85	8.40		11'800	Xu et al. (2013)

Table 6.1: *In the table the characteristics of all the polluted WDs selected in our work (information from the relative publication and Wenger (2000)).*

To select the lines we wanted to analyze, we focused on previous research. For each target observed spectroscopically, we searched for the lines highlighted in the publication and then compare the results with other studies and polluted white dwarfs. The final selection is below:

OBJECT	CI	CII	CIII	NI	OI	Na	NaI	MgI	MgII	Al	AlII	AlIII	SiI	SiII	SiIII	PII	PIII	SII
GD 40																		
GD 61																		
PG 0843+516																		
PG 1015+161																		
PG 1225-079																		
NLTT 43806																		
GD 362																		
WD 1929+012																		
HS 2253+8023																		
G29-38																		

	CaI	CaII	ScII	TiI	TiII	VII	CrII	CrII	MnII	FeI	FeII	CoI	NiI	NiII	CuII
GD 40															
GD 61															
PG 0843+516															
PG 1015+161															
PG 1225-079															
NLTT 43806															
GD 362															
WD 1929+012															
HS 2253+8023															
G29-38															

Figure 6.11: *In the table, we selected some examples of polluted white dwarfs from the previous works presented above, and for each of them we highlighted the absorption lines observed to see the most common element (in green the lines observed on the target).*

The source for the precise wavelengths and the intensity is the NIST database (National Institute of Standards- NIST (2013)) for atomic lines. The catalogue is a selection of the most important and frequently used spectroscopic data. It is possible to choose either neutral and singly-ionized atoms of all elements, from hydrogen to einsteinium (Z = 1-99). It will report wavelengths, intensities, and spectrum in different format for each line. The data comes both from published and unpublished material, and also incomplete information about certain elements are still reported.

Using the NIST database, for each of the elements in Fig. 6.11 a list of the strongest lines in the spectra of the neutral and singly-ionized atoms was researched, obtaining the wavelength, the ionization stage, the reference for the wavelength measurement, and an intensity. Regarding the wavelength value, it is derived from Reader (2000), with a stated uncertainty of less than 0.001 $\dot{A}$. The intensities are not obtained with direct calculation: the relative intensities of the spectral lines observed for any element depend upon the light source and excitation conditions. The database assigns an intensity of 1000 to the strongest line/lines for element, while the relative intensities are based on values from Reader (2000).

INTENSITY	WAVELENGTH(Å)	LINE	INTENSITY	WAVELENGTH(Å)	LINE	INTENSITY	WAVELENGTH(Å)	LINE
1000	3093.102	V II	500	3330.775	Mn II	90	2933.054	Mn II
1000	3135.48	Na II	400	3586.557	Al II	90	2972.29	O I
1000	3273.96	Cu I	400	3900.675	Al II	90	3015.367	Sc I
1000	3349.405	Ti II	400	3920.693	C II	90	3072.986	Ti II
1000	3414.764	Ni I	400	3134.72	O II	90	3072.986	Ti II
1000	3453.51	Co I	400	3911.957	O II	90	3119.723	Ti I
1000	3578.682	Cr I	400	3973.2562	O II	90	3119.723	Ti I
1000	3613.831	Sc II	400	3183.992	V I	90	3217.073	Ti II
1000	3736.901	FeI	300	3331.875	Ni II	90	3217.073	Ti II
1000	3856.017	Si II	250	3036.1	Cu I	90	3340.341	Ti II
1000	3911.812	Sc I	250	3063.41	Cu I	90	3340.341	Ti II
1000	3933.6614	Ca II	250	3307.95	Cu I	90	3394.578	Ti II
1000	3961.52	Al I	200	3888.6456	He I	90	3394.578	Ti II
900	3653.495	Ti I	200	3905.523	Si I	90	3783.53	Ni I
900	3653.495	Ti I	140	3368.936	Sc II	90	3783.53	Ni I
700	3686.555	Cu II	120	2939.308	Mn II	90	3794.962	V I
600	3234.513	Ti II	100	3856.017	Si II	90	3807.144	Ni I
600	3361.227	Ti II				90	3807.144	Ni I
600	3234.513	Ti II				90	3919.165	Cr I
600	3361.227	Ti II				90	3963.694	Cr I
600	2802.7056	Mg II						
INTENSITY	WAVELENGTH(Å)	LINE	INTENSITY	WAVELENGTH(Å)	LINE			
80	2905.692	Si II	9	3209.19	Cr II			
80	2970.0994	Fe I	9	3358.49	Cr II			
80	3000.9478	Fe I	9	3403.3	Cr II			
80	3037.3887	Fe I	9	3815.438	Cr I			
80	3047.6045	Fe I	9	3819.57	Cr I			
80	3193.2998	Fe I	9	2905.477	Cr I			
80	3297.6	Ni II	8	3970.072	H			
80	3297.6	Ni II	8	3336.394	Mn II			
80	3570.2542	Fe I	8	3497.525	Mn II			
80	3838.292	Mg I	8	3302.98	Na I			
80	3841.0481	Fe I	7	3339.81	Cr II			
80	3895.6565	Fe I	7	2900.154	Mn II			
70	3359.668	Sc II	4	3092.984	Mg I			
60	3888.6046	He I	4	3092.984	Mg I			
50	3057.144	Al I	3	3613.64	He I			
40	3050.073	Al I	3	3705	He I			
15	2797.998	Mg II						
15	3203.1	He II						
15	3302.37	Na I						

Figure 6.12: *In the table, the 81 lines selected for the synthetic spectra, with wavelength, relative intensity and element from NIST.*

The injection of the lines in Fig. 6.12 in the simulated spectra was done in small steps, from very strong lines (1000) to the weakest ones (1-10). A total of five classes

was prepared, base on the intensity in the database: 1) 1000 2) 600-900 3)100-500 4) 11-100 5) 1-10. As expected, most of the lines in the category 1 and 2 were found also in previous works on the same topic.

6.2 Synthetic spectra

6.2.1 Selection of non-polluted WDs catalogues

The method for simulating the spectra obtained in this work was based on lines injection on a non-polluted white dwarf's continuum spectrum (blackbody shape). After selecting the elements and the related absorption lines, a catalogue of white dwarfs spectra was required: it was decided to use only pure hydrogen atmosphere (without any pollution due to the lines injection subsequent step) with a small range of temperatures (1000 K range). We chose very cool stars to have hypothetically the longest sinking time possible: it is clear in reality only around 200 white dwarfs in DZ spectral class have such low effective temperature. In addition, the spectra we used have a wide range of gravity values from 6.5 to 9.0 $cm \cdot s^{-2}$.

Koester 2010

The first catalogue is from Koester (2010), with a total of 1066 spectra in the database. The stellar parameters have been obtained through the calculation and subsequent comparison with real data of the intensity of radiation at surface level:

$$\bar{I} = 2 \int_0^{\frac{\pi}{2}} I(\vartheta) cos(\vartheta) sin(\vartheta) d\vartheta \tag{6.1}$$

where ϑ is the angle of emission relative to the normal on the surface. To do so, an atmospheric model was selected for the simulation. The assumptions were:

- Homogeneous parallel layers (quantities depend on height only).
- Hydrostatic equilibrium (see Chapter 2).
- Radiative and convective equilibrium (the energy is conserved and only transported within the atmosphere).
- LTE(Local Thermodynamical Equilibrium: a condition under which matter emits radiation based on its intrinsic properties and its temperature, uninfluenced by the magnitude of any incident radiation; it occurs when the radiant energy absorbed by a molecule is distributed across other molecules by collisions before it is reradiated by emission).

The major code is divided in two parts: 1) physical structure of the outer layers (pressure, temperature, density, absorption coefficients) 2) surface intensity with the emergent spectrum. Regarding the absorption coefficients, the processes involved considered in this work are: bound-free and free-free absorption of neutral hydrogen, bound-free and free-free absorption of the H ion, bound-free and free-free transitions of the H+2 ion, bound-free absorption of neutral helium, free-free absorption of

He-, bound-free and free-free absorption of the negative carbon ion C-, bound-free transitions for heavier elements, Thomson scattering by free electrons, Rayleigh scattering by HI/ HeI/H2, molecular absorption and spectral line absorption. To derive the final intensity, the radiative transfer equation is used:

$$\mu \frac{dI}{\rho \kappa dz} = I - S \tag{6.2}$$

where ρ is the density, κ is the absorption coefficient, I (depending on an emission coefficient ε) is the emitted intensity and S is the source function (ratio between emission and absorption coefficient). The solution is only numerical and obtained with two constraints:

$$I_{top} = 0$$

$$\mu < 0$$

(6.3)

Convection was constrained only with three parameters (a,b,c) present in the solutions. But so far, we have not a consistent theory for white dwarfs convection, due to the high turbulence in atmosphere.

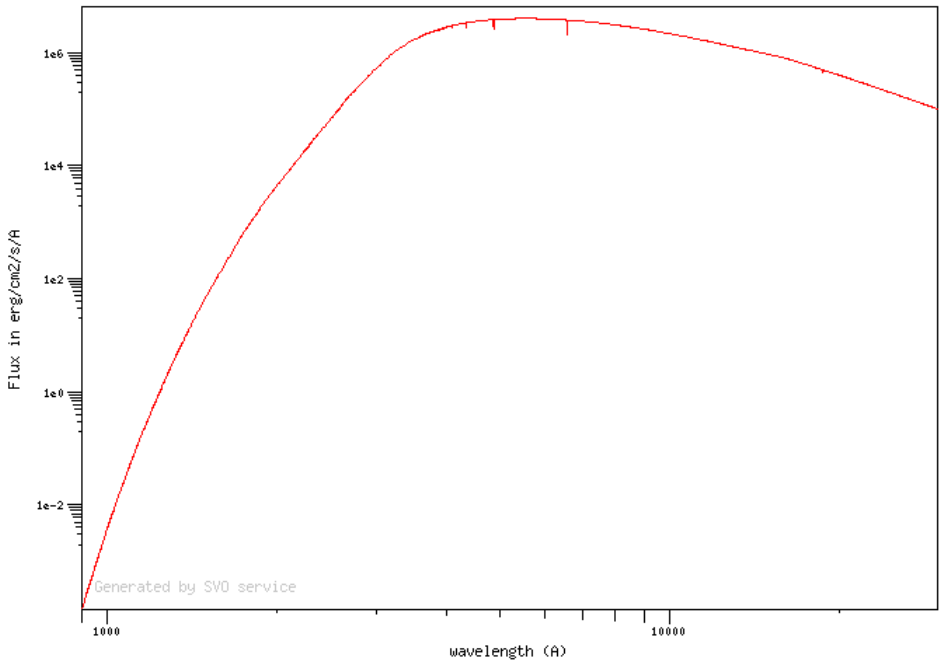

Figure 6.13: *An example from the catalogue Koester 2010, with T=5'000K, log(g)= 6.5* $g \cdot cm^{-2}$.

Levenhagen 2017

The second catalogue selected was from Levenhagen et al. (2017). It is characterised by an overall higher temperature range (17'000-100'000 K), for a total of 2183 synthetic spectra. It was decided to use a range of samples from 17'000K to 18'000K, to reduce the settling times of elements typical of hotter stars. The main assumptions are the same as for Koester, with the addition of NLTE spectra (Non-Local Thermodynamical Equlilibrium) for stars with T >34'000 K (not selected for this project). These white dwarfs include some strong absorption lines of hydrogen, as it is visible in Fig. 6.14. The synthetic spectra are prepared though the SYNSPEC code (Zboril (1996)) and the atmosphere modelling comes from TLUSTY (Hubeny & Lanz (2017)). The main difference with the Koester catalogue is the finer sampling of the model (up to $4e^5$ data points per spectrum).

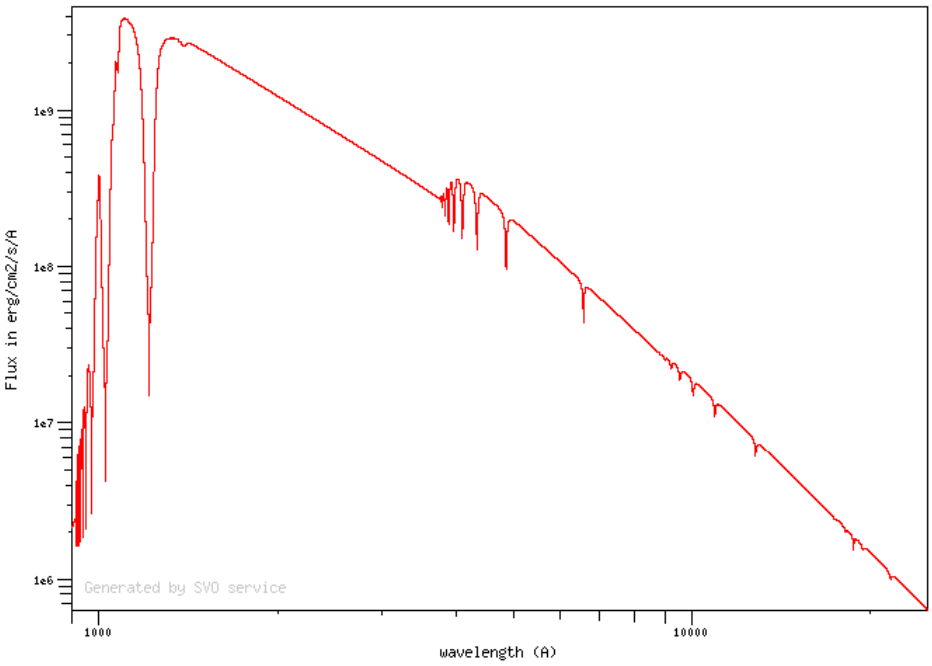

Figure 6.14: *An example from the catalogue Levenhagen 2017, with T=17'000 K, log(g)= 7.0* $g \cdot cm^{-2}$.

6.2.2 Continuum fitting and re-sampling

The first step in the generation of synthetic spectra was to obtain the continuum black body function for the different white dwarfs samples from our catalogues. To do so, it is necessary to first reduce the wavelength range within 3000-4000 $\dot{A}$ for both catalogues. They cover around 100-10'000 $\dot{A}$, but CUBES works efficiently in a smaller range, which we are testing.

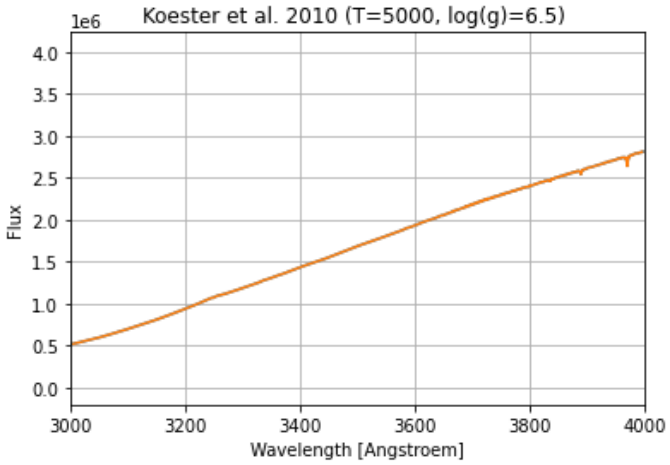

a)

Figure 6.15: Koester 2010

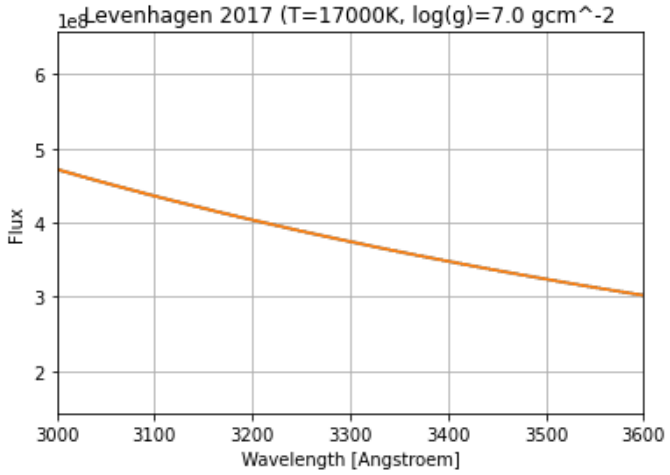

b)

Figure 6.16: Levenhagen 2017

Figure 6.17: *Fit functions for Koester catalogue sample (Fig. a) and Levehagen catalogue sample (Fig. b). It is fitted only the range 3000- 4000 Å for Koester and 3000-3600 Å for Levenhagen, due to the presence of strong lines at λ 3600Å): it is the range used for our work.*

To fit the continuum of the spectra, we used a function to fit with a black-body shape:

$$B = \frac{2hc^2}{\lambda^5 e^{(\frac{hc}{\lambda KT})}} \tag{6.4}$$

and with a piece wise cubic polynomial which is twice continuously differentiable, through CubicSpline from scipy.interpolate package (scipy (2023a)). In addition, we re-sampled the wavelengths of the spectra using the wavelength grid of the instrument, which has a sampling of 2.4 pixel per wavelength. At the end of this process, we saved the continuum fit and normalised spectra for the next step (examples visible in Fig 6.17).

6.2.3 Lines injection

The lines selection is presented in Fig. 6.12. To inject them in our samples, I generated a Gaussian-shaped function for each line:

$$f = \frac{A}{\sqrt{2\pi}\sigma} e^{(\frac{-1}{2}\frac{(\lambda-\mu)^2}{\sigma^2})} \tag{6.5}$$

where μ is the mean wavelength of the peak, A a multiplicative parameter for amplitude and σ_{line} is the distribution's standard deviation.The σ_{line} is then a straightforward representation of the line's profile width, and in the text it will be considered the line's width main parameter. As we have seen in Fig. 6.18, the width of the line is taken at $(-\sigma, \sigma)$, which in our case are substituted by the given parameter σ_{line}.

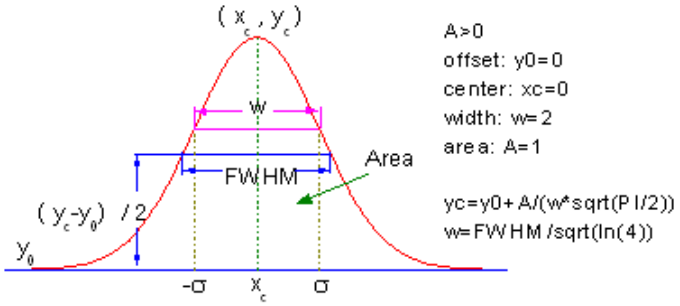

Figure 6.18: *Gaussian function parameters from OriginLab (2023). W is the line's profile width, which is represented by $(-\sigma, \sigma)$. It differs from the equivalent width, which is the area under the line profile respect to the continuum.*

For each wavelength, a specific function was created, with two free parameters: line intensity and line profile's width. I decided to create different classes again to test the limit for intensity and equivalent width. A scheme of the synthetic spectra creation process is shown in Fig. 6.19.
First, five different sets of lines could be injected. Second, for each lines group it is now possible to select four different line profile's width (which is defined by σ_{line} in the Gaussian function). Last, it is possible to choose from 0.1 to 1.0 intensity (which is the amplitude A in the function).

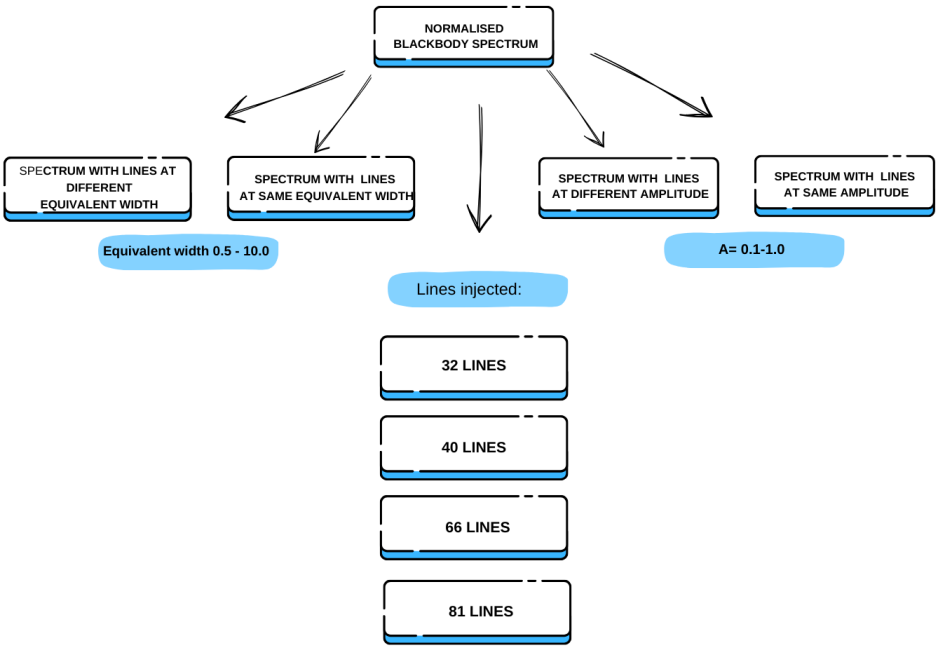

Figure 6.19: *Schematic process of synthetic spectra creation based on the parameters of 1) number of lines 2) amplitude of the lines 3) equivalent width of the lines.*

As it is clear, the possible outcomes are multiple. Lines were directly injected with a multiplication respect to the original y-axis value of the flux: in this way, we noticed that the function was actually using the original data from the spectra and not creating new flux values. In Fig. 6.20, different synthetic spectra with injected lines are shown. In total, with 50 spectra with only continuum blackbody shape for each catalogue, we obtained a sample of 2800 spectra with different properties.

6.2.4 Noise

This paragraph is divided in two main sections, the potential noise sources for ground telescopes and the method used to add a synthetic random noise to our spectra.

Noise sources

The noise treatment is based on Richmond (2023) and Hainaut (2005). The signal flux is based on the target we are observing, and it is the only source of light. However, the noise has four main standard sources: the star's shot noise, the sky background shot noise, the detector (CCDs) thermal noise and readout noise.

Star's shot noise The star produces photons described by a Poisson distribution, with random variations called shot noise. To quantify the size of the noise we use the formula:

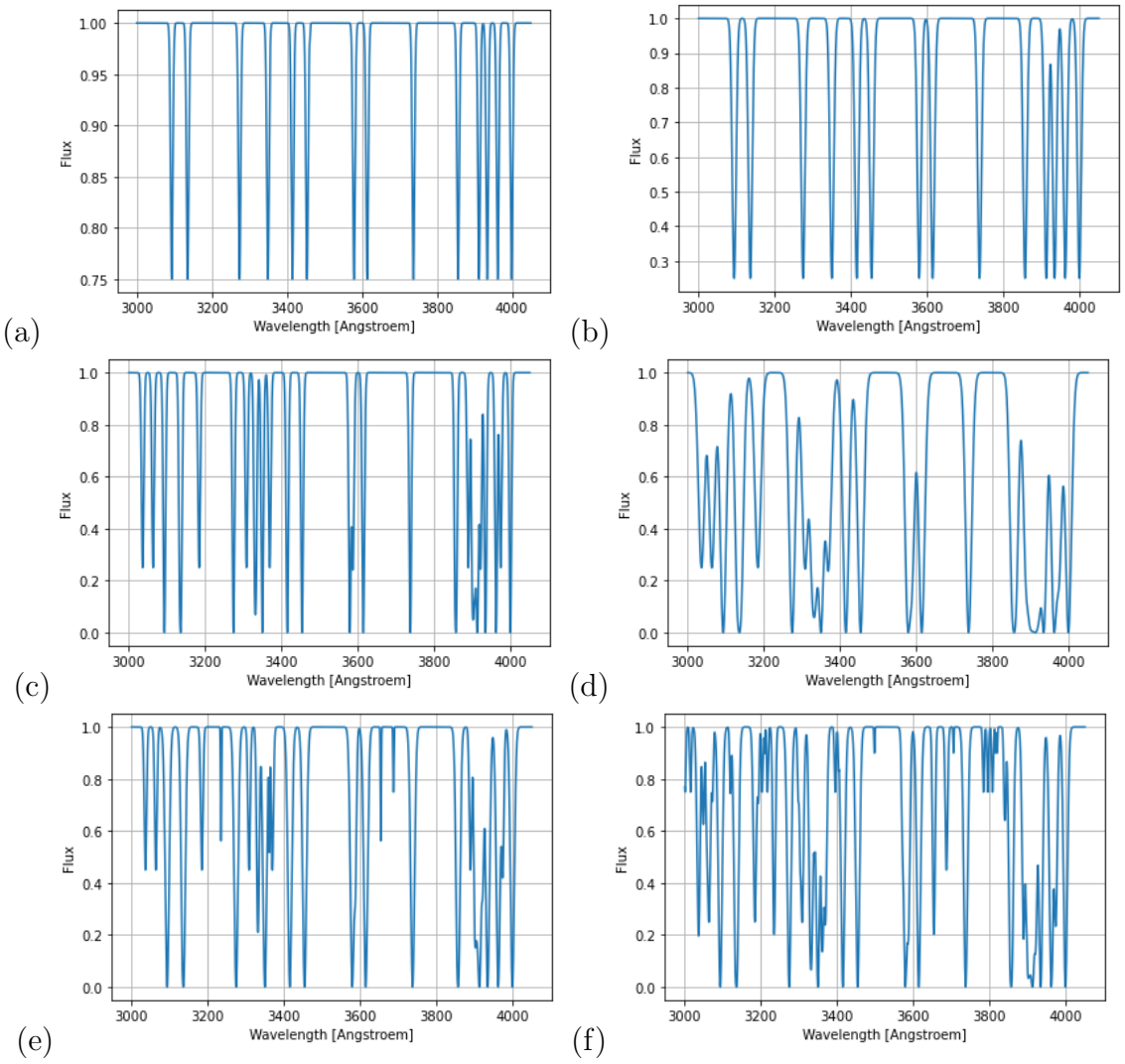

Figure 6.20: *Examples of spectra with injected lines (only Koester catalogue). (a) Lines of all five classes, all same amplitude (A= 0.25) and with a sigma of 3.0. (b)Lines of all five classes, all same amplitude (A= 0.75) and with a sigma of 5.0. (c) Lines from class 1 and 2, with amplitude respectively 1 and 0.75 and sigma of 3 for both classes. (d) Lines from class 1 and 2, with amplitude respectively 1 and 0.75 and sigma of 8.0 for both classes.(e) Lines from class 1,2 and 3, with amplitude respectively 1, 0.55 and 0.25, and sigma of 5.0, 3.0 and 10.. (f) Lines from all classes, with amplitude respectively 1, 0.75, 0.55, 0.25, 0.1 and sigma of 5.0, 4.0, 3.0, 2.0 and 1.0.*

$$N_{star}^{noise} = \sqrt{N_{star}} \tag{6.6}$$

where N indicates always photons number.

Background's shot noise The sky during the light acquisition from a specific target contributes, usually with a large fraction of photons, polluting the observations. The background's light comes from either natural phenomena (stars, galaxies, reflected sunlight from dust particles, etc..) or human-made sources (city lights, warning lights, airplanes, etc..). The background light can be measured with background empty observations, then subtract the total amount without target to our data flux. The noise from the sky is calculated as:

$$N_{background}^{noise} = \sqrt{N_{sky}(pixel) \cdot n_{pixel}} \tag{6.7}$$

Thermal noise The thermal motion of the electrons in the CCDs produces the so-called "dark current": a relatively small electric current present in all diodes and in general photosensitive devices (e.g. a photomultiplier tube, a photodiode). The presence of charges is due to the detector itself, observable even if no outside radiation is entering the device. Usually it is necessary to take a series of dark exposures to have an average of the thermal contributions to the toal noise. However, since there are important random fluctuations from the average, it is impossible to totally cancel out this contribution. The noise can be calculated as follow:

$$N_{therm}^{noise} = \sqrt{N_{therm}(pixel) \cdot n_{pixel}} \tag{6.8}$$

For CUBES, the design is expecting a dark current of 0.5e/ pix/h (assuming a temperature of 165 K). For more information see Chapter 5.

Readout noise The measurement process of the CCDs is afflicted by a systematic error in the final charge calculation for electrons' packet. It is possible to calculate the readout noise per pixel as:

$$R = \sigma_{counts} \frac{n_{electrons}}{counts} \tag{6.9}$$

For CUBES, the expected readout noise is 2.5erms (at 50 kHz), and a pixel-response non-uniformity of 3%.

The final contribution comes from the variance of all the pixels which fall inside the photometric aperture as:

$$N_{readout}^{noise} = \sqrt{R^2 \cdot n_{pixel}} \tag{6.10}$$

The final total noise is the addition of the different terms:

$$N_{total}^{noise} = \sqrt{N_{star} + N_{sky}(pixel) \cdot n_{pixel} + N_{therm}(pixel) \cdot n_{pixel+R^2 \cdot n_{pixel}}} \quad (6.11)$$

In case of faint stars, as white dwarfs, it is clear from Fig. 6.21 that the thermal noise or readout noise can definitely affect the final result. Now, if we consider a variable x(t), and the corresponding noise term in the equation does not depend on the variable itself, it is an additive noise term; otherwise is a multiplicative term. It is then possible to divide the noise in two main regimes: 1) multiplicative regime, where only the shot noise from the star is considered; 2) additive regime , where all terms are included in the final calculation.

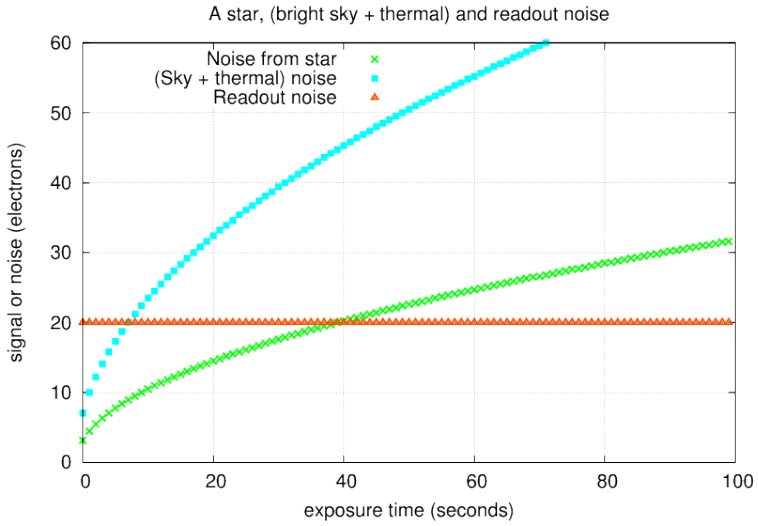

Figure 6.21: *Trends of the different noise components respect to the exposure time: the thermal and sky background noise becomes dominant at long exposure times; the readout noise is constant, since it is a systematic noise from the detector. From Richmond (2023).*

Synthetic noise: multiplicative regime

The synthetic spectra generated following this method provide a theoretical example of possible polluted white dwarfs observations. In this step, we added noise to our sample. I must point out that the noise treatment in this work does not consider a a realistic representation of the possible different noise sources, so both the additive and multiplicative regime will be covered with a constant parameter.

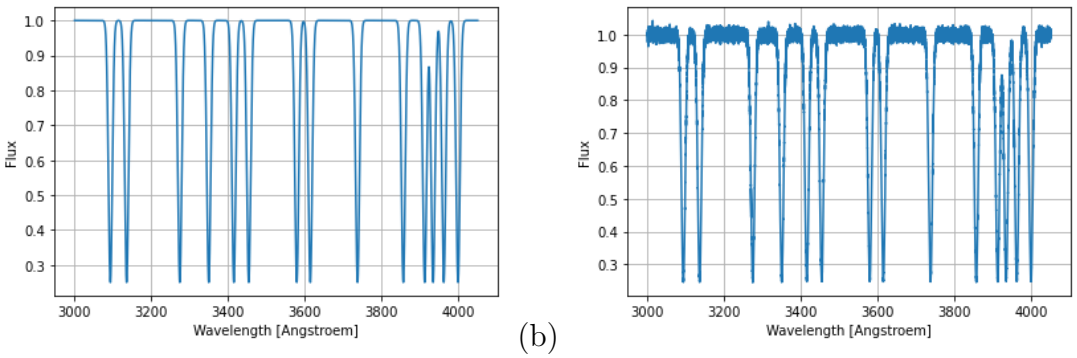

(a) (b)

Figure 6.22: *Example without noise (case (b) of Fig. 6.20) and with a noise level of standard deviation 0.01 added. The flux is* $erg \cdot cm^{-2}s^{-1}\dot{A}^{-1}$*, the wavelength in* $\dot{A}$*.*

A

A set of random noise data points was added to each spectrum, using numpy.random function (numpy (2023)). This Numpy package draws random samples from a normal distribution. The noise depends on three parameters: 1) y-axis zero value (here set to 1 to avoid absorption lines to be negative) 2) standard deviation of the random noise distributionσ_{noise} 3) length of the random samples (here the same as the number of data points in our spectra). It is clear that, as in the case of the line's width, σ_{noise} could be considered direct expression of the noise level respect to the continuum, since we are normalising the spectrum at 1.0 $erg \cdot cm^{-2}s^{-1}\dot{A}^{-1}$ and multiplying the noise distribution with the normalised flux. To understand the meaning behind σ_{noise}, see Fig. 6.18.

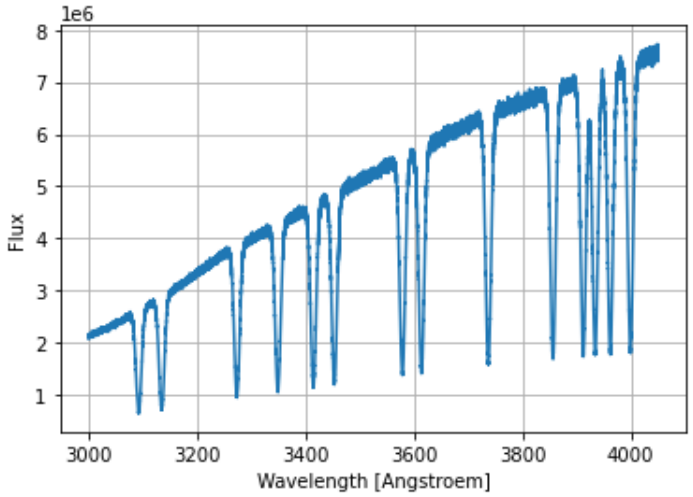

Figure 6.23: *Re-shaped spectrum from Fig. 6.22. The flux is* $erg \cdot cm^{-2}s^{-1}\dot{A}^{-1}$*, the wavelength in* $\dot{A}$*.*

As discussed earlier, we have created four classes of noise from σ 0,001 to 0,05, and added the noise to the 2800 spectra polluted with lines. After noise injection, we saved the spectra in two different versions: flat and blackbody shaped (see Fig. 6.23. Using the continuum fit function saved from the first step, we returned to the original spectrum temperature-peak shaped: this will be necessary to calculate the

final S/N per pixel. The flat spectra instead will be used for fitting each line in the next step.

6.2.5 Atmosphere modelling

One last step was the atmosphere integration in the simulation: CUBES, as mentioned in Chapter 5, will be installed as part of the ground telescopes group of VLT (Very Large Telescope). Atmospheric extinction is particularly important at the ultraviolet band: as we can see in Fig. 6.24, nearly 70% of the radiation does not reach the ground. Usually the main sources of attenuation in the atmosphere are Rayleigh scattering by air molecules, scattering by particulates, and molecular (telluric) absorption. The last is the dominant one in the range 300-400 nm, due to molecular oxygen and ozone. In the Atacama desert, conditions are favorable for observations due to the high altitude and dry weather, as in La Silla and Cerro Tololo. Cerro Paranal is much closer to the Pacific Ocean (12 km), the composition of the troposphere's aerosols could affect the results and must be considered (Patat et al. (2011)).

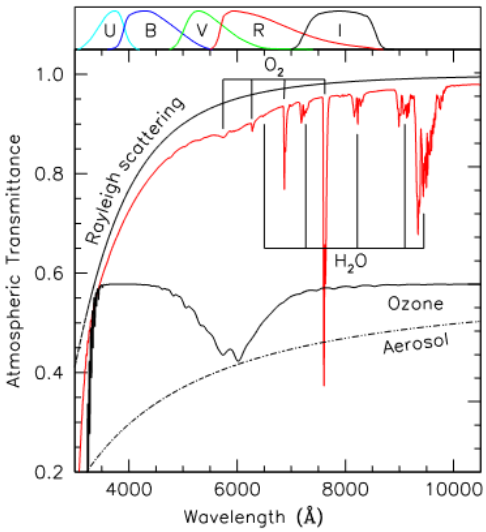

Figure 6.24: *Modeled atmosphere transmittance in the range 2000-10000 Åcomputed for Cerro Paranal with the LBLRTM code (Patat et al. (2011)), for airmass equal to 1. The main extinction sources in the range we are interested are Rayleigh scattering and ozone molecular absorption lines. The curves on the top panel trace the normalised U BVRI Johnson-Cousins passbands.*

I used the atmosphere transmittance spectrum given by the CUBES developers and used during the first simulations for the instrument. It is visible in Fig. 6.24: it represents the yearly average conditions at Paranal (coordinates: -24°.6274, -70°.4039, apparent horizon altitude -1°.95, altitude of the site 2640 m) and at the zenith for VLT (airmass = 1), available thanks to ESO databases.

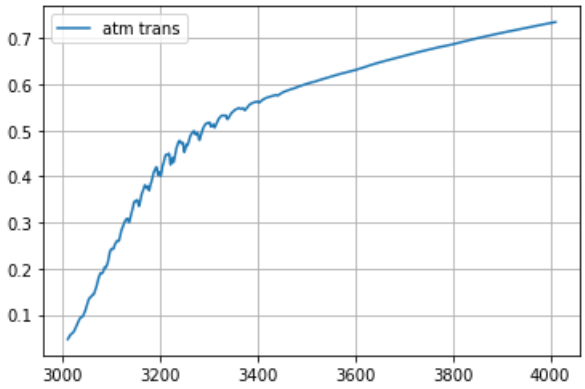

Figure 6.25: *Transmittance spectrum for VLT at standard conditions.*

In addition, the transmittance T(x) changes with airmass following an exponential law:

$$T_X(\lambda) = e^{ln(T_0(\lambda))X} \tag{6.12}$$

As we know, the total attenuation obtained depends on location and altitude, so conditions of the sky and airmass (extinction is lowest at the observer's zenith and highest near the horizon). Here, airmass X=1 indicates the zenith.

6.3 Synthetic spectra analysis and main parameters estimation

At the end of the synthetic spectra production, a statistical analysis was carried out. It was focused on: 1) noise limit for lines detection; 2) minimum amplitude and line profile's width to resolve the line; 3) S/N at fixed exposure time (with the use of the ETC presented in 5); 4) effect of the atmosphere dispersion.

6.3.1 Lines fit and detection

The first step was line fit on all the lines injected with a Gaussian function (see 6.18). The mean was assigned as the wavelength of the line we wanted to analyse (from the list in 6.12) and the standard deviation was calculated as:

$$\sigma_{line} = \sqrt{\frac{1}{N}\sum(x_i - \bar{x})^2} \tag{6.13}$$

where y_0 and the amplitude A were retrieved with an estimation through the python package CurveFit (scipy (2023b)). Initial guess sets on average the parameters at A= -0.9, y_0= 1, while the estimation for mean wavelength peak of the line and the sigma-value of the Gaussian function were calculated directly from the line. Based on the input characteristics of the lines, we set bounds on the fitting function ($0.05 < A < 1.1$, $0.5 < \sigma_{line} < 10.0$).

The fit had a parameter maxfev (the maximum number of function calls) to 5000; if the fit was not found, it will report "Line not found". With this process it was possible to obtain the lines found for different noise levels/number of lines injected/line profile's width of the lines. For each parameter, the value obtained from the fit and the related standard deviation for each of them was saved in a separate ASCII file. The standard deviation for the single parameters was used to derive the dispersion of each of them respect to the expected value, during the CurveFit function calls. In total, the fit parameters were four (amplitude, y_0, wavelength of the peak, standard deviation of the function): we are interested in amplitude, line's width and mean location of the line in the wavelength range.

The process was repeated for both catalogues, different number of injected lines with different characteristics and with/without atmosphere extinction. At the end, number of lines detected with CurveFit for different spectrum types were calculated, to obtain a trend respect to changes in amplitude, line profile's width, number of lines injected and noise level.

6.3.2 S/R and relative errors

To estimate the detection threshold regarding noise and line overlapping, we estimated a S/R as:

$$S/R = \frac{N_{target}}{NOISE} = \frac{Flux_{target}}{Noise} \tag{6.14}$$

where $Flux_{target}$ is in $erg \cdot cm^{-2}s^{-1}\dot{A}^{-1}$ and the noise is the normal distribution in Paragraph 6.2.4. We considered spectra normalised to 1.0 $erg \cdot cm^{-2}s^{-1}\dot{A}^{-1}$ with all five lines classes injected, for both catalogues, and the selected wavelength were chosen from the best fit obtained in the first step. The main goal was to discover correlation between S/N and 1) amplitude; 2)line's width; 3) mean wavelength; 4) number of lines injected.

Parameter estimation value versus original input value

The fit function requires a value of input for each fit parameters (amplitude, line's profile width and mean wavelength of the line). To understand if the fit converged with a comparable estimation of the parameters (which results in a realistic line's simulation), we calculated the ratio:

$$\theta = \frac{x_{estimation}}{x_{input}} \tag{6.15}$$

where x is the parameter. The goal is to reach a value of the ratio of 1.0, which means that the parameter's estimation and input values are the same and the fit process is valid. The range of acceptance is the one already use for amplitude and line's width bounds on the fit from CurveFit. On the mean wavelength it would have been challenging to retrieve comparable values, and the presence of possible

lines blending effect would also have been not detected with a bound, this is the reason why this parameter is free from strict constraints (the range for the peak is usually around 40 $\dot{A}$).

Parameters significance

To understand the possible trends of the fit parameters, we derived a parameter significance as:

$$\Delta = \frac{\bar{x}}{\sigma} \tag{6.16}$$

where $\bar{x}$ is the mean for the chosen parameter and σ the uncertainty (square root of the variance obtained from the fit). The goal is to estimate the limit on amplitude and line position. The threshold condition is given by $\sigma > \bar{x}$: in this case, the line is not considered an optimal match and therefore it is considered not detectable. The process was repeated for both catalogues, different number of injected lines with different characteristics and with/without atmosphere extinction.

Exposure Time Calculator

The Exposure Time Calculator (see Chapter 5) is a simulation tools that allows to study the instrument's reaction to various imput spectra, reporting S/R at given exposure time and viceversa, in addition to magnitude for detection. It is possible to select various setup for the instrument, but we maintained the design proposed by Genoni et al. (2023). The analysis was conducted on various spectra, to test the S/R per pixel of CUBES at different 1)amplitude/line's width combination; 2) noise level; 3) atmospheric dispersion (airmass).

Chapter 7

Results and discussion

In this chapter we analyze the results from the statistical analysis as described in Chapter 6. The first paragraph highlights some noteworthy issues regarding the blackbody continuum function fitting process. Then the Exposure Time Calculator was used as mentioned in Chapter 6.3.2 to test different magnitude range of our targets, and a first selection of potential observable stars from Bergeron (2023) with temperature and luminosity required is showed. In addition, the atmosphere characterization is included in this section and the effect on the total star's flux received by the instrument. Secondly, the lines detection process is carried out with a fitting function on the single lines, and the number of lines per spectra type compared in different cases. At the end, we conducted a study on the fit parameters and their significance, to set the thresholds on S/N, line amplitude, width and location.

7.1 Blackbody continuum

Fitting the continuum reported issues regarding the second catalogue: with the Levenhagen 2017 catalogue, a threshold on the detectable wavelegth range can be set due to very strong H atomic lines from the Balmer series (the shortest Balmer wavelenght for hydrogen is at 364.5 nm). After lines injection and noise addition, it became impossible to distinguish properly metallic individual lines. There were issues with fitting the continuum in the region 380 to 400 nm, visible in Fig. 7.1

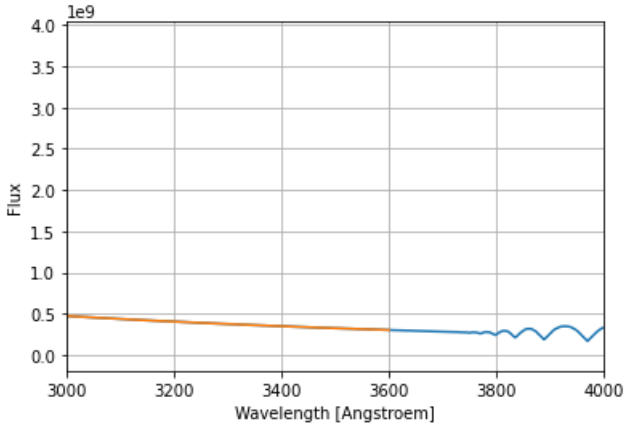

Figure 7.1: *The continuum fit of a spectrum from Levenhagen catalogue: it is clear that there are absorption lines as 3800 Å,which cause errors in the fit function (it tends to infinite).*

Due to the presence of Balmer lines, which are part of the synthetic spectra stellar atmosphere absorption lines from hydrogen, it was possible to research the S/N and exposure time limits for the instrument considering only the first part of the U-Band, up to 3600 $\dot{A}$, for the Levenhagen catalogue. The Balmer lines were as deep as other possible metallic lines, and would have affected the individual lines analysis in the next paragraph, incorrectly detected as heavy elements' lines.

Both catalogs showed a strong resemblance with a blackbody emission spectrum, and, since the range for effective temperature was small (around 1000 K), there is not visible difference in the fit result increasing temperature.

7.2 Exposure Time Calculator analysis

The next step was to conduct a S/N and exposure time analysis on the Exposure Time Calculator. As explained in Chapter 5, the ETC is able to retrieve the S/N per wavelength at constant exposure time. The configuration used for the ETC was:

- R >20'0000 (high);
- parallactic observations;
- magnitude 12.

This setting was proposed by Evans et al. (2023) for the study of exoplanets composition trough white dwarfs exogeology. The sky conditions were set as the standard proposed for the simulator: the reference magnitude at 22 mag/$arcsec^2$, the seeing at 5500 $\dot{A}$ and the airmass at 1 (for this part, the airmass is constant). The selected technical design was the one proposed by the consortium in 2022, a configuration with 6 slits of 1.5x0.25 arcsec with R over 20'000. In Table 7.1 the design characteristics for this study are illustrated. The S/N in the ETC is calculated as:

WL	3800.0	*actual wavelength (A)*
m(AB)	13.1	*Magnitude in AB units at 3800.0 (A)*
mSky(AB)	22.7	*Sky Magnitude/arcsec2 in AB units at 3800.0 (A)*
OVERALL_DQE	0.3395	*Overall DQE:Tel->CCD no slit throughput*
TOTAL EFFICIENCY	0.2292	*Total efficiency, including atmospheric absorption*
SLIT_LOS	1.0	*Slit transmission (for point source)*
VAR_DC	2.70e+01	*Variance of dark Current*
VAR_RON	337.5	*Variance of Read Noise*
PHOT_EL_STAR	2.16e+05	*Integrated object signal (photo-el)*
PHOT_EL_SKY	6.32e+01	*Integrated sky signal (photo-el)*
MAG_LIM	21.9	*magnitude limit at SNR=3*
SNR	464.32	*Signal-to-noise ratio for pixel of extracted spectrum*
SNR_Res	732.54	*Signal-to-noise ratio for Resolution element*
RESOLUTION	24039	*Resolving power at 3800.0 (A)*

Table 7.1: *Parameters selected for this work. The configuration is H2 (6k detectors of 15 μm), with atmosphere airmass of 1.*

$$SNR = \frac{N_{obj}}{N_{noise}}$$

$$N_{noise} = \sqrt{N_{obj} + N_{sky} + N^2_{detector}} \tag{7.1}$$

where N is the photons number. The noise from the detector is explained in Future improvements. The sky noise in this work is considered negligible.

The exposure time selected was 3600 s (60 min), the standard time proposed by the design group of the instrument in the high resolution mode. The reference V magnitude is set at 12 in the first step, which covers only partially the magnitude range for white dwarfs (some stars can reach up to 15,16, that would reduce the total S/R from the simulator). The process was repeated multiple times for the wavelength used in the local machine (see Table 7.1), and a distribution was saved in an excel file. The general S/N relation with the wavelength is in Fig. 7.2 and 7.3 (calculated at two different wavelegth peaks): as expected the S/R is increasing with exposure time. It is noticeable that even at $\lambda < 350$ nm the S/N is over 10.

The S/N calculation on the Exposure Time Calculation was conducted only through the Koester catalogue: Levenhagen 2017 has a finer sampling, and so far the web application does not support the possibility of uploading data point up to 10^5.

The V-magnitude of the target was considered as one of the possible parameters for an observational plan of the instrument. The magnitude is based on the UBV

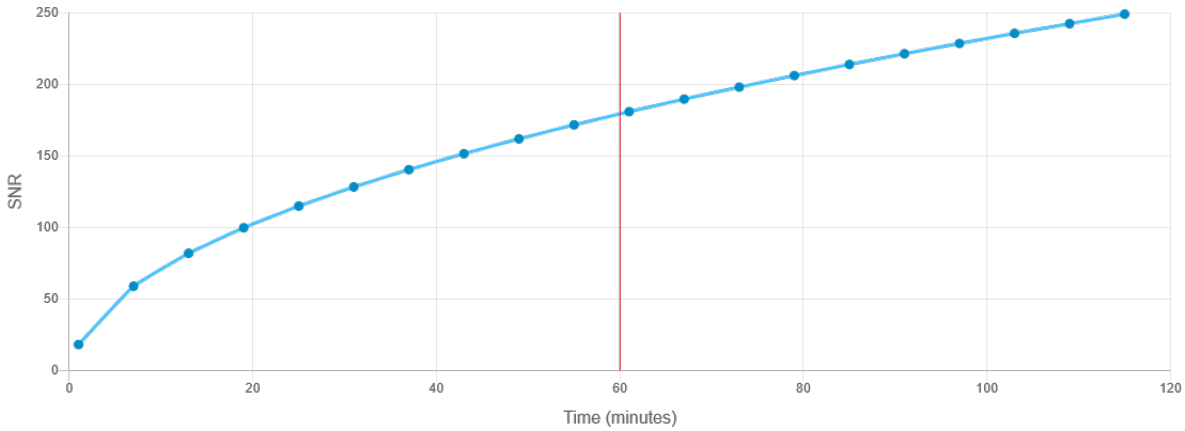

Figure 7.2: *ETC S/N trend respect to exposure time for λ= 3100 Å. The spectrum used is from Koester catalogue with a noise level of σ 0.005.*

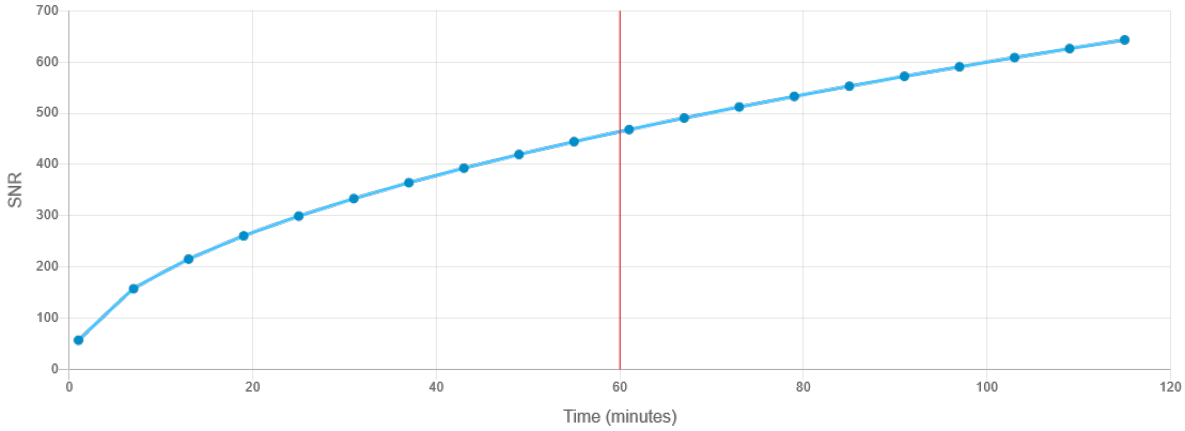

Figure 7.3: *ETC S/N trend respect to exposure time for λ= 3800 Å. The spectrum used is from Koester catalogue with a noise level of σ 0.005.*

photometric system or Johnson-Morgan system, where the apparent magnitudes of stars in the system are considered in the U, B and V band. The Exposure Time Calculator used the V magnitude input value to scale the final target photon number as:

$$N^V_{object}(\lambda) = N^V_0(\lambda)10^{\frac{-(V-V_0)}{2.5}} \tag{7.2}$$

where V_0 is read from the ASCII input file as $erg \cdot cm^2 s^1 \dot{A}^1$ and converted in photon $cm^2 s^1 \dot{A}^{-1}$. At the beginning of our project, the V magnitude was set at standard value of 12, for the best operating mode of the instrument. Nonetheless, looking at the white dwarfs' selection in Table 6.1, the maximum value of V magnitude is 16. We conducted a S/N analysis with spectra with standard lines ' profile width σ_{line} of 5.0, 4.0, 3.0, 2.0 and 1.0, fixed amplitudes at 1.0, 0.75, 0.55, 0.25 and 0.1 and a noise level of σ_{noise} of 0.005, but the V-parameter was set at 16. As visible in 7.4, the S/N is remarkably reduced up to our limit of 10 for $\lambda = 3050$ $\dot{A}$. For the spectra considered, the limit magnitude for S/N =10 is $m_V > 17$: above this value, the shorter wavelength area of the spectrum ($\lambda < 3100\dot{A}$) are highly affected by the signal reduction and lines are not detectable anymore.

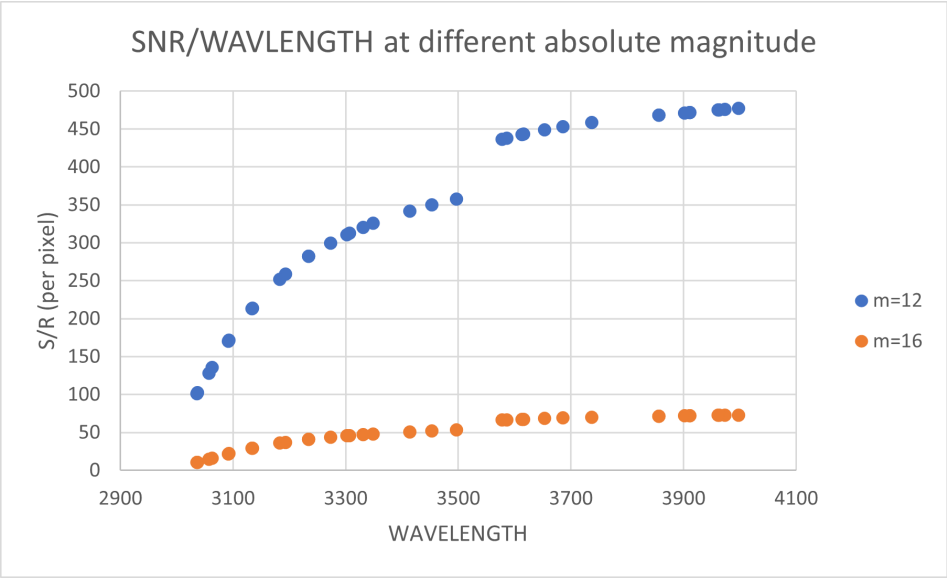

Figure 7.4: *S/N respect to wavelength for spectra with standard lines' profile width σ_{line} of 5.0, 4.0, 3.0, 2.0 and 1.0, fixed amplitudes at 1.0, 0.75, 0.55, 0.25 and 0.1 and a noise level of σ_{noise} of 0.005, but the V-parameter was set at 16.*

7.2.1 Atmosphere extinction

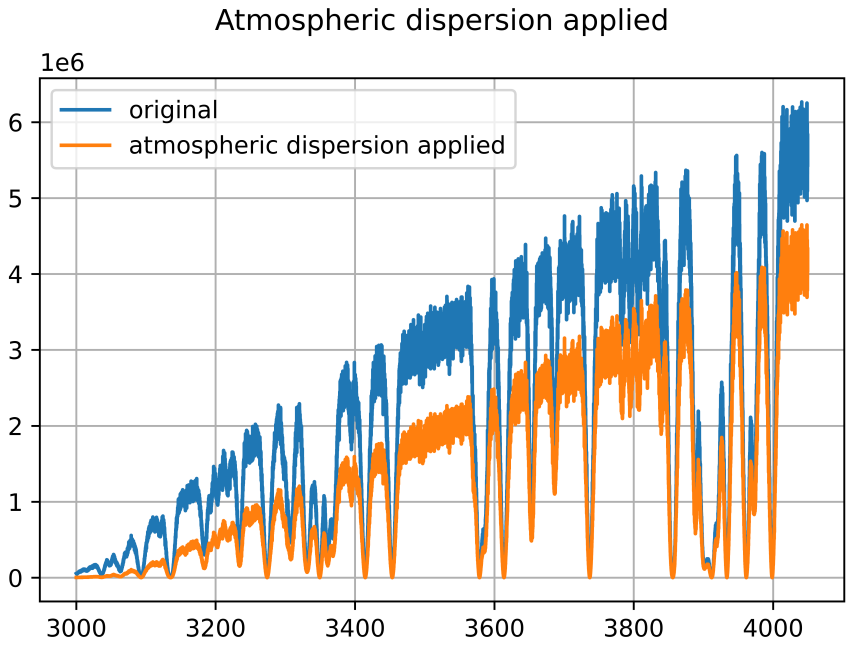

Figure 7.5: *Spectrum example from the Koester catalogue with atmospheric dispersion model applied (see Chapter6.12, X=1).*

As explained in Chapter 6.2.5, we modelled the atmosphere extinction and added it to the synthetic spectra of both catalogues. In Fig. 7.5 an example from Koester

catalogue, while an example from Levenhagen is in Appendix 9.1.2. To observe at which extent the atmosphere reduced the S/N, we decided to follow the same technique of the above paragraph. We calculated the S/N per pixel with the ETC over different spectra types with five classes of lines injected, with a range of line profile's width from σ_{line} 10.0 to 0.5, and amplitude fixed as 1.0 for class 1, 0.75 for class 2, 0.55 for class 3, 0.25 for class 4 and 0.1 for class 5. The process was iterated for 50 spectra per spectrum type. We repeated the calculation at different wavelength peaks, and compared the result with the spectra without atmosphere extinction. In Fig. 7.6 it is clear that the S/N is reduced homogeneously along the entire wavelength range. The minimum value is 40, which is still above the threshold of 10 we fixed for observations.

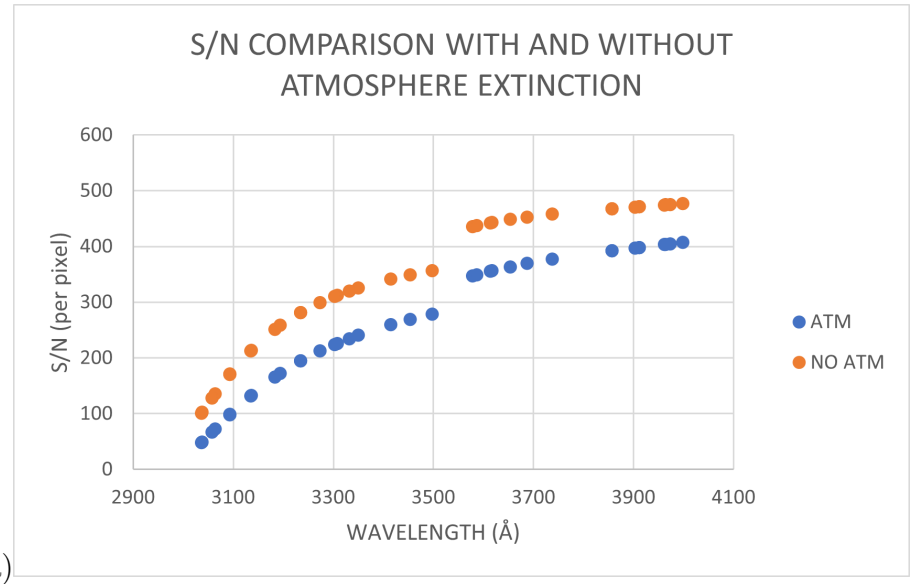

(a)

(b)

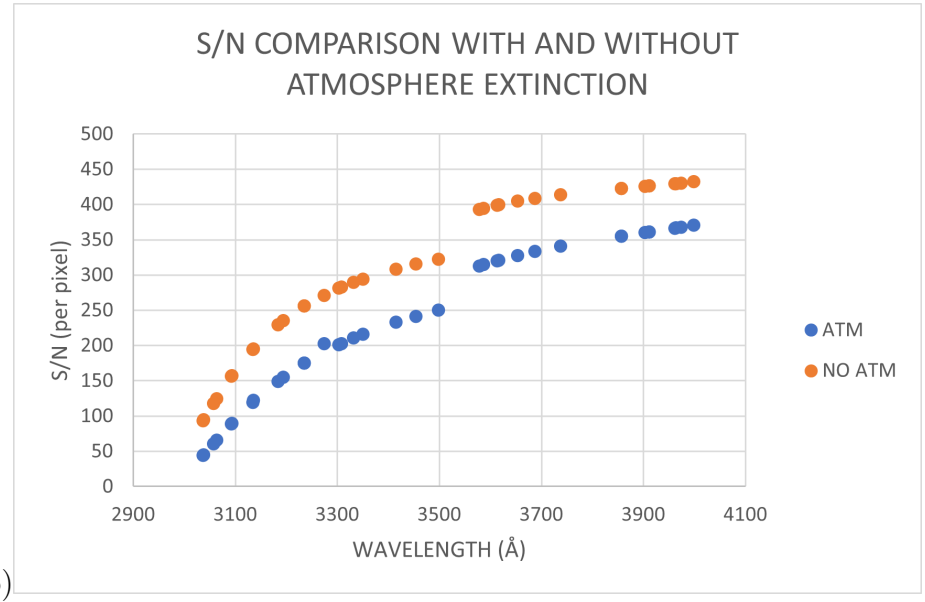

Figure 7.6: *S/N respect to wavelength for two different spectra types, with atmosphere included (airmass X=1): a) with 81 lines injected, line's width from 5.0 to 1.0, and noise level at σ_{noise}= 0.005; b) with 81 lines injected, equivalent width from 10.0 to 0.5, and noise level at σ_{noise}= 0.05.*

The atmosphere transmittance model used in equation 6.12 depends on the airmass considered. We repeated the analysis for X= 2 and X=5 on spectra from the Koester catalogue with five classes of lines injected at line's width respectively σ_{line} 5.0, 4.0,3.0,2.0 and 1.0 with amplitudes 1.0, 0.75, 0.55, 0.25 and 0.1 (noise level is fixed at 0.005).

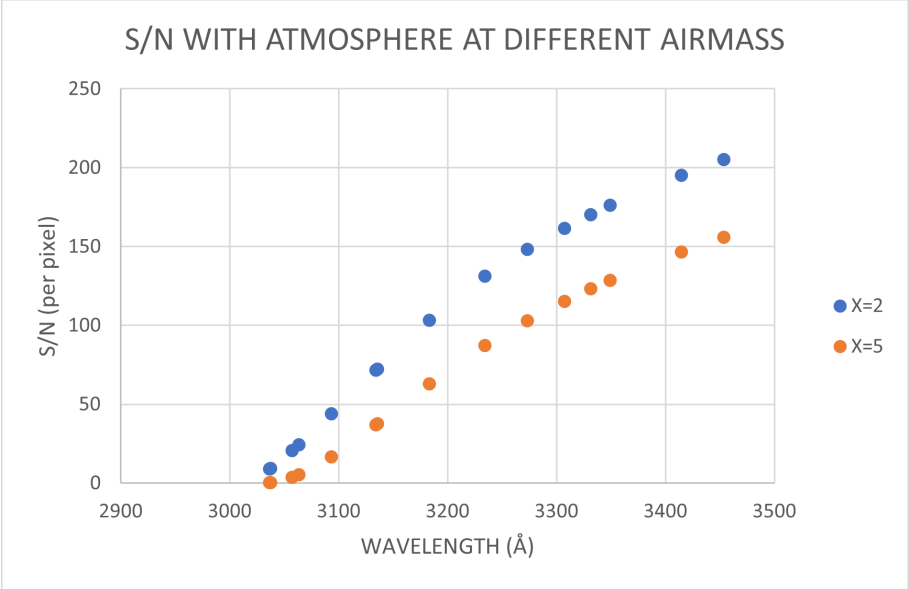

Figure 7.7: *S/N respect to wavelength for a Koester spectrum (81 lines injected, line's width from 5.0 to 1.0, and noise level at σ_{noise}= 0.005) with atmosphere included at airmass 2 and 5.*

The atmosphere dispersion at higher airmass has an important effect on the flux, as visible in Fig. 7.7: at X=2 it is already challenging to observe lines below $\lambda < 3100\dot{A}$. The S/N is 9.14 at 3036 $\dot{A}$, which is less than the threshold set at 10 and so the lines located in this part of the spectrum would not be detected.

7.2.2 Results from the ETC

In general, the analysis on the ETC highlighted two major sources of light flux reduction: 1) high magnitude of the target; 2) high airmass atmospheric dispersion. Using the Bergeron (2023) white dwarfs catalogue, we researched targets with:

- V-magnitude from 11 to 17
- Effective temperature 5000-10'000 K.
- Metals lines detected on the surface.

The first results are in Fig. 7.8. It is noticeable that on 70'667 white dwarfs, only 20 met the requirements in the database. The stars in this selection are potential targets for CUBES, based on magnitude and temperature parameters, but in the future it is possible this number would increase before the instrument will be operative, allowing observations on more targets.

Identifier	Right ascension	Declination	Spectral type	Teff [k]	log(g)	Distance [pc]
2MASS J06214164-4016187	06 21 41.77	-40 16 24.55	DZ	5919.0	8.0	23.68
87GB 103758.5+063247	10 40 31.63	06 17 21.70	DZ	7521.0	8.0	
EGGR 391	13 30 58.83	30 29 52.01	DZ	6274.0	8.205	25.54
EGGR 554	23 15 19.44	-02 09 37.76	DZ	6337.0	8.078	29.72
G 163-28	10 57 47.89	-04 13 32.72	DZ	6534.0	8.033	36.35
GD 17	01 49 34.52	24 00 46.86	DZ	8762.0	8.086	43.68
GD 401	22 18 00.99	39 08 40.53	DZ	8354.0	7.999	48.17
GJ 1211	17 08 07.95	02 57 30.72	DZ	6259.0	8.07	17.85
GJ 1276	22 53 56.06	-06 47 05.39	DZ	4323.0	8.141	8.54
GJ 283 A	07 40 22.06	-17 24 57.84	DZA	7461.0	7.976	9.15
Gaia DR2 3011223668834627328	05 54 42.97	-10 35 23.79	DZ	6089.0	8.003	15.29
NAME HL 4	05 55 10.10	-04 10 44.14	DZ	4534.0	7.955	6.44
Ross 640	16 28 24.34	36 46 27.79	DZA	8177.0	7.97	15.90
WD 0816-310	08 18 40.56	-31 10 32.90	DZ	6535.0	8.2785	19.36
WD 0840-136	08 42 48.17	-13 47 13.61	DZ	5627.0	8.321	14.81
WD 1009-184	10 12 01.28	-18 43 33.48	DZ	5715.0	7.952	18.09
WD 1532+12	15 35 05.63	12 47 42.32	DZ	5969.0	8.167	19.25
WD 2138-332	21 41 57.33	-33 00 31.61	DZ	6908.0	8.0455	16.11
WD 2216-657	22 19 48.83	-65 29 27.81	DZ	9770.0	8.09	25.53
Wolf 28	00 49 11.22	05 22 35.60	DZ	5908.0	8.105	4.31

Figure 7.8: *Table with a selection of WDs that meet the requirements specified above. From Bergeron (2023).*

7.3 Results from the single line fit

To simulate the possible line detection technique of CUBES we used a python code based on CurveFit (scipy (2023b)) to fit the single lines. The process involved single line fit for a total of 81 lines injected, and for each line it saved in a separate ASCII file the fit parameters and relative standard deviation; in addition, a PDF file with single line plots was printed.

INTENSITY	WAVELENGTH	ELEMENT
1000	3093.102	V II
1000	3135.480	Na II
1000	3273.960	Cu I
1000	3414.764	Ni I
1000	3453.510	Co I
1000	3613.831	Sc II
1000	3736.901	FeI
1000	3856.017	Si II
700	3686.555	Cu II
600	3234.513	Ti II
400	3183.992	V I
200	3888.646	He I
140	3368.936	Sc II
8	3497.525	Mn II

Table 7.2: *In the table the most detected lines in the sample (data from NIST (2013)).*

The first step in the analysis was to create a selection of the lines that were detected in all the synthetic spectra. The fit was considered converged if the bounds on the parameters were satisfied (we used the bounds function from CurveFit) within 5000 iterating attempts. The input parameters were: 1) amplitude (0.1 to 1.0); 2) line's profile width (0.5 to 9.0); 3) mean wavelength value for the line (usually a range of 30-40 $\dot{A}$). The input parameters are estimated line per line (lines have different characteristics at injection, see Chapter 6).

Typical errors in the fitting process were (visible in Fig. 7.9):

- 1) overlapping of two lines of nearly same amplitude, incorrectly recognised as one line by CurveFit;
- 2) presence of two emission lines which are however spurious features due to the added noise, and they are then not recognised;
- 3) a weak line nearby a very strong line not detected;
- 4) a forest of lines with similar amplitude within a very short range of wavelengths, which are not resolved.

From the final lines selection in Table 7.2 , we observed that it is identical for both catalogues: it appears that the major issues regarding lines identification in this step were related to line's width, amplitude, noise and mean location in the range of wavelength, but not on the different shape of the two catalogues or the initial data points (blackbody continuum and so effective temperature of the star). It is also important to notice that lines have been injected always considering the initial supposed intensity from the NIST catalogue, and strongest lines have deeper amplitude. Observing the selection, we see that most of the detected lines were either intense (relative intensity of 1000 in the original catalogue) or relatively isolated respect to the others (avoiding overlapping). In particular cases, very strong lines (amplitude 1.0) were nearly at the same wavelength of weak lines (amplitude 0.25 to 0.1): in this case, only the strong line was detected (example: at 3613.81 A we have Sc II line with a relative intensity of 1000, and at 3613.69 A the Cr I line of relative intensity 90).

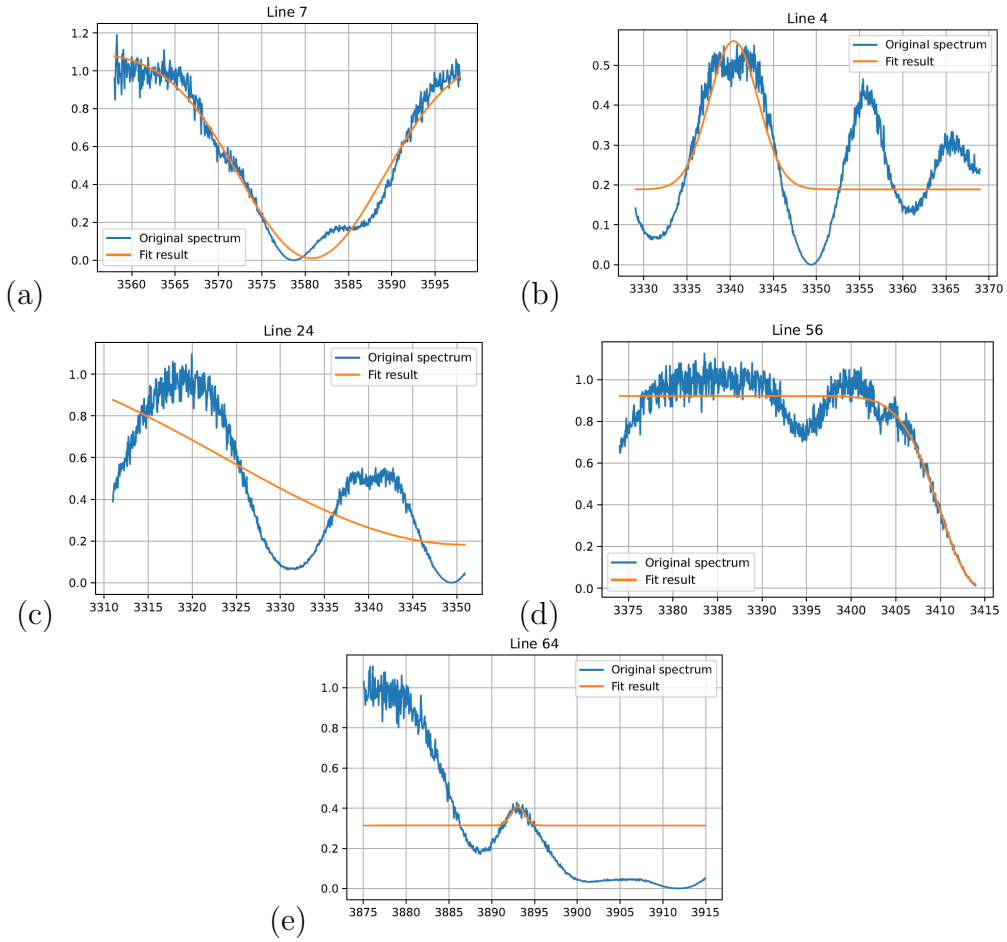

Figure 7.9: *A spectrum line-fitted from Levenhagen 2017 catalogue with some of the common fit errors highlighted above: a) overlapping of two lines; b) fit on emission features due to noise; c) two important lines not recognised for similar peak amplitude; d) a weak line nearby a very strong line not detected; e) a forest of lines with similar amplitude within a very short range of wavelengths.*

7.3.1 Detected lines

We analysed the fit results based on the spectra lines' characteristics (amplitude, line's width), the noise level and the different effective temperature, studying the number of detected lines within the fitting process. This process was done on the Koester catalogue.

CLASS	INTENSITY	NUMBER OF LINES
1	1000	14
2	600-900	16
3	100-500	6
4	10-100	25
5	1-10	12

Table 7.3: *Injected lines number per type (class) with relative intensity from NIST (2013).*

Line's profile width

The line profile's width depends, as explained in Chapter 6, on the sigma-value of the injected line's equation 6.13. The values's range for the parameter was 1.0 to 8.0 (broad lines) for this study, and we divided the lines injected per classes based on the width, as visible in Table 7.3. We conducted the analysis on 50 spectra per single catalogue, and we calculated the lines passing the required parameter's bounds (here 0.5 to 9.0 line's width, depending on the line) with the fitting function from CurveFit (numpy (2023)). After we obtained the number of lines per spectrum per line profile's width class (see Table 7.3), we averaged it over a folder of 50 samples (the samples have effective temperature and gravity logarithm range from T=5000 K, log g= 6.5 $g \cdot cm^{-2}$) and distributed. The results are in Fig. 7.10.

There are four distributions in the Fig, one per each line's width class. The lines' number increases from 8 lines for σ_{line} equal to 1.0 to 12 lines for σ_{line} equal to 8.0. The number increases with the line's width as expected, because the fit function is able to easily distinguish broader lines. The number of lines is around 12-15, which is coherent with the number of lines injected per width class (which ranges from 10 to 20).

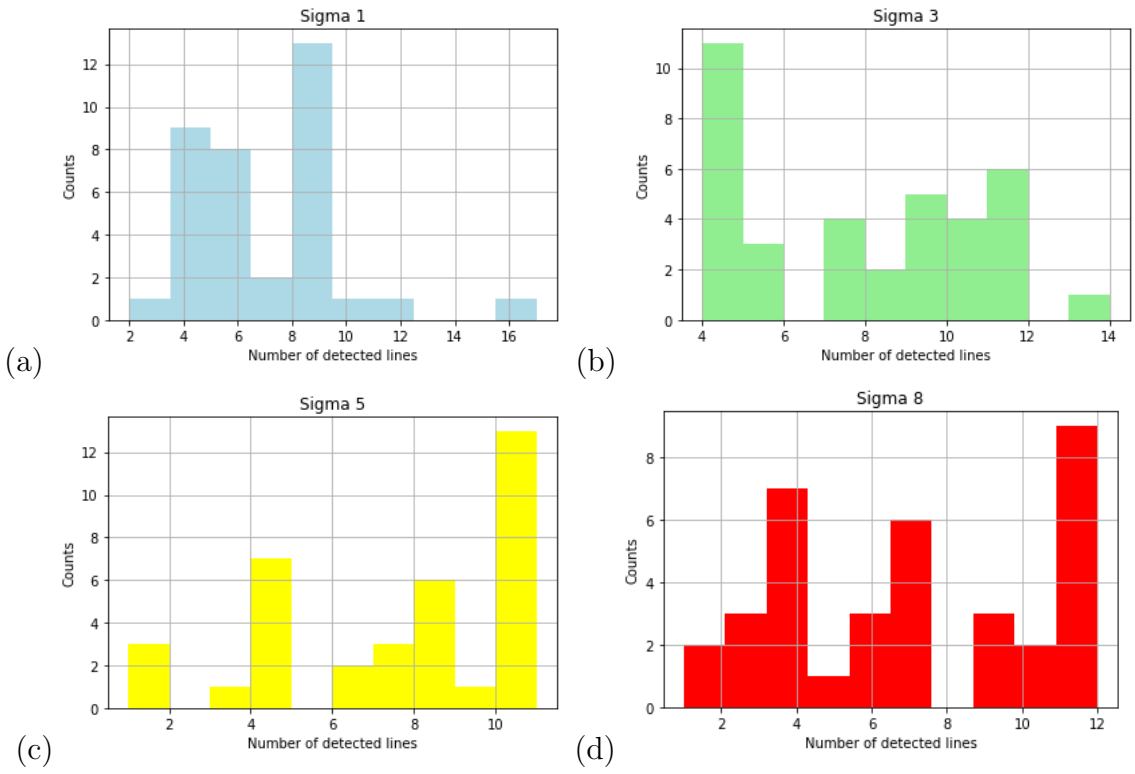

Figure 7.10: *From Koester catalogue the distribution of the lines detected per spectrum, considering: a) line Gaussian function with σ_{line}=1.0; b) line Gaussian function with σ_{line}=3.0; c) line Gaussian function with σ_{line}=5.0; d) line Gaussian function with σ_{line}=8.0. In all different spectra types, the process was iterated over 50 spectra of different effective stellar temperature.*

Amplitude

The second analysis step regarded the amplitude of the lines we injected, referred as parameter A in equation 6.13. Selecting spectra with lines injected with σ_{line} 3.0 and 5.0 and the amplitude in a range from 0.25 to 1.0, we compared the number of lines found by CurveFit. In this case, since the lines had the same profile's width in the spectra but different amplitude, the final number is calculated considering 81 lines injected, not divided per class as above.

The result is visible in Fig. 7.11: in both cases, as the amplitude increases the detected lines number increases as well, even if not significantly. But it is also evident that the trend has important error bars, and consequently it can not be concluded a significant parameter dependency.

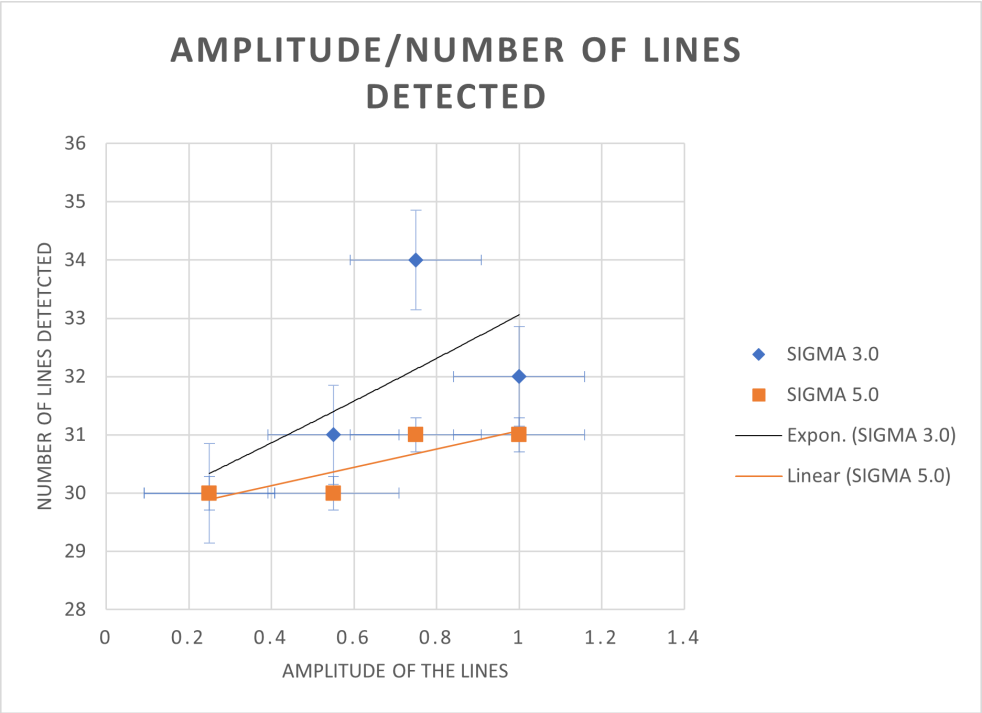

Figure 7.11: *The number of lines detected at increasing amplitude of the line. In blue the lines with σ_{line} 3.0 and in orange the 5.0. It is highlighted the trend for both data sets, respectively with an exponential and linear function, and relative error bars. In all different spectra types (different colors), the process was iterated over 50 spectra of different effective stellar temperature.*

Added noise

The last phase of the analysis regarded the overall noise level used (reported as S/N). In Fig. 7.12 we built a plot of the number of detected lines per S/N, where each dot is the number of lines found by CurveFit per lines' class (see Table 7.3) at different noise level. There is not an evident correlation between the noise level and the effectiveness of the fit method. The reason could be find in the use of a multiplicative regime for the synthetic noise, which only covers up to 5% of the flux. For higher noise cases, see Chapter7.4.2.

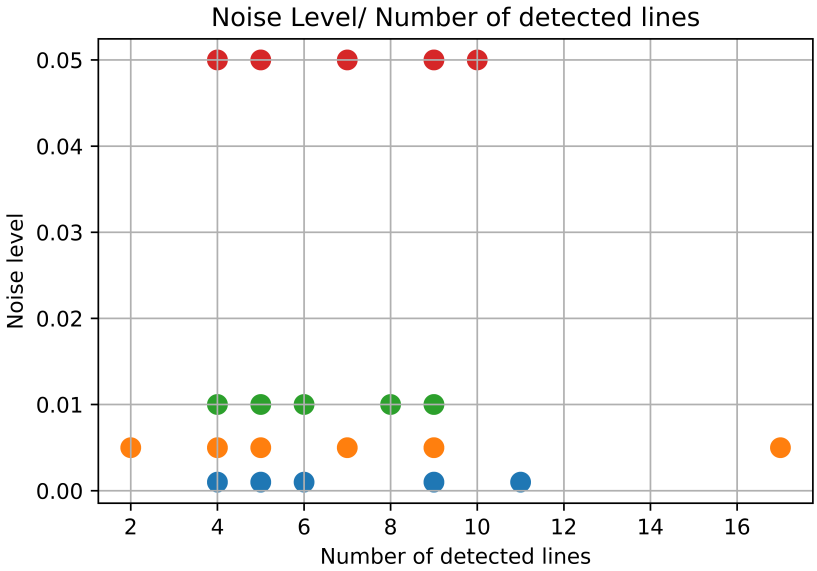

Figure 7.12: *The same spectra used in the above analysis steps here plotted by different noise levels (σ_{noise} of 0.001, 0.005,0.01 and 0.05). In different colors the same noise level spectra. In all different spectra types (different colors), the process was iterated over 50 spectra of different effective stellar temperature.*

Fit of special lines

A secondary process for line fitting was conducted on lines for which the fit converged during the first step of the analysis, however the parameters did not match the required bounds on the line (amplitude, line's width, mean wavelength value) for particular reasons:

- Double-peak lines: two lines with a very similar mean wavelength peak.
- Lines with low intensity near deep lines.
- Lines forest effect.

The fit function was modified introducing: 1) reduced wavelenght range for detection (usually CurveFit considers a range of 40 $\dot{A}$ respect the input mean wavelegth, here it was reduced to 20); 2) a double peak Gaussian function, as described in the equation below.

$$f = \frac{1}{\sqrt{2\pi}\sigma_1} e^{(\frac{-1}{2}\frac{(\lambda_1-\mu_1)^2}{\sigma_1^2})} + \frac{1}{\sqrt{2\pi}\sigma_2} e^{(\frac{-1}{2}\frac{(\lambda_2-\mu_2)^2}{\sigma_2^2})} \tag{7.3}$$

At the end of the analysis, we concluded that dense conglomerates of lines (etg. 3035-3070 $\dot{A}$) were in most cases not resolved, due to the total blending effect, as visible in Fig. 7.13.a. In this case, it is possible to have a detection but it must be considered that more than one line is detected at time. However, the double-peak function detected cases with only two lines partially overlapping. In Fig. 7.13.b an example of a strong line (3960-3965 $\dot{A}$) near a medium-amplitude line (3979-3975 $\dot{A}$)

detected with a double-peak Gaussian function. A threshold at 0.4 in amplitude was set for detection of the weak line, otherwise indistinguishable from the strong one. In Chapter 8.3, we described the possibility of solving these issues with a spectrum template.

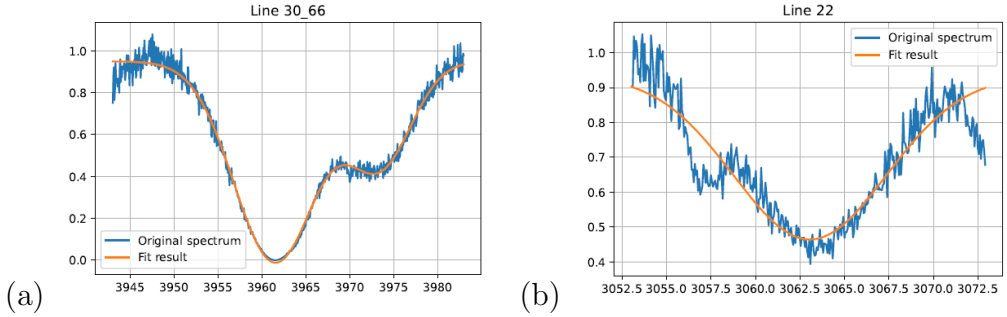

(a) (b)

Figure 7.13: *A spectrum line-fitted from Koester 2010 catalogue with two of the cases highlighted above: a) forest of lines, completely indistinguishable; b) overlapping of two lines, fitted with double-peak Gaussian function.*

7.4 S/N study

The analysis process proceeded with Signal-To-Noise estimation in different cases. As it is described in Chapter 6, the S/N is calculated per wavelength through the equation 6.14 , in which we first considered a multiplicative regime (see 6.2.4). The calculation was done at the continuum level of the normalised spectrum (signal equal to 1.0 erg/$cm^2 s\dot{A}$ for the continuum), and averaged over the entire spectrum. In this regime, four levels of noise were injected and the final S/N values were: 1) 1000 for σ_{noise} 0.001 ; 2) 200 for σ_{noise} 0.005; 3) 100 for σ_{noise} 0.01; 4) 20 for σ_{noise} 0.05. The σ_{noise} represents the standard deviation of the added random noise distribution.

7.4.1 Fit parameters

In this paragraph we analysed the fit parameters obtained with CurveFit for each detected line. As it is mentioned in the previous section, CurveFit has different outputs: fit function on the data, the free parameters indicated for the fit and a covariance matrix for the parameters themselves. In this research we are interested in the amplitude, the line's profile width and mean position in the wavelength range.

Extracting the parameter and their relative standard deviation (the diagonal of the covariances matrix is composed of the variances for each parameter; with a square root function it is possible to retrieve the standard deviation), we computed the parameters' estimation over input ratio (equation 6.15) and its significance (equation 6.16). In Chapter 7.3 we described the variety of possible spectra we produced, and the different characteristics are an advantage to better test the reliability of our system. The errors were calculated on the reliable lines that passed the fit function in the first step, mentioned in Table 7.2.

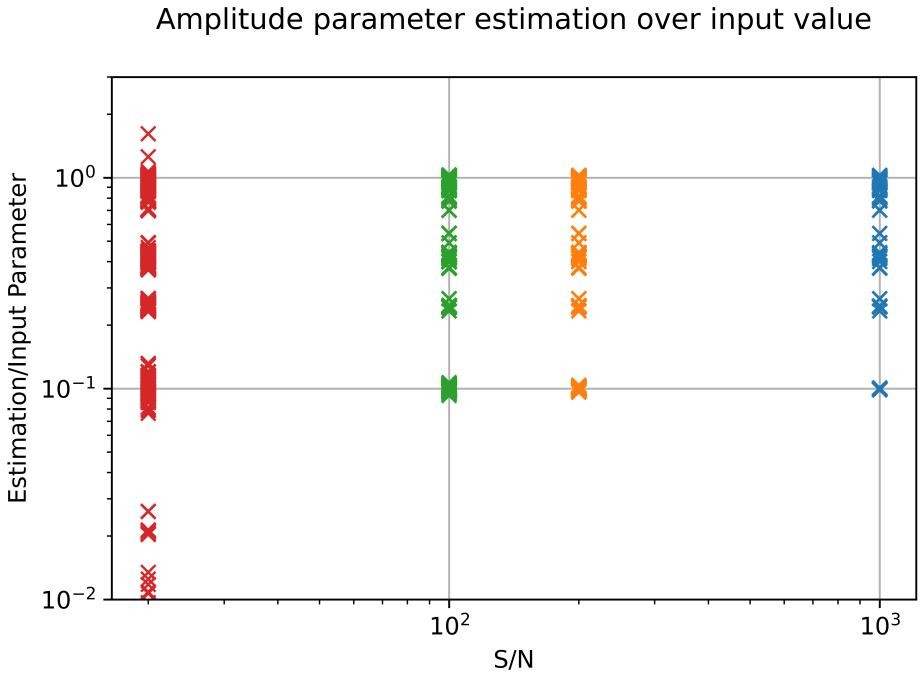

Figure 7.14: *From Koester catalogue the distribution of* $\frac{A_{estimation}}{A_{input}}$*, with five classes of injected lines at different amplitude (from 1.0 to 0.1) and line's profile width determined by* σ_{line} *1.0 to 10.0.*

In the next paragraphs, we illustrate for a range of spectra with different characteristics the results regarding the parameters' estimation and significance.

Spectra with 81 lines (0.1 <A<1.0, 1.0 < σ_{line} <10.0) and S/N 20 - 1000

First, we selected spectra with five classes of injected lines at different amplitude (from 1.0 to 0.1) and line's profile width determined by σ_{line} 1.0 to 10.0. We calculated the errors on the amplitude, the mean and the line's profile width. We plotted the relative distribution respect to the S/N. For each plot, a total of 200 spectra per noise level were analysed, with four levels of noise (at σ_{noise} 0.001, 0.005,0.01 and 0.05). In each graph, the lines are considered together independently from their characteristics (amplitude, line's width, mean wavelength).

Amplitude (A)

It was necessary to further reduce the data in the process, since there were lines for which the fit converged but the errors were higher than two times the parameter estimation. This data were discarded.

The ratio of amplitude estimation compared to the input amplitude used has on average a value between 0.1 to 1.0 (the injected lines have amplitude 1.0, 0.75, 0.55, 0.25 and 0.1), which represents a good fit result. It is also noteworthy that the ratio is affected by the increasing noise: at S/N of 20, the ratio is below 0.01, which means the amplitude obtained from the fit is becoming not comparable with the

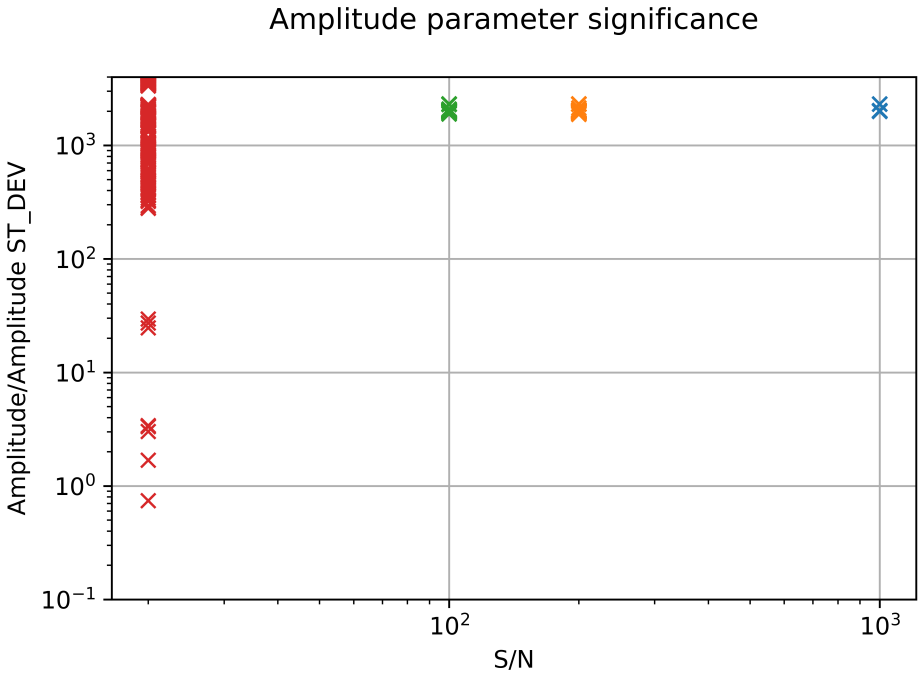

Figure 7.15: *From Koester catalogue the distribution of the amplitude significance* $\frac{A}{\sigma_{amplitude}}$*, where* $\sigma_{amplitude}$ *respect to the S/N for spectra with five classes of injected lines at different amplitude (from 1.0 to 0.1) and line's profile width determined by* σ_{line} *1.0 to 10.0.*

input value, and the fit is not optimised anymore.

The amplitude plot in Fig. 7.15 shows the significance for amplitude ($\frac{A}{\sigma_{amplitude}}$), where $\sigma_{amplitude}$ is the standard deviation of the fit Gaussian function of the line, respect to the S/N: this is the amplitude estimation significance in the fitting process. To confirm that the parameter is well estimated with the fitting Gauss function, the overall value of this ratio must be >1.

In general, the error is not comparable with the parameter, and the ratio is always optimal respect to the limit threshold. As expected, the higher the noise (at lower S/N) the lower is the ratio on the parameter (error is increasing); it is interesting that with a reduced S/N the distribution tends to widen, since the data points of weaker lines have lower values of significance respect to deeper lines. With a S/N of 1000 the significance is around 10^3, which is an error of 0.001% respect to the original parameter. Below a S/N of 20-50, the significance drops to 1 to 5 for certain lines, which was also expected (lines with lower amplitude, as Mn II or Sc II. Regarding the whole distribution, it is clear that the significance is very high, and considering the single line values for the errors it is noticeable that the fit function retrieved accurate fit up to 5% noise level.

Mean wavelength of the line (λ)

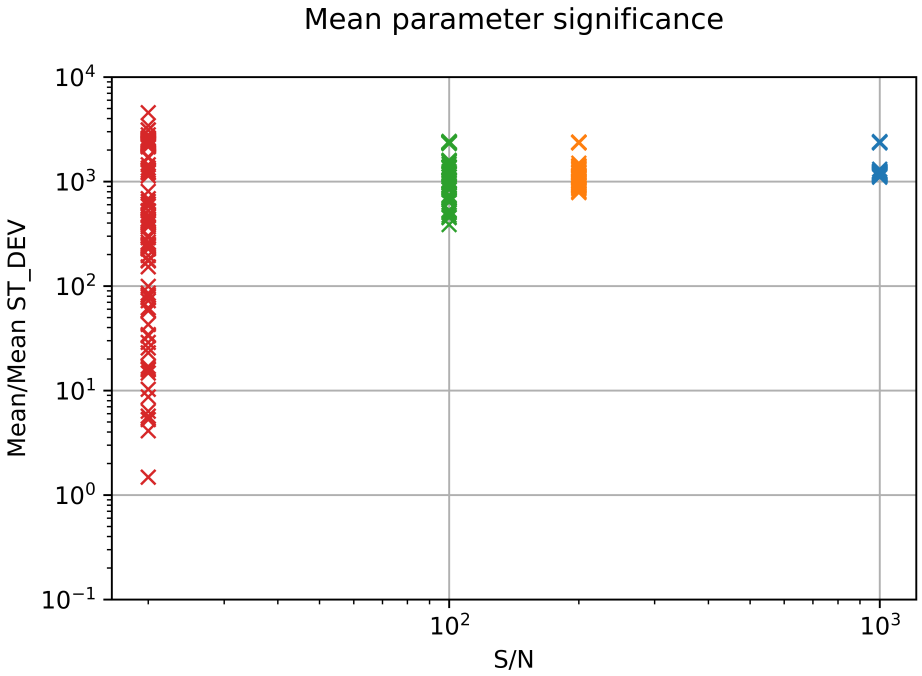

Figure 7.16: *From Koester catalogue the distribution of the mean significance* $\frac{A}{\sigma_{mean}}$*, where* σ_{mean} *respect to the S/N for spectra with five classes of injected lines at different amplitude (from 1.0 to 0.1) and line's profile width determined by* σ_{line} *1.0 to 10.0.*

We repeated for the mean wavelength of the line (peak position) parameter, in Fig. 7.16. The plot illustrates the $\frac{\lambda}{\sigma_\lambda}$, where the σ_λ represents the error on the line location in the wavelength range. Lines displacement in this work is mostly related to lines overlapping, while we are not considering other sources as atmospheric emission lines or scattering.
The final distribution for the mean wavelength significance is similar to the amplitude distribution, with a decreasing pattern respect to the S/N (the lower the S/N, the lower the significance). With a S/N of 1000, the significance is around 10^4 as for amplitude, and at lower S/N (below 50) reaches 1: certain lines are already beyond the set threshold for parameter significance. Also in this case the distribution tends to widen with decreasing S/N, due to weak narrow lines that are challenging to be fitted by CurveFit compared to broader lines.

Line's profile width (σ_{line})

The ratio of line profile's width estimation compared to the input shows a broader distribution compared to the amplitude. It is possible to notice values in which the line's width was underestimated (input value higher than estimation). This could be potentially due to the narrow lines (σ_{line} 1.0) that are not easily distinguishable from the noise. In general, most of the distribution highlights values for the ratio in the range 1.0 to 0.1, which means that the fit reported a comparable estimation for the input line's width.

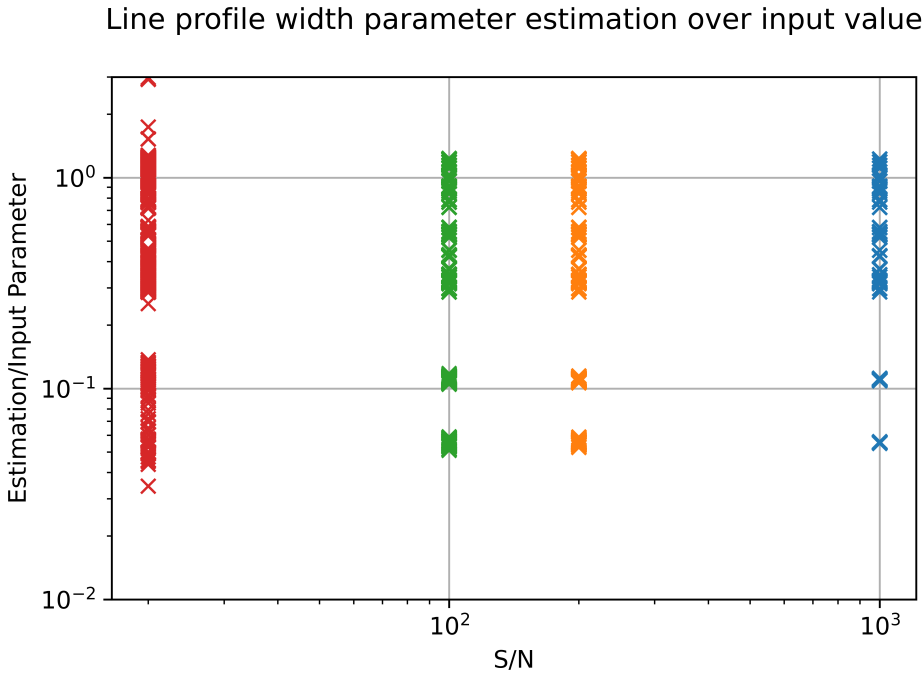

Figure 7.17: *From Koester catalogue the distribution of* $\frac{\sigma_{estimation}}{\sigma_{input}}$ *(line profile's width), with five classes of injected lines at different amplitude (from 1.0 to 0.1) and line's profile width determined by* σ_{line} *1.0 to 10.0.*

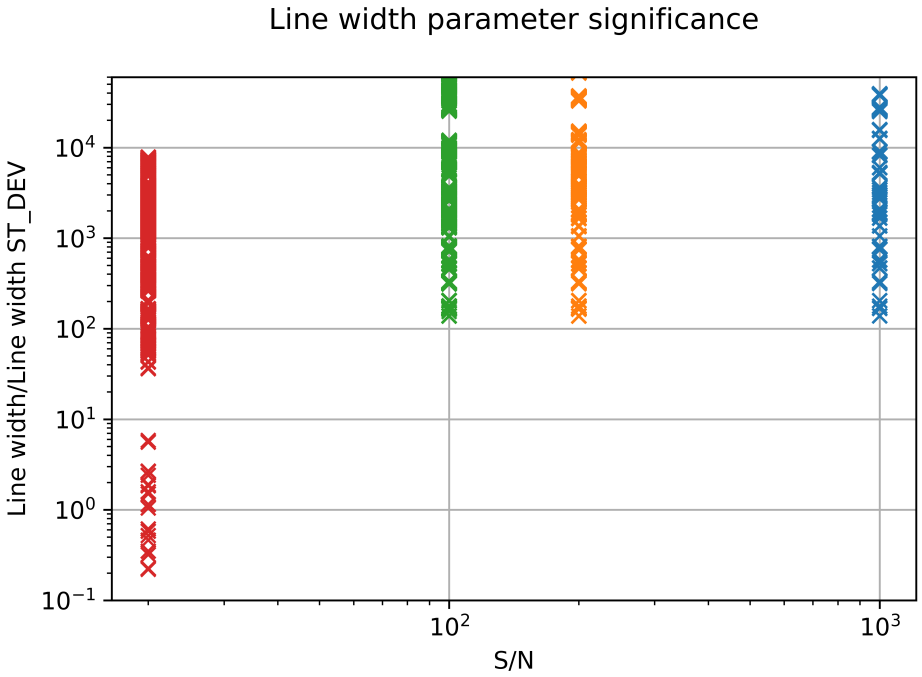

Figure 7.18: *From Koester catalogue the distribution of the width significance* $\frac{\sigma_{line}}{\sigma_{\sigma line}}$*, where* σ_{width} *respect to the S/N for spectra with five classes of injected lines at different amplitude (from 1.0 to 0.1) and line's profile width determined by* σ_{line} *1 to 10.*

At last, regarding the line's profile width, the results are higher respect the other parameters, with a significance up to more than 10^4. It is a striking feature that the line's width is estimated with high accuracy even for very narrow lines (σ_{line} around 0.5), as visible in Fig. 7.18. For a S/N below 50 the values fall to less than 1, probably having not detected correctly the narrow lines.

Spectra with 81 lines (0.1 <A<1.0, 1.0 < σ_{line} <10.0) and S/N 20 - 1000. Levenhagen 2017 catalogue.

We repeated the analysis on the Levenhagen catalogue with similar results (see the Appendix 9.1.3 for the plots). The amplitude and line's width parameter estimation/input is within the range 1.0 to 0.1 as in Koester case, however the line fit is deteriorated already at S/N 20 for amplitude, where the ratio is 10^{-2} and the estimation is smaller compared to the input value. It could be possible that the presence of additional hydrogen lines in the original spectrum (see Chapter 6.2.1) could affect the amplitude estimation (overall the effect is not significant). Regarding the significance of the three parameters, in general the results are comparable with the Koester catalogue.

Spectra with 81 lines at various amplitude's classes and constant line's width σ_{line} 3.0 and S/N 20 - 1000.

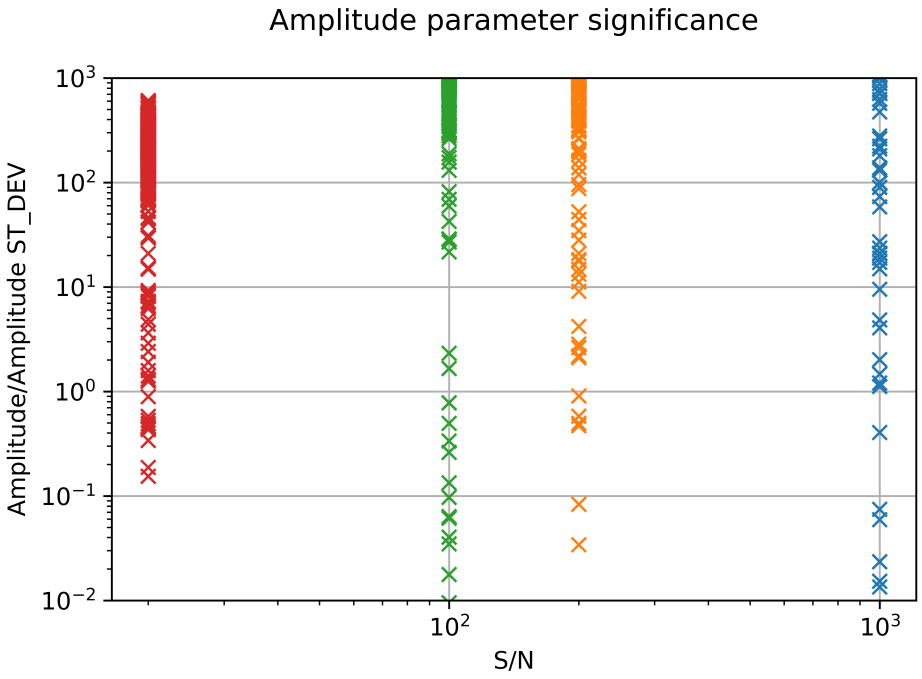

Figure 7.19: *From Koester catalogue the distribution of the amplitude significance* $\frac{A}{\sigma_{amplitude}}$*, where* $\sigma_{amplitude}$ *respect to the S/N for spectra with five classes of injected lines at amplitude 0.25,0.55 and 0.75 and line's profile width determined by* σ_{line} *3.0.*

Considering spectra with five classes of injected lines at selected amplitude (in order, 0.25, 0.55, 0.75, 1.0) and a constant line's profile width determined by σ_{line} of 3.0, we calculated the errors on the amplitude alone. We plotted the amplitude significance and compare the results at different S/N. In Fig. 7.19, for each plot a total of 200 spectra per noise level were analysed, with four levels of noise (at σ_{noise} 0.001, 0.005,0.01 and 0.05).
Overall, the amplitude distribution is deteriorated by the noise: the significance reaches below 10 for nearly all the different S/N, and there are no visible trends. The lines injected with an amplitude around 0.25 are the first to be not detected properly (error over three times the parameter estimation) when we have higher noise (up to 5%, multiplicative regime), and their presence reduced strongly the significance average value, widening the distribution in the plot. Considering that now the spectra have all the same amplitude for the lines injected, it is possible to notice that the amplitude value tends to overcome the noise level as potential first reason behind not detection of the line and, as consequence, high error on the parameter estimation (if the line is too weak in amplitude, detection would be difficult independently respect to the noise level).

Spectra with 81 lines at various line's width classes and fixed amplitude and S/N 20 - 1000.

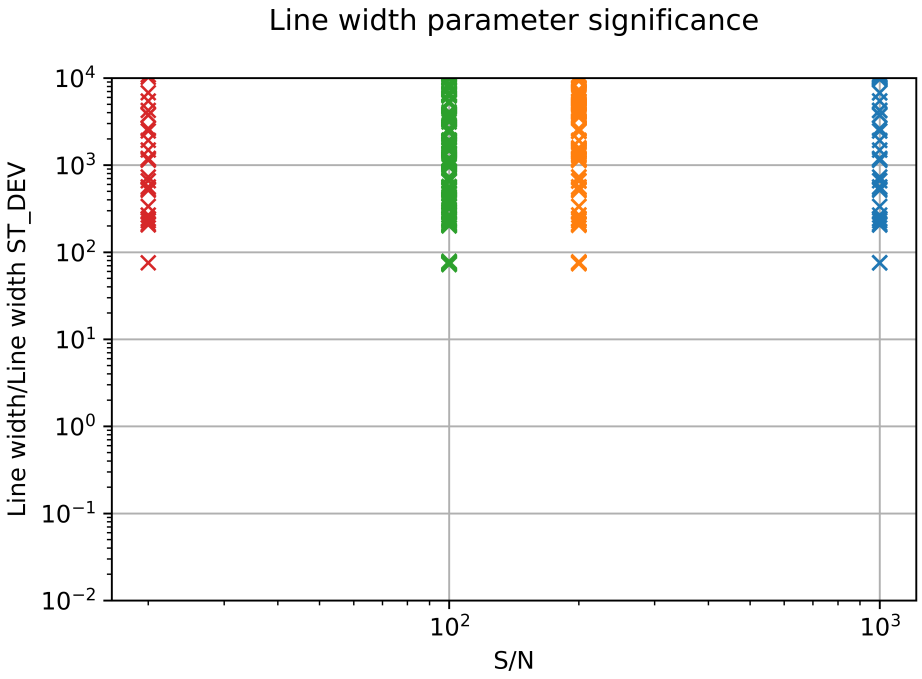

Figure 7.20: *From Koester catalogue the distribution of the amplitude significance* $\frac{A}{\sigma_{amplitude}}$*, where* $\sigma_{amplitude}$ *respect to the S/N for spectra with five classes of injected lines at amplitude 0.25,0.55 and 0.75 and line's profile width determined by* σ_{line} *3.0.*

In addition, we also tested spectra with five classes of injected lines at selected amplitude (in order, 0.25, 0.55, 0.75, 1.0) and a different line's profile width determined by σ_{line} of 8.0, 5.0 and 1.0 respectively. We calculated the errors on the line's width alone. We plotted $\frac{width}{\sigma_{width}}$ and compare the results at different S/N. In Fig. 7.20, for each plot a total of 200 spectra per noise level were analysed, with four levels of noise (at σ_{noise} 0.001, 0.005,0.01 and 0.05).
The line's width significance has nearly a constant value over different noise levels: it is probably due to the fact that broad lines are dominant in the distribution, and the error on width estimation for these kind of lines is very small. To prevent this issue, it is better to test narrow and broad lines separately, regarding the parameters values.

7.4.2 Additive noise regime

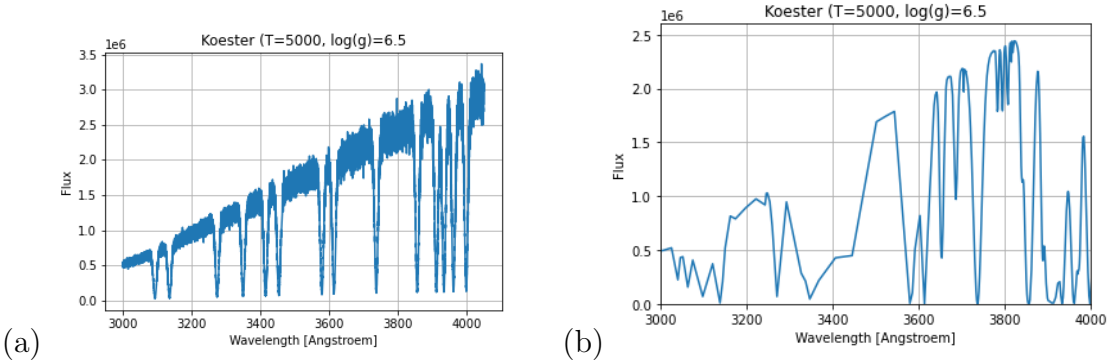

Figure 7.21: *From Koester catalogue, two example of spectra with: a) multiplicative noise; b) additive noise.*

In Chapter 6.2.4 we covered the different noise regimes considered in the project: so far, we worked in a multiplicative regime up to a noise level of 5%. To simulate a higher additive noise level, we selected to add directly to our data a free constant parameter:

$$S_{noisy} = Flux + C \tag{7.4}$$

where C is decided case by case from 0.1 to 0.8 (80% noise). Since the flux is normalised at 1.0 erg/$cm^2 s\dot{A}$, we added a comparable noise level respect to the continuum. In Fig. 7.21.b an example of additive noise at 60%.

Amplitude

Selecting spectra with five classes of injected lines at different amplitude (from 1.0 to 0.1) and line's profile width determined by σ_{line} 1.0 to 10.0, we injected noise in an additive regime from level 10% to 80% and fitted the lines in Table 7.2. In Fig. 7.22 the amplitude estimation significance for different S/N: 10% equals to S/N of 10, 50% to 2, 70% to 1.42. Increasing the noise level up to 80% and with a bound on the amplitude parameter, the fit function was not able to retrieve any line with a good estimation of the parameters: even if the line was "detected" by the function for fitting, the errors on the parameters resulted in a significance of 10^{-3} and not considered. Overall, the amount of lines detected at 70% is around 13-14, only with the maximum intensity (1.0), as described in the NIST catalog (NIST (2013)).

Line's profile width

Repeating the same process for the line's width in Fig. 7.23, we observe similar results. The line's width parameter has a significance estimated as 10^{-3} at noise

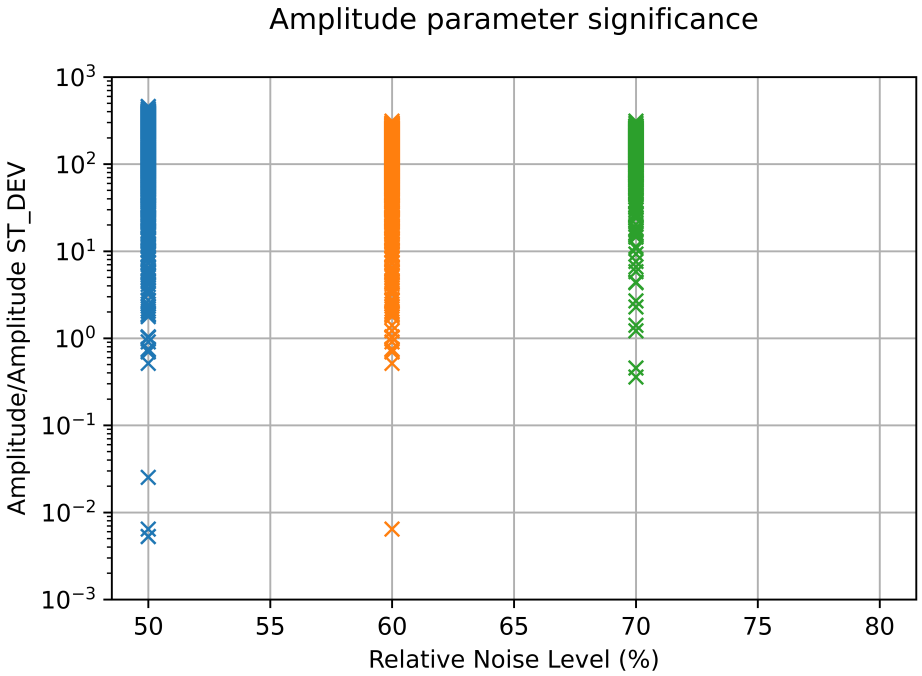

Figure 7.22: *From Koester catalogue the distribution of the amplitude significance* $\frac{A}{\sigma_{amplitude}}$*, where* $\sigma_{amplitude}$ *respect to the noise level (percentage of the signal) with five classes of injected lines at different amplitude (from 1.0 to 0.1) and line's profile width determined by* σ_{line} *1 to 10.*

level of 80%, consequently most of the data above 70% are considered not a good fit. It is interesting that, for the detected lines (again around 13-14 lines only at 60-70%), the average significance from the distribution for the line's width is slightly higher respect to the amplitude. However, we must consider that the total amount of lines included within good fit are now only lines with amplitude 0.75-1.0 and σ_{line} around 3.0 to 5.0.

Total number of lines detected

If we count the number of lines that were able to pass the threshold given by CurveFit respect to the 81 lines correctly injected in the spectrum, the total is decreasing: from Fig. 7.11, where we see the total number of lines detected per spectrum (independently of the line's class), the average is around 30-35, when only overlapping and other fit issues are the major obstacle to the detection. Here the average is around 15 lines, up to 13-14 for 80% noise, which is less than the selection in Table 7.2. So the noise level have cut to 1/4 the total amount of visible lines during observations.

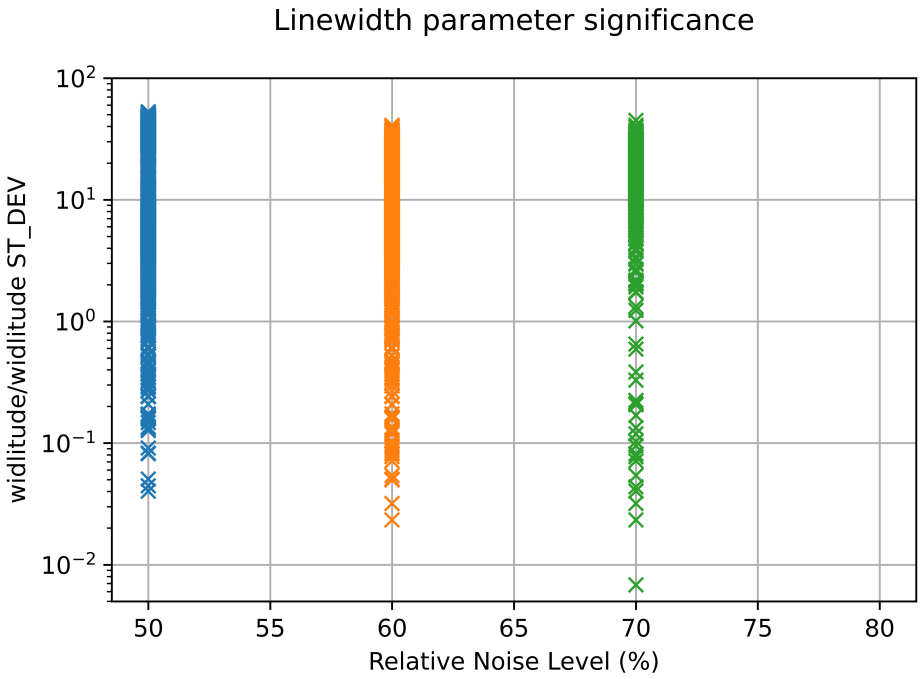

Figure 7.23: *From Koester catalogue the distribution of the width significance* $\frac{A}{\sigma_{width}}$*, where* σ_{width} *respect to the noise level (percentage of the signal) for spectra with five classes of injected lines at different amplitude (from 1.0 to 0.1) and line's profile width determined by* σ_{line} *1 to 10.*

Chapter 8

Conclusions

The aim of this project is to investigate the limitations in the spectral analysis of polluted white dwarfs. Polluted white dwarfs, as mentioned in Chapter 2.3, are faint stars characterised by the presence of detectable metal lines in the stellar atmosphere. There are about a thousand polluted white dwarfs known to-date and the majority were discovered in the Sloan Digital Sky Survey (Sloan (2000)); the pollution process is detailed explained in Chapter 4. To set define an observational strategy, a total of two catalogues were analysed: Koester from 2010 and Levenhagen et al. from 2017 (see Chapter 6.2.1); they differ in total number of data points and temperature of the blackbody emission spectrum.

The spectra produced have a total of 81 lines injected, with a combination of three parameters: 1) the amplitude of the lines (A); 2) the line's width (σ_{line}); 3) the noise level (σ_{noise}). Each spectrum was analysed through a step by step process:

- Blackbody shape fitting and analysis.
- Exposure Time and S/N per pixel calculation, with a focus on the effect of target's magnitude and atmosphere dispersion .
- Lines fit (number of detected lines at different conditions).
- Calculation of parameters estimation over input ratio and significance $\frac{par}{\sigma_{par}}$ (threshold at <1) and the trend respect to the S/N.

In the next paragraph the limits on observation retrieved from the analysis.

8.1 Detection limits

We calculated the thresholds for detection analysing the instrument's limits with respect to amplitude, line's width, mean wavelength position, minimum exposure time (exposure time required for a S/R of 10 must be below 60 minutes for detection), noise level (and regime), magnitude and atmospheric dispersion.

In general, the fitting function parameters (amplitude and line's profile width) are scaling with the noise level as expected. The fit method, from Fig. 7.14 and

7.17, is efficient, and the parameters estimation process reported values comparable with the input parameters for amplitude and line's width. Considering as reference the significance at high noise, for both amplitude and line's width there is a slow decrease of the ratio at noise <40-50%: the plots in Fig. 7.15 and Fig. 7.22 show that the distribution for the amplitude significance has the mean value moved from 10^3 (S/N 1000) to 10^{-1} (S/N 20). Taken as a whole, broad and deep lines (A >0.75, $\sigma_{line} > 3.0$) are easier to detect, while it is already challenging at low noise level (5%) to detect weak lines, as significance drops.

When we consider spectra with a fixed width values (σ_{line}) and the same amplitude for all the lines (with a sample of spectra in which the amplitude has value 0.75 to 0.25), the distribution changed drastically (see Fig. 7.19): already at noise level 0.5% the significance for part of the lines is below 10^{-2}. The amplitude parameter has an important effect on the lines detection, and potentially the spectra injected with only lines at amplitude 0.25 shows a decrease in the parameter significance, as the fit is deteriorated and the error is increasing.
If we assume that the parameter estimated is significant if its error is not comparable, and the significance ratio is more than 1, then the threshold for observation of a line is a noise level of 70%, where we can still detect lines. Such threshold can be converted in amplitude values: at continuum level of 1.0, the line must have amplitude deeper than -0.4/ -0.5 to be observed.

Considering now the line's width parameter,we obtained similar results, as the significance decreases with higher noise, and in general the values for significance are high (see Fig. 7.18). In addition, the distribution in case of fixed values of amplitude and constant width for all the lines shows that the significance remains high for broad and narrow lines, and the threshold for a significance above 1 is around 70-80% noise. There is a weak correlation between the line profile's width and the lines detection, which it is only slightly affected by this parameter.

Regarding the noise level, in particular in the additive regime, there is a decreasing trend for detected lines with the fitting model (see Chapter 7.4.2). Considering that on average, with little or no noise, 35 lines on 73 were detected (due to line blending and lines forest effects), The threshold for half this value (17 lines, which is also the standard selection in Table 7.2) is around 70% noise.

The Exposure Time Calculator was used to estimate a limit for the exposure time on noise-rich spectra. In the standard conditions described in Chapter 7.2 at 3100 $\dot{A}$ and 5% noise level (which is already in the lower part of the wavelength range and affected by atmospheric extinction for UV) the minimum exposure time for S/N =10 is less than 60 s. Using spectra with added noise, we derived that the S/N at 60 minutes was reduced to 78. Considering only the multiplicative regime, with unrealistic noise treatment (free parameter), the noise level did not affect sig-

nificantly the exposure time required for a S/N > 10: overall, the signal is always above the threshold.

Also the magnitude contribution was estimated through the calculator for different cases: as it is described in Chapter 7.2, the standard magnitude used was set at V-magnitude equal to 12. However, setting the V-magnitude of the target at 16 reduced the S/R from 180 to 23 after 60 minutes of observation. The limit to obtain a S/R around 10 in less than 60 minutes is a V-magnitude of 17.

The atmosphere dispersion was treated as the magnitude above. The model described in 7.2.1 is not complex, and it considers only the airmass. The limit derived from the calculator on this variable was on airmass X=2: at x=3 the range of observation was already limited up to 3100 A, due to the UV scattering. It is clear from Fig. 7.7 that for airmass higher than X=2 is nearly impossible to detect anything below 3100 $\dot{A}$.

8.2 Selection of possible targets

The amount of available polluted white dwarfs with spectroscopic data is low, as mentioned in Gänsicke et al. (2012). In the selection considered (see Table 6.1), we analysed the best targets for CUBES, considering the observational limits obtained in the previous sections (magnitude, S/N, exposure time). To calculate the S/N we used the ETC from Chapter 6.3.2, data were taken from Bergeron (2023).

OBJECT	V-Magnitude	Spectral class	Wavelenght coverage (nm)	SNR	Publication
GD 40	11.3	DB	380-400	148.48	Jura et al. (2012)
GD 61	13.8	DBAZ	380-400	148.48	Jura et al. (2012)
PG 0843+516	11.4	DA	360-400	375.74	Gänsicke et al. (2012)
PG 1015+161	15.6	DA	300-400	93.26	Gänsicke et al. (2012)
PG 1225-079	14.8	DB	330-400	93.26	Xu et al. (2013)
GD 362	16.23	DB	300-400	64.25	Xu et al. (2013)
NLTT 43806	15.4	DA	360-400	93.26	Zuckerman et al. (2011)
WD 1929+012	14.2	DA	Not available	148.48	Gänsicke et al. (2012)
G29-38	13	DA	330-400	236.57	Xu et al. (2013)

Above, a selection of possible targets and the S/N at 3100 $\dot{A}$, which is in the wavelength range CUBES would be a pioneer in. The white dwarfs were taken from Table 6.1. It is clear that the lack of high-resolution spectra in the range 300-400 nm brings a huge challenge to test possible targets before CUBES is ready to operate. The targets have a magnitude below 17 as required, and the S/N is always above a limit of 10 (set as minimum required at 60 minutes observation). However, only for PG 1225-079, G29-38, PG 1015+161 and GD 362 the wavelength covers below 350 nm and allows the signal study in the blue part of the spectrum . We decided to test also the other white dwarfs using PG 1015+161 as model at different magnitudes (it has the highest resolution in the wavelength range so far), and retrieved the S/N as an example for all the targets.

It is noteworthy that stars with a magnitude below 14 are probably the best object to observe: scaling the S/N for white dwarfs with a ratio < 100 already at 310 nm, it is possible to notice that the S/R would be probably around 10 and at our limit value. It must be also remembered that the atmospheric dispersion also affects heavily the stars in the range 300-350 nm, with nearly complete extinction of the signal at 300-310 nm (see Chapter 7.2.1). The ETC already considers the atmosphere extinction, so the S/N in the table above includes it.

Overall, CUBES' requirements explained in Chapter 5, in particular the threshold of S/N 20 at 17.5 mag for 313 nm, are reached. The lines with a converged fit in Chapter 7.3 have an amplitude of 0.75 to 1.0 respect to the flux continuum (normalised at 1.0), while narrow lines (0.25 or 0.1 amplitude) are only detected by the CurveFit function, but with high errors on the parameters (two times more than the parameters), and not considered observed. This means that only strong lines could be fit with a significant parameter estimation. Nevertheless, there is a positive result: the instrument in most cases detected the line's presence at a certain wavelength, even if without line's characteristics. Working in parallel with archives of metals lines, it could be possible to retrieve them and have a complete line's description.

8.3 Future improvements

The project developed a total of nearly 20'000 samples of synthetic polluted white dwarfs spectra, differentiated in 27 classes depending on amplitude, lines' width and number of lines injected, and a total of 8 noise classes up to 80% noise. However, there are still steps to have a more realistic simulation.

White dwarfs pollution mechanism

In this work we assumed pollution on the stars due to planetesimals accretion (Jura & Young (2014)). But also other processes are quoted in literature:

Interstellar accretion Especially for hydrogen, interstellar accretion would be possible for the star. In the study from Zuckerman et al. (2007), the possibility was researched and it was concluded that in the absence of cold accretion flows in the circumstellar disk this option would not be possible. Also, settling time for hydrogen is long compared to other heavy elements: if hydrogen and metals accretion happened through the same process, heavier elements would have been already not observable on the surface. Silicates and calcium abundances and emission lines also must be checked, and compared with interstellar medium values.

Two white dwarfs' merger

The case of a merger between two white dwarfs have been also proposed by Zuckerman et al. (2007): it is necessary to verify the final elements abundances ratios of C/Ca and Fe/Mg and compare them with stellar nucleosynthesis simulations. For accretion with a circumstellar disk, the ratios are well above the value of 10, while usually a merger would imply ratios below 5.

Comet accretion

Another possibility is the capture within the tidal radius and consequent distruction of a comet. The comet capture is very unlikely to happen, since the statistics is of one hit every 10'000 years: if we consider also the sinking time for elements, it would be improbable to detect cometary elements lines on white dwarfs surface. An important check to distinguish planetesimal disruption from comet disruption is the amount of oxygen: as in the case of GD362 in Zuckerman et al. (2007), since on average 50% of the material from a comet is ice, we expect to find a high abundance of oxygen from icy molecules.

Asteroid capture

Apart from planetesimals, within planetary systems it is easy to find asteroids of various size and composition. The main components for asteroids are the chondrites (stony meteorite that has not been modified, by either melting or differentiation of the parent body): it is possible to compare the abundance of these rocks with the known asteroids/meteorites, and, in case of planet-like object accretion, the abundance will be lower.

Testing the synthetic spectra

We introduce also different aspects not covered in the analysis due to the limited time for the research project:

Realistic noise treatment

In Chapter 6.2.4, we analyzed the standard noise sources for ground telescopes. Using the technical design characteristics from Chapter 5 regarding the CCDs and workflow of the instrument, it would be possible to retrieve the dark current and apply the spectrograph's efficiency (which is potentially the most significant characteristic of CUBES, as it would reach 40% below 350 nm). Thermal noise and readout noise could be implemented.

Spectrum's template implementation

Instead of single line fitting, with the function from Specutils package (specutils (2023b)) template match it is possible to consider multiple spectrum models with fixed lines (templates) and compare it with the data. The function returns the best template that matches the observed spectrum via chi-square minimization, and the process is :

- Move each template to the first term in the redshift grid.
- Run steps 1 and 2 of the case with known redshift.
- Move to the next term in the redshift grid.
- Run steps 1 and 2 of the case with known redshift.
- Repeat the steps until the end of the grid is reached.
- Return the best redshift, the lowest chi-square and its corresponding template spectrum, and a list with all chi-square values, one per template.

The returned template spectrum corresponding to the lowest chi-square is redshifted and normalized to the observed spectrum (and the index of the template spectrum if the list of templates is iterable). This process would avoid fitting the single lines, and selecting a model prepared before detection (more realistic).

Accretion process modelling

In Chapter 4 we described in details the pollution process for white dwarfs in case of planetesimals accretion. It would be challenging but innovative to introduce a model of accretion for evolved stars. In this case, it would be interesting to obtain the elements' abundances, to better compare the results with Earth's composition, or with previous literature. A plot as Fig. 6.1 would be a good example.

Real target test

Considering the selection in the above paragraph, it would be interesting to start testing CUBES for stars with spectroscopical data in the range 300-400 nm, in particular 300-350 nm. However, the number of targets with the requirements set in the detection limits are still few. An important step is to navigate through white dwarfs' catalogues from space telescopes' surveys (as ESA (2023)) and plannte observations to increase the number of known polluted white dwarfs.

Chapter 9

Appendix

9.1 Additional plots and tables from 7

9.1.1 Targets study in the ETC

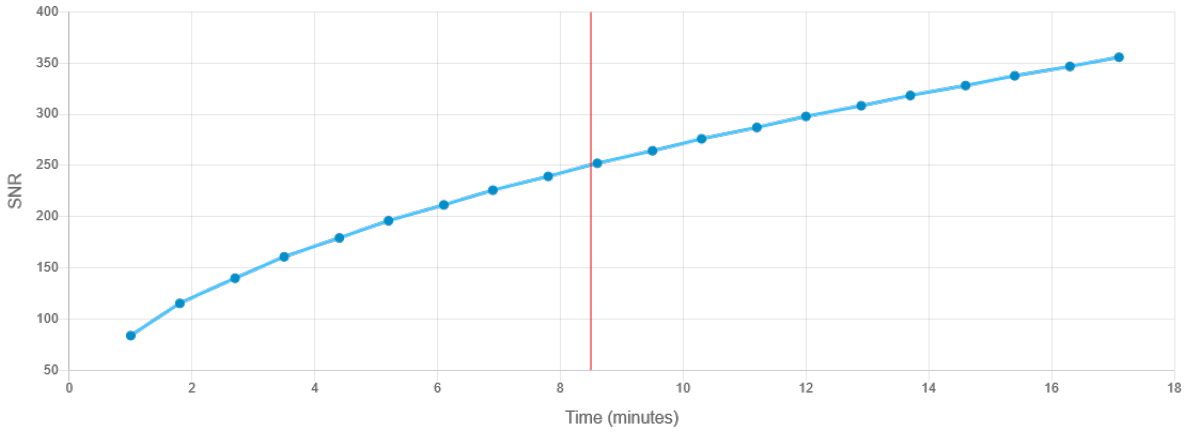

Figure 9.1: *ETC S/R trend respect to exposure time for λ= 3500 Å for white dwarf PG105+161.*

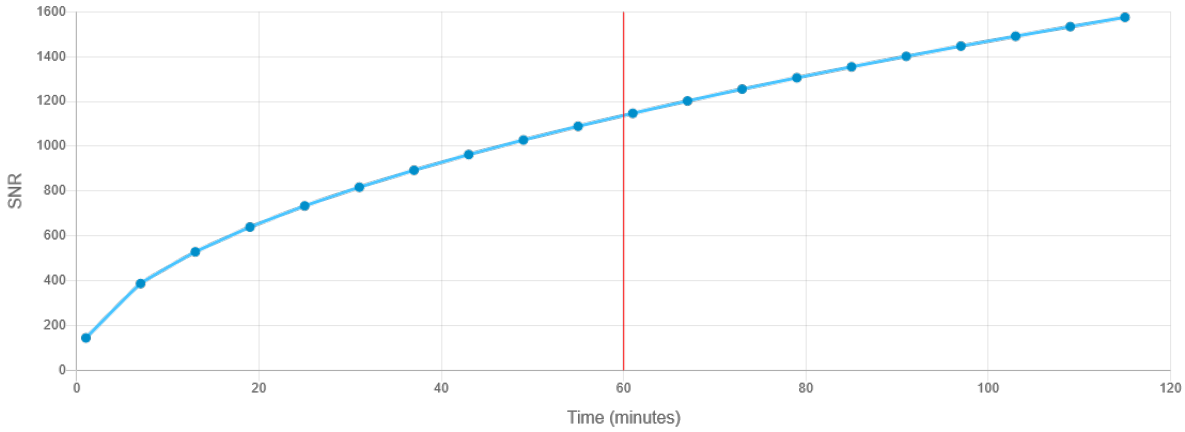

Figure 9.2: *ETC S/R trend respect to exposure time for λ= 3500 Å for white WD0435+410/ GD 61.*

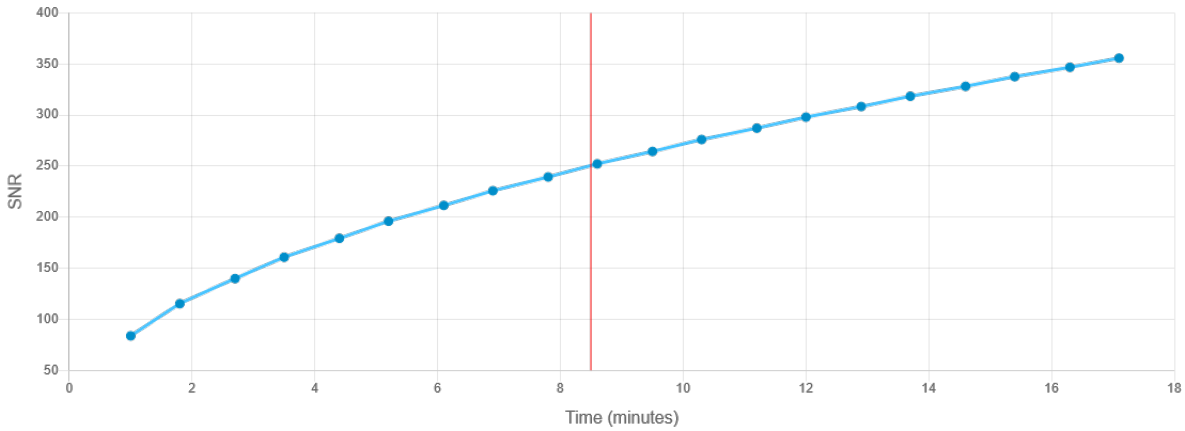

Figure 9.3: *ETC S/R trend respect to exposure time for λ= 3500 Å for white dwarf PG 0843+516.*

9.1.2 Atmosphere dispersion

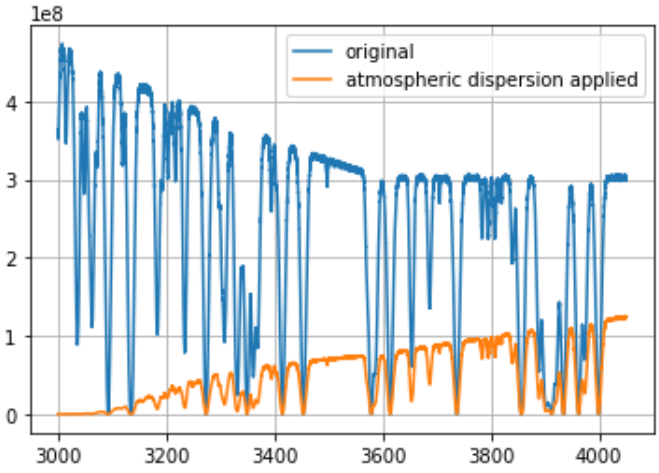

Figure 9.4: *Atmosphere dispersed spectrum from Levenhagen 2017 (airmass equal to 3.0).*

9.1.3 Fit parameters

Results from Levenhagen 2017

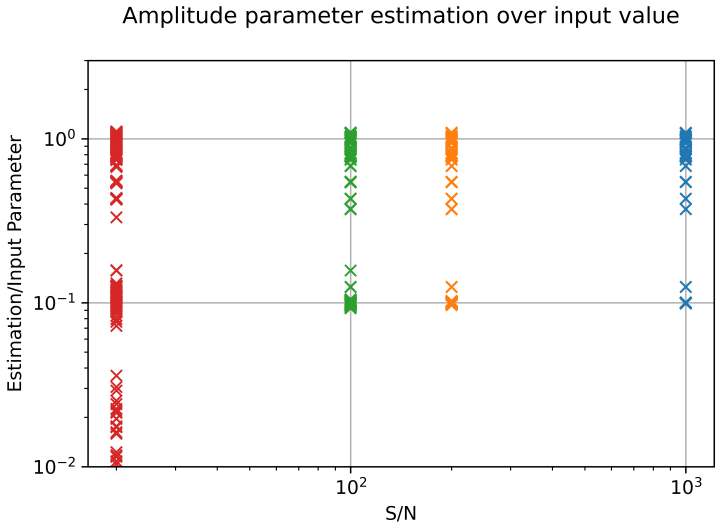

Figure 9.5: *From Levenhagen catalogue the distribution of* $\frac{A_{estimation}}{A_{input}}$ *(amplitude), with five classes of injected lines at different amplitude (from 1.0 to 0.1) and line's profile width determined by* σ_{line} *1.0 to 10.0.*

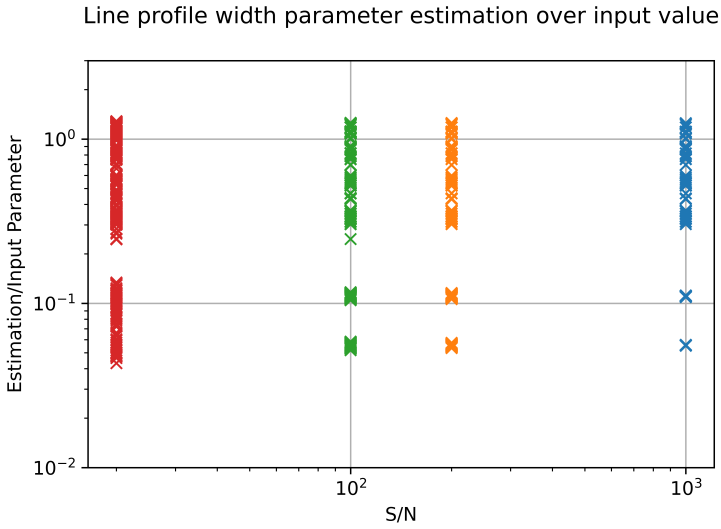

Figure 9.6: *From Levenhagen catalogue the distribution of* $\frac{\sigma_{estimation}}{\sigma_{input}}$ *(line's width), with five classes of injected lines at different amplitude (from 1.0 to 0.1) and line's profile width determined by* σ_{line} *1.0 to 10.0.*

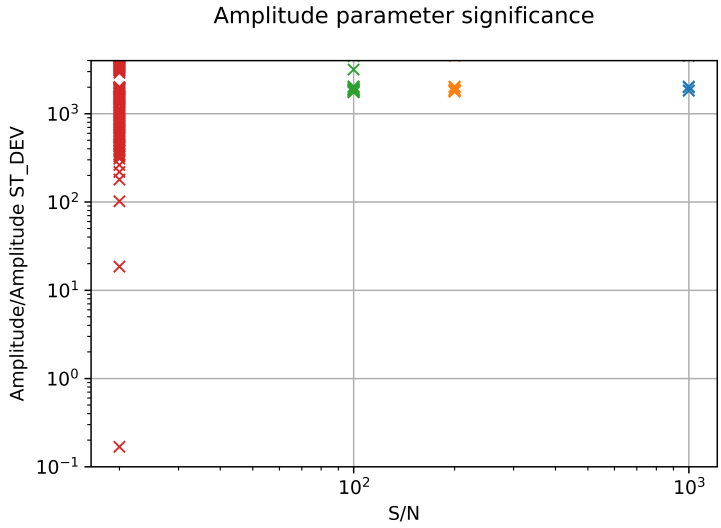

Figure 9.7: *From Levenhagen catalogue the distribution of the amplitude significance* $\frac{A}{\sigma_A}$*, where* σ_{width} *respect to the S/N for spectra with five classes of injected lines at different amplitude (from 1.0 to 0.1) and line's profile width determined by* σ_{line} *1 to 10.*

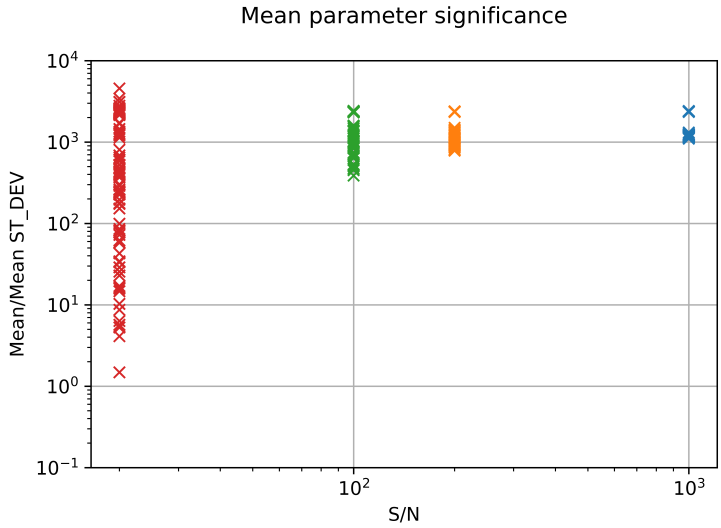

Figure 9.8: *From Levenhagen catalogue the distribution of the amplitude significance* $\frac{\sigma_{line}}{\sigma_{\sigma_{line}}}$*, where* σ_{width} *respect to the S/N for spectra with five classes of injected lines at different amplitude (from 1.0 to 0.1) and line's profile width determined by* σ_{line} *1 to 10.*

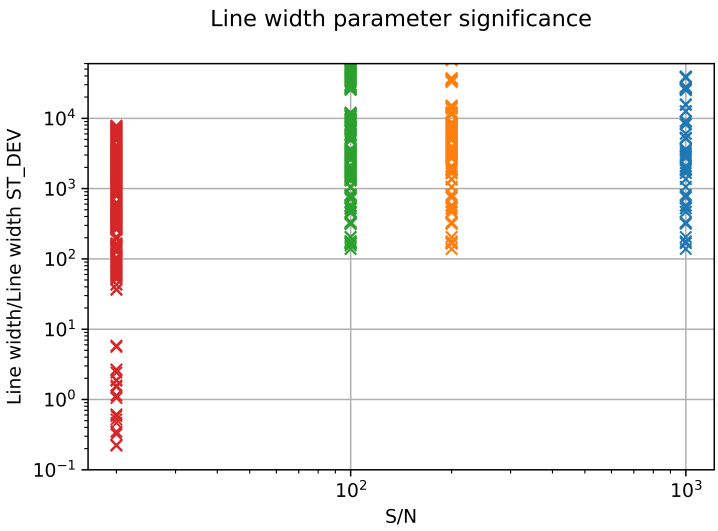

Figure 9.9: *From Levenhagen catalogue the distribution of the amplitude significance* $\frac{\lambda}{\sigma_\lambda}$*, where* σ_{width} *respect to the S/N for spectra with five classes of injected lines at different amplitude (from 1.0 to 0.1) and line's profile width determined by* σ_{line} *1 to 10.*

Bibliography

Agnor C., Asphaug E., 2004, *Accretion efficiency during planetary collisions*, The Astrophysical Journal, 613, L157

Alcalá J., Cupani G., Evans C., Franchini M., Nisini B., 2023, *Accretion and outflows in young stars with CUBES*, Experimental Astronomy, 55, 165

Ali S. S., De Propris R., 2023, *Unveiling UV-bright stellar populations in red and dead galaxies with CUBES*, Experimental Astronomy, 55, 199

Aumann H., et al., 1984, *Discovery of a shell around Alpha Lyrae*, Astrophysical Journal, Part 2-Letters to the Editor (ISSN 0004-637X), vol. 278, March 1, 1984, p. L23-L27., 278, L23

Balashev S., Noterdaeme P., 2023, *Molecular hydrogen in absorption at high redshifts: Science cases for CUBES*, Experimental Astronomy, 55, 223

Beichman C. A., Greene T. P., 2017, Technical report, *Observing Exoplanets with the James Webb Space Telescope*. Springer International Publishing AG

Bergeron 2023, *MWDD*, https://www.montrealwhitedwarfdatabase.org/tables-and-charts.html

Bik A., et al., 2012, *Age Spread in W3 Main*, ApJ, 744, 87

Blum J., et al., 2000, *Growth and form of planetary seedlings: Results from a microgravity aggregation experiment*, Physical Review Letters, 85, 2426

Blum J., Wurm G., Poppe T., Kempf S., Kozasa T., 2002, *First results from the cosmic dust aggregation experiment CODAG*, Advances in Space Research, 29, 497

Bonsor A., Xu S., 2017, *White Dwarf Planetary Systems: insights regarding the fate of planetary systems*, Formation, Evolution, and Dynamics of Young Solar Systems, pp 229–252

Borucki W. J., et al., 2012, *Kepler-22b: a 2.4 Earth-radius planet in the habitable zone of a Sun-like star*, The Astrophysical Journal, 745, 120

Bowman D. M., 2017, *Amplitude modulation of pulsation modes in delta Scuti stars*. Springer

Brucato J. R., Nuth III J. A., 2010, *Laboratory studies of simple dust analogs in astrophysical environments*, Protoplanetary Dust: Astrophysical and Cosmochemical Perspectives, edited by D. Apai and DS Lauretta, Cambridge University Press, Cambridge, UK, pp 128–160

Butler R. P., Vogt S. S., Marcy G. W., Fischer D. A., Wright J. T., Henry G. W., Laughlin G., Lissauer J. J., 2004, *A Neptune-mass planet orbiting the nearby M dwarf GJ 436*, The Astrophysical Journal, 617, 580

Butler R. P., et al., 2017, *The LCES HIRES/Keck precision radial velocity exoplanet survey*, The Astronomical Journal, 153, 208

Cameron A., 1973, *Formation of the outer planets*, Space Science Reviews, 14, 383

Cameron A. C., Pollacco D., Hellier C., West R., 2008, *The WASP transit surveys*, Proceedings of the International Astronomical Union, 4, 29–35

Carroll B. W., Ostlie D. A., 2017, *An introduction to modern astrophysics*. Cambridge University Press

Catanzarite J., Shao M., Tanner A., Unwin S., Yu J., 2006, *Astrometric detection of terrestrial planets in the habitable zones of nearby stars with SIM PlanetQuest*, Publications of the Astronomical Society of the Pacific, 118, 1319

Chayer P., Fontaine G., Wesemael F., 1995, *Radiative levitation in hot white dwarfs: Equilibrium theory*, The Astrophysical Journal Supplement Series, 99, 189

Cristiani S., et al., 2022, *CUBES, the Cassegrain U-Band Efficient Spectrograph for the VLT*, The Messenger, 188, 36

Cumming A., Butler R. P., Marcy G. W., Vogt S. S., Wright J. T., Fischer D. A., 2008, *The Keck planet search: detectability and the minimum mass and orbital period distribution of extrasolar planets*, Publications of the Astronomical Society of the Pacific, 120, 531

Curé M., Araya I., 2023, *Radiation-Driven Wind Hydrodynamics of Massive Stars: A Review*, Galaxies, 11, 68

Dawson R. I., Johnson J. A., 2018, *Origins of hot Jupiters*, Annual Review of Astronomy and Astrophysics, 56, 175

De Wit J., et al., 2018, *Atmospheric reconnaissance of the habitable-zone Earth-sized planets orbiting TRAPPIST-1*, Nature Astronomy, 2, 214

Debes J. H., Sigurdsson S., Woodgate B. E., 2005, *Cool customers in the stellar graveyard. I. Limits to extrasolar planets around the white dwarf G29-38*, The Astrophysical Journal, 633, 1168

Deutsch A. J., 1956, *The Circumstellar Envelope of Alpha Herculis.*, The Astrophysical Journal, 123, 210

Dominik C., Blum J., Cuzzi J., Wurm G., 2006, *Growth of dust as the initial step toward planet formation*, arXiv preprint astro-ph/0602617

Doppmann 1994-2008, *KECK-HIRES*, https://www2.keck.hawaii.edu/inst/hires/

Doyle L. R., 2019, *The discovery of "Tatooine": Kepler-16b*, New Astronomy Reviews, 84, 101515

Dufour P., Kilic M., Fontaine G., Bergeron P., Melis C., Bochanski J., 2012, *Detailed compositional analysis of the heavily polluted DBZ white dwarf SDSS J073842.56+ 183509.06: a window on planet formation?*, The Astrophysical Journal, 749, 6

D'Odorico V., 2023, *Portraying the missing baryonic mass at the cosmic noon: the contribution of CUBES*, Experimental Astronomy, 55, 209

ESA 2023, *GAIA*, https://www.esa.int/Science_Exploration/Space_Science/Gaia

ESA 2026, *PLATO*, https://platomission.com/

ESA 1989-1993, *HIPPARCOS*, https://www.cosmos.esa.int/web/hipparcos

ESO 2007, *Hertzsprung–Russell diagram*, https://www.eso.org/public/italy/images/eso0728c/?lang

ESO 2023a, *UVES*, https://www.eso.org/public/teles-instr/paranal-observatory/vlt/vlt-instr/uves/

ESO 2023b, *x-shooter*, https://www.eso.org/sci/facilities/paranal/instruments/xshooter.html

Ernandes H., Barbuy B., Castilho B., Evans C., Cescutti G., 2023, *Simulated observations of heavy elements with CUBES*, Experimental Astronomy, 55, 149

Evans C., et al., 2023, *The CUBES science case*, Experimental Astronomy, 55, 1

Gaia C., et al., 2018, *Gaia data release 2 summary of the contents and survey properties*, Astronomy & Astrophysics, 616

Gänsicke B., Koester D., Marsh T., Rebassa-Mansergas A., Southworth J., 2008, *SDSS J084539.17+ 225728.0: the first DBZ white dwarf with a metal-rich gaseous debris disc*, Monthly Notices of the Royal Astronomical Society: Letters, 391, L103

Gänsicke B., Koester D., Farihi J., Girven J., Parsons S., Breedt E., 2012, *The chemical diversity of exo-terrestrial planetary debris around white dwarfs*, Monthly Notices of the Royal Astronomical Society, 424, 333

Gehrz R., Woolf N., 1971, *Mass loss from M stars*, Astrophysical Journal, vol. 165, p. 285, 165, 285

Genoni M., et al., 2023, *The CUBES instrument model and simulation tools: Their role in the project Phase A study*, Experimental Astronomy, 55, 301

Gentile Fusillo N. P., et al., 2019, *A Gaia Data Release 2 catalogue of white dwarfs and a comparison with SDSS*, Monthly Notices of the Royal Astronomical Society, 482, 4570

Gentile Fusillo N., et al., 2021, *A catalogue of white dwarfs in Gaia EDR3*, Monthly Notices of the Royal Astronomical Society, 508, 3877

Gilman R. C., 1969, *On the composition of circumstellar grains*, Astrophysical Journal, vol. 155, p. L185, 155, L185

Giribaldi R. E., Smiljanic R., 2023, *Beryllium abundances in turn-off stars of globular clusters with the CUBES spectrograph*, Experimental Astronomy, 55, 117

Girven J., Brinkworth C., Farihi J., Gänsicke B., Hoard D., Marsh T., Koester D., 2012, *Constraints on the lifetimes of disks resulting from tidally destroyed rocky planetary bodies*, The Astrophysical Journal, 749, 154

Goldreich P., Tremaine S., 1979, *The excitation of density waves at the Lindblad and corotation resonances by an external potential*, Astrophysical Journal, 233, 857

Goldreich P., Tremaine S., 1982, *The dynamics of planetary rings*, Annual review of astronomy and astrophysics, 20, 249

Goldreich P., Ward W. R., 1973, *The formation of planetesimals*, Astrophysical Journal, Vol. 183, pp. 1051-1062 (1973), 183, 1051

Goldschmidt V. M., Holmsen D., 1927, *Geochemische verteilungsgesetze der elemente*. No. 1, In Kommission bei J. Dybwad

Graue R., Kampf D., Roeser S., Bastian U., Seifert W., 2003, in Future EUV/UV and Visible Space Astrophysics Missions and Instrumentation. pp 9–20

Grimm S. L., et al., 2018, *The nature of the TRAPPIST-1 exoplanets*, Astronomy & Astrophysics, 613, A68

Hainaut 2005, *Signal and noise from ESO*, https://www.eso.org/~ohainaut/ccd/sn.html

Harrison J. H., Bonsor A., Madhusudhan N., 2018, *Polluted white dwarfs: constraints on the origin and geology of exoplanetary material*, Monthly Notices of the Royal Astronomical Society, 479, 3814

Hebrard G., 2006, *A posteriori detection of the planetary transit of HD 189733 b in the Hipparcos photometry*, Astronomy & Astrophysics, 445, 341

Hellier 2023, *WASP*, https://wasp-planets.net/wasp-planets//

Henry G. W., Marcy G. W., Butler R. P., Vogt S. S., 1999, *A transiting "51 Peg-like" planet*, The Astrophysical Journal, 529, L41

Hessman F. V., et al., 2011, in AIP Conference Proceedings. pp 281–286

Höfner S., Olofsson H., 2018, *Mass loss of stars on the asymptotic giant branch: Mechanisms, models and measurements*, The Astronomy and Astrophysics Review, 26, 1

Høg E., et al., 1997, *The Tycho Catalogue*, Astronomy and Astrophysics, Vol. 323, p. L57-L60, 323, L57

Hollands M., Koester D., Alekseev V., Herbert E., Gänsicke B. T., 2017, *Cool DZ white dwarfs–I. Identification and spectral analysis*, Monthly Notices of the Royal Astronomical Society, 467, 4970

Hubeny I., Lanz T., 2017, *A brief introductory guide to TLUSTY and SYNSPEC*, arXiv preprint arXiv:1706.01859

INAF 2023, *CUBES*, https://cubes.inaf.it/

Johnson H. L., Morgan W., 1953, *Fundamental stellar photometry for standards of spectral type on the revised system of the Yerkes spectral atlas*, Astrophysical Journal, Vol. 117, p. 313, 117, 313

Johnston K., et al., 2000, in American Astronomical Society Meeting Abstracts. pp 14–03

Jura M., Kleinmann S., 1992, *Oxygen-rich semiregular and irregular variables*, Astrophysical Journal Supplement Series (ISSN 0067-0049), vol. 83, no. 2, p. 329-349., 83, 329

Jura M., Young E., 2014, *Extrasolar cosmochemistry*, Annual Review of Earth and Planetary Sciences, 42, 45

Jura M., Xu S., Klein B., Koester D., Zuckerman B., 2012, *Two extrasolar asteroids with low volatile-element mass fractions*, The Astrophysical Journal, 750, 69

Kaltenegger L., Pepper J., Stassun K., Oelkers R., 2019, *TESS Habitable Zone Star Catalog*, The Astrophysical Journal Letters, 874, L8

Kanaan A., et al., 2005, *Whole Earth Telescope observations of BPM 37093: A seismological test of crystallization theory in white dwarfs*, Astronomy & Astrophysics, 432, 219

Karovicova I., Wittkowski M., Ohnaka K., Boboltz D., Fossat E., Scholz M., 2013, *New insights into the dust formation of oxygen-rich AGB stars*, Astronomy & Astrophysics, 560, A75

Katz D., et al., 2004, *Spectroscopic survey of the Galaxy with Gaia–I. Design and performance of the Radial Velocity Spectrometer*, Monthly Notices of the Royal Astronomical Society, 354, 1223

Kepler S. O., et al., 2005, *Measuring the evolution of the most stable optical clock G 117-B15A*, The Astrophysical Journal, 634, 1311

Kim S.-L., et al., 2016, *KMTNET: a network of 1.6 m wide-field optical telescopes installed at three southern observatories*, Journal of The Korean Astronomical Society, vol. 49, issue 1, pp. 37-44, 49, 37

Klahr H., Bodenheimer P., 2006, *Formation of giant planets by concurrent accretion of solids and gas inside an anticyclonic vortex*, The Astrophysical Journal, 639, 432

Klein B., Jura M., Koester D., Zuckerman B., Melis C., 2010, *Chemical abundances in the externally polluted white dwarf GD 40: evidence of a rocky extrasolar minor planet*, The Astrophysical Journal, 709, 950

Klein B., Jura M., Koester D., Zuckerman B., 2011, *Rocky extrasolar planetary compositions derived from externally polluted white dwarfs*, The Astrophysical Journal, 741, 64

Klein B. L., Doyle A. E., Zuckerman B., Dufour P., Blouin S., Melis C., Weinberger A. J., Young E. D., 2021, *Discovery of beryllium in white dwarfs polluted by planetesimal accretion*, The Astrophysical Journal, 914, 61

Koester D., 2009, *Accretion and diffusion in white dwarfs-New diffusion timescales and applications to GD 362 and G 29-38*, Astronomy & Astrophysics, 498, 517

Koester D., 2010, *White dwarf spectra and atmosphere models*, Memorie della Societa Astronomica Italiana, 81, 921

Konacki M., Wolszczan A., 2003, *Masses and orbital inclinations of planets in the PSR B1257+ 12 system*, The Astrophysical Journal, 591, L147

Kuiper G. P., 1941, *List of known white dwarfs*, Publications of the Astronomical Society of the Pacific, 53, 248

Kurtz S., 2005, *Hypercompact HII regions*, IAU Symp., 1, 111

Kusaka T., Nakano T., Hayashi C., 1970, *Growth of solid particles in the primordial solar nebula*, Progress of Theoretical Physics, 44, 1580

Lamers H. J., Levesque E. M., 2017, *Understanding Stellar Evolution*. IoP Publishing Bristol

Lee J. W., Kim S.-L., Kim C.-H., Koch R. H., Lee C.-U., Kim H.-I., Park J.-H., 2009, *The sdB+ M eclipsing system HW Virginis and its circumbinary planets*, The Astronomical Journal, 137, 3181

Levenhagen R. S., Diaz M. P., Coelho P. R., Hubeny I., 2017, *A grid of synthetic spectra for hot DA white dwarfs and its application in stellar population synthesis*, The Astrophysical Journal Supplement Series, 231, 1

Lissauer J. J., 1993, *Planet formation*, Annual review of astronomy and astrophysics, 31, 129

Lodders K., 2003, *Solar system abundances and condensation temperatures of the elements*, The Astrophysical Journal, 591, 1220

Lodders K., 2010, in Principles and Perspectives in Cosmochemistry: Lecture Notes of the Kodai School on'Synthesis of Elements in Stars' held at Kodaikanal Observatory, India, April 29-May 13, 2008. pp 379–417

Loidl R., Höfner S., Jørgensen U., Aringer B., 1999, *Dynamic model atmospheres of AGB stars. II. Synthetic near infrared spectra of carbon stars*, Astronomy and Astrophysics, v. 342, p. 531-541 (1999), 342, 531

Mandell A. M., Sigurdsson S., 2003, *Survival of terrestrial planets in the presence of giant planet migration*, The Astrophysical Journal, 599, L111

Mayor M., Queloz D., 1995, *A Jupiter-mass companion to a solar-type star*, nature, 378, 355

McCullough P., Stys J., Valenti J., Fleming S., Janes K., Heasley J., 2005, *The XO project: searching for transiting extrasolar planet candidates*, Publications of the Astronomical Society of the Pacific, 117, 783

McDonald I., Zijlstra A., 2016, *Pulsation-triggered mass loss from AGB stars: the 60 day critical period*, The Astrophysical Journal Letters, 823, L38

McDonough W. F., 2001, *The composition of the Earth*, Earthquake thermodynamics and phase transformations in the Earth's interior, 76, 3

Mullally F., Reach W. T., Degennaro S., Burrows A., 2009, *Spitzer planet limits around the pulsating white dwarf GD66*, The Astrophysical Journal, 694, 327

NASA 1990, *Hubble Space Telescope*, https://hubblesite.org/science/exoplanets

NASA 2005, *EPOXI*, https://science.nasa.gov/mission/deep-impact-epoxi/

NASA 2022, *Light Curve of a Planet Transiting Its Star*, https://exoplanets.nasa.gov/resources/280/light-curve-of-a-planet-transiting-its-star/

NASA 2023, *NASA Exoplanets' catalogue*, https://exoplanets.nasa.gov/

NASA/ESA 2009, *Kepler*, https://science.nasa.gov/mission/kepler/in-depth/s

NASA/ESA 2022, *JWST*, https://webb.nasa.gov/s

NIST 2013, *NIST Catalogue*, https://www.nist.gov/pml/handbook-basic-atomic-spectroscopic-data

Neugebauer G., Leighton R. B., 1969, *Two-micron sky survey: A preliminary catalog*. Vol. 3047, Scientific and Technical Information Division, National Aeronautics and ...

Nittler L. R., Ciesla F., 2016, *Astrophysics with extraterrestrial materials*, Annual Review of Astronomy and Astrophysics, 54, 53

Nittler L. R., McCoy T. J., Clark P. E., Murphy M. E., Trombka J. I., Jarosewich E., 2004, *Bulk element compositions of meteorites: A guide for interpreting remote-sensing geochemical measurements of planets and asteroids*, Antarctic Meteorite Research

Ohnaka K., Weigelt G., Hofmann K.-H., 2017, *Clumpy dust clouds and extended atmosphere of the AGB star W Hydrae revealed with VLT/SPHERE-ZIMPOL and VLTI/AMBER-II. Time variations between pre-maximum and minimum light*, Astronomy & Astrophysics, 597, A20

Opitom C., et al., 2023, *Cometary science with CUBES*, Experimental Astronomy, 55, 59

OriginLab 2023, *Gaussian Function*, https://www.originlab.com/doc/origin-help/gauss-fitfunc

Paczynski 2008, *MOA*, http://www2.phys.canterbury.ac.nz/moa//

Patat F., et al., 2011, *Optical atmospheric extinction over Cerro Paranal*, Astronomy & Astrophysics, 527, A91

Perryman M., 2018, *The exoplanet handbook*. Cambridge university press

Perryman M. A., et al., 1997, *The HIPPARCOS catalogue*, Astronomy and Astrophysics, Vol. 323, p. L49-L52, 323, L49

Perryman M., et al., 2001, *GAIA: Composition, formation and evolution of the Galaxy*, Astronomy & Astrophysics, 369, 339

Petrescu R. V., Aversa R., Apicella A., Petrescu F. I., 2018, *NASA Data used to discover eighth planet circling distant star*, Journal of Aircraft and Spacecraft Technology, 2, 19

Price S. D., Walker R. G., 1976, *The AFGL Four Color Infrared Sky Survey: Catalog of Observations at 4.2, 11.0, 19.8, and 27.4 Micrometers*. Vol. 76, Air Force Geophysics Laboratories, Air Force Systems Command, United States ...

PrincetonUniversity 2003, *HATNET*, https://hatnet.org/

Qian S.-B., Liao W.-P., Zhu L.-Y., Dai Z.-B., 2009, *Detection of a giant extrasolar planet orbiting the eclipsing polar DP Leo*, The Astrophysical Journal Letters, 708, L66

Queloz D., 2020, *Nobel Lecture: 51 Pegasi b and the exoplanet revolution*, Reviews of Modern Physics, 92, 030503

Rasio F., Nicholson P., Shapiro S., Teukolsky S., 1992, *An observational test for the existence of a planetary system orbiting PSR1257+ 12*, Nature, 355, 325

Reader J., 2000, in AIP Conference Proceedings. pp 104–117

Reimers D., 1975, Technical report, *Circumstellar absorption lines and mass loss from red giants*. Univ., Kiel

Richmond 2023, *Signal and noise*, http://spiff.rit.edu/classes/ast613/lectures/signal/signal_illus.html

Rivera E. J., Butler R. P., Vogt S. S., Laughlin G., Henry G. W., Meschiari S., 2009, *A super-Earth orbiting the nearby Sun-like star HD 1461*, The Astrophysical Journal, 708, 1492

Robichon N., Arenou F., 2000, *HD 209458 planetary transits from Hipparcos photometry*, Astronomy and Astrophysics-A&A, 355, 295

Robinson 2017, *Exoplanet Studies with the Origins Space Telescope*, https://exoplanets.nasa.gov/exep/newsletters/issue17/ost/

Rosenblatt F., 1971, *A two-color photometric method for detection of extra-solar planetary systems*, Icarus, 14, 71

Safronov V. S., 1972, *Evolution of the Protoplanetary Cloud and Formation of the Earth and the Planets*

Safronov V., Zvjagina E., 1969, *Relative sizes of the largest bodies during the accumulation of planets*, Icarus, 10, 109

Sasselov D. D., 2003, *The new transiting planet OGLE-TR-56b: orbit and atmosphere*, The Astrophysical Journal, 596, 1327

Sigurdsson S., Stairs I., Moody K., Arzoumanian K., Thorsett S., 2008, in Extreme Solar Systems. p. 119

Silvotti R., et al., 2007, *A giant planet orbiting the 'extreme horizontal branch'star V 391 Pegasi*, Nature, 449, 189

Sion E. M., Greenstein J. L., Landstreet J. D., Liebert J., Shipman H. L., Wegner G. A., 1983, *A proposed new white dwarf spectral classification system*, Astrophysical Journal, Part 1 (ISSN 0004-637X), vol. 269, June 1, 1983, p. 253-257. Research supported by the John Simon Guggenheim Memorial Foundation., 269, 253

Sloan 2000, *SDSS*, https://www.sdss.org/

Smith N., 2014, *Mass loss: its effect on the evolution and fate of high-mass stars*, Annual Review of Astronomy and Astrophysics, 52, 487

Solomon P., Jefferts K. B., Penzias A. A., Wilson R. W., 1971, *Observation of CO emission at 2.6 millimeters from IRC+ 10216*, The Astrophysical Journal, 163, L53

Struve O., 1952, *Proposal for a project of high-precision stellar radial velocity work*, The Observatory, 72, 199

Supulver K. D., Bridges F. G., Tiscareno S., Lievore J., Lin D., 1997, *The sticking properties of water frost produced under various ambient conditions*, Icarus, 129, 539

Tej A., Lançon A., Scholz M., Wood P. R., 2003, *Optical and near-IR spectra of O-rich Mira variables: A comparison between models and observations*, Astronomy & Astrophysics, 412, 481

Tielens A., Waters L., Bernatowicz T., 2005, in Chondrites and the Protoplanetary Disk. p. 605

Tonks W., Melosh H., 1992, in Abstracts of the Lunar and Planetary Science Conference, volume 23, page 1437,(1992).

Tremblay P.-E., et al., 2019, *Core crystallization and pile-up in the cooling sequence of evolving white dwarfs*, Nature, 565, 202

Tsapras Y., 2018, *Microlensing searches for exoplanets*, Geosciences, 8, 365

Udalski 1997, *OGLE*, https://ogle.astrouw.edu.pl/

Vallenari A., et al., 2023, *Gaia Data Release 3-Summary of the content and survey properties*, Astronomy & Astrophysics, 674, A1

Van Marle A. J., Smith N., Owocki S. P., Van Veelen B., 2010, *Numerical models of collisions between core-collapse supernovae and circumstellar shells*, Monthly Notices of the Royal Astronomical Society, 407, 2305

Vanderburg A., et al., 2015, *A disintegrating minor planet transiting a white dwarf*, Nature, 526, 546

Veras D., 2016, *Post-main-sequence planetary system evolution*, Royal Society Open Science, 3, 150571

Weidenschilling S. J., Donn B. D., Meakin P., 1989, *The physics of planetesimal formation.*, The Formation and Evolution of Planetary Systems, pp 131–146

Wenger 2000, *Database for astronomical objects*, http://simbad.cds.unistra.fr/simbad/

Wenz J., 2019, *Four Types of Stars That Will Not Exist for Billions or Even Trillions of Years*, https://www.smithsonianmag.com/science-nature/four-types-stars-will-not-exist-billions-or-even-trillions-years-180971299/

Wetherill G. W., 1990, *Comparison of analytical and physical modeling of planetesimal accumulation*, Icarus, 88, 336

Wetherill G., 1996, *The formation and habitability of extra-solar planets*, Icarus, 119, 219

White 2013, *Goldschmidt classification*, https://wiki.aalto.fi/display/SSC/Goldschmidt+classification

Whitelock P., Feast M., Catchpole R., 1991, *IRAS sources and the nature of the Galactic Bulge*, Monthly Notices of the Royal Astronomical Society (ISSN 0035-8711), vol. 248, Jan. 15, 1991, p. 276-312., 248, 276

Wilson W. J., Barrett A. H., 1968, *Discovery of OH Radio Emission from the Infrared Star NML Cygni.*, The Astronomical Journal Supplement, 73, 209

Wolszczan A., 1994, *Confirmation of Earth-mass planets orbiting the millisecond pulsar PSR B1257+ 12*, Science, 264, 538

Wright C. O., Egan M. P., Kraemer K. E., Price S. D., 2003, *The Tycho-2 spectral type catalog*, The Astronomical Journal, 125, 359

Xu S., Bonsor A., 2021, *Exogeology from polluted white dwarfs*, Elements: An International Magazine of Mineralogy, Geochemistry, and Petrology, 17, 241

Xu S., Jura M., Klein B., Koester D., Zuckerman B., 2013, *Two beyond-primitive extrasolar planetesimals*, The Astrophysical Journal, 766, 132

Xu S., Jura M., Koester D., Klein B., Zuckerman B., 2014, *Elemental compositions of two extrasolar rocky planetesimals*, The Astrophysical Journal, 783, 79

Zanutta A., et al., 2022, *CUBES phase a design overview*, Experimental astronomy.

Zboril M., 1996, in MASS, Model Atmospheres and Spectrum Synthesis. p. 193

Zsom A., Ormel C. W., Güttler C., Blum J., Dullemond C., 2010, *The outcome of protoplanetary dust growth: pebbles, boulders, or planetesimals?-II. Introducing the bouncing barrier*, Astronomy & Astrophysics, 513, A57

Zuckerman B., Koester D., Melis C., Hansen B. M., Jura M., 2007, *The chemical composition of an extrasolar minor planet*, The Astrophysical Journal, 671, 872

Zuckerman B., Koester D., Dufour P., Melis C., Klein B., Jura M., 2011, *An aluminum/calcium-rich, iron-poor, white dwarf star: evidence for an extrasolar planetary lithosphere?*, The Astrophysical Journal, 739, 101

numpy 2023, *Numpy*, https://numpy.org

scipy 2023a, *CubicSpline*, https://docs.scipy.org/doc/scipy/reference/interpolate.html

scipy 2023b, *CurveFit*, https://docs.scipy.org/doc/scipy/reference/generated/scipy.optimize.curve_fit.html

specutils 2023a, *JWST exoplanet*, https://www.nasa.gov/universe/exoplanets/webb-discovers-methane-carbon-dioxide-in-atmosphere-of-k2-18-b/

specutils 2023b, *Template*, https://specutils.readthedocs.io/en/stable/api/specutils.analysis.template_match.html